Volume 17, Issue 4, 2010

JOURNAL OF

Enhanced Heat Transfer

Ralph L. Webb
Editor-in-Chief

begell house, inc.
publishers

Journal of Enhanced Heat Transfer (ISSN 1065-5131) is published quarterly and owned by Begell House, Inc., 50 Cross Highway, Redding, Connecticut 06896, telephone (203) 938-1300. US rate for 2010 subscription is $654 call publisher for price information for print/online or online only subscriptions. Add $10.00 per issue for foreign airmail shipping and handling fees to all orders shipped outside the United States or Canada. All subscriptions are payable in advance. Subscriptions are entered on an annual basis, i.e., January-December. For immediate service and charge card sales, call (203) 938-1300 Monday through Friday 9 am–5 pm est. Fax orders to (203)938-1304. Send written orders to SubscriptionsDepartment, Begell House, Inc., 50 Cross Highway, Redding, Connecticut 06896.

Printed January 31, 2011

Journal of
ENHANCED HEAT TRANSFER
Theory and Application in High Performance Heat and Mass Transfer
Published by Begell House, Connecticut

JOURNAL OF ENHANCED HEAT TRANSFER

AIMS AND SCOPE • AUTHOR INSTRUCTIONS

AIMS AND SCOPE

The *Journal of Enhanced Heat Transfer* will consider a wide range of scholarly papers related to the subject of "enhanced heat and mass transfer" in natural and forced convection of liquids and gases, boiling, condensation, radiative heat transfer. Areas of interest include:

- Specially configured surface geometries, electric or magnetic fields, and fluid additives - all aimed at enhancing heat transfer rates. Papers may include theoretical modeling, experimental techniques, experimental data, and/or application of enhanced heat transfer technology.
- The general topic of "high performance" heat transfer concepts or systems is also encouraged.
- The journal will also consider well-prepared review articles within the identified subject areas.
- Archival quality papers previously published at limited distribution conferences are also accepted. The author may need to provide a copyright release from the conference publisher

SUBMISSION OF MANUSCRIPTS

Authors should submit their manuscript electronically in Word or pdf format. Electronically transmitted manuscripts should be e-mailed to the Editor-in-Chief, Ralph.Webb@psu.edu. Authors may also electronically submit manuscripts to any of the regional editors listed on the inside *Journal* cover or on the Begell House website http://www.begellhouse.com/journals/4c8f5faa331b09ea.html. The manuscript must be accompanied by a statement that it has not been published elsewhere and that it has not been submitted simultaneously for publication elsewhere. Authors are responsible for obtaining permission to reproduce copyrighted material from other sources and are required to sign an agreement for the transfer of copyright to the publisher. All accepted manuscripts, artwork, and photographs become the property of the publisher. All parts of the manuscript should be typewritten, with one inch margins on all sides. Single line spacing is acceptable. Manuscript pages must be numbered consecutively throughout the paper. Each article should be summarized in an abstract of no more that 100 words. Avoid abbreviations, diagrams, and reference to the text.

REFERENCE FORMAT

Identify references in the text by giving the last name of the author(s) and the year of publication in square brackets. References will be cited at the end of the paper in alphabetical order. References should include: author name(s), year, title, journal (or book and publisher), volume, issue number and page numbers. Below are examples of entries for a journal, a book, a paper in an edited book, and conference proceedings.

JOURNAL: Nakayama, W. and Nakajima, T. (1982) Effects of Pore Diameters and System Pressure on Saturated Pool Nucleate Boiling Heat Transfer From Porous Surfaces, Journal of Enhanced Heat Transfer, Vol. 104, pp. 286-291.

BOOK: Webb, R. L., and Kim, N-H. 2005. *Principles of Enhanced Heat Transfer*, 2nd ed., Taylor & Francis, New York.

EDITED BOOK: Nishikawa, K. and Ito, T. (1982) Augmentation of Nucleate Boiling Heat Transfer by Prepared Surfaces, in Heat Transfer in Energy Problems, eds. T. Mizushima and W.J. Yang, pp. 111-118, Hemisphere Publishing, Washington, DC.

CONFERENCE PROCEEDINGS: Ma, T.M. (1987) Effects of Geometrical Shapes of Reentrant Grooves on Boiling Heat Transfer from Porous Surfaces, Heat Transfer 1986, Proc. 8th Int'l. Heat Trans Conf., Vol. 4, pp. 2013- 2018.

FOOTNOTES: Footnotes should be identified in the text by superscript Arabic numerals and cited consecutively in the paper. All footnotes should be compiled on a separate sheet.

TABLES AND FIGURES

Tables and figures should not be embedded in the text, but should be included as a separate file. A short descriptive title should appear above each table with a clear legend and any foot-notes suitably identified below. All units must be included. Figures and illustrations submitted (line drawings, halftones, photos, photomicrographs, etc.) should be digital files. Figures should be completely labeled, taking into account size reduction of the published journal. Figure captions should be typed, on a separate sheet. The author can submit color figures that will print in black and white, but will be in color online. Extra author charges will be applied for figures that the author wants printed in color in the print version. Digital files are preferred for highest quality reproduction and should follow these guidelines:

- 300 dpi or higher
- EPS, TIFF, JPEG, PNG, or PSD format only
- Captions sized to fit on printed journal page

REVIEW PROCESS

The manuscript will be assigned a number and electronically sent to an assigned JEHT Regional Editor, who will obtain reviews and advise the author of the review results. The Regional Editor has authority to accept, reject, or request needed revisions. Authors will be informed via e-mail of the assigned JEHT Regional Editor. Note that all communications will be electronic and not involve any "hard copy" mailing.

FINAL MANUSCRIPTS

After notification of manuscript acceptance by the assigned Editor, the corresponding author should submit an electronic file to the Editor containing:

- Manuscript (double spaced with 1" margins all around in Word format). Figures in a separate file(s) using either EPS, TIFF, JPEG, PNG, or PSD . Use of pdf format is not acceptable.
- Completed *Manuscript Transmittal* form (signed and scanned).
- Signed *Copyright Transfer Agreement* (signed and scanned).

The author names on the title page should be accompanied by address information, including e-mail. The title page should also contain:

- A short-ended version of the title suitable for the running head, not exceeding 50 character spaces.
- Keywords

Electronically submit the above materials to the JEHT Regional Editor in a single zip file with the subject of the email "JEHT m/s **-** (Final Manuscript)", where the **-** is the assigned manuscript number.

PROOFS

One set of proofs is sent to the corresponding author. Proofs should be carefully checked and returned promptly. Alterations made in proof should be absolutely minimal.

OFFPRINTS

An offprint order form will accompany your author proofs. It should be completed and returned with your proofs. Corresponding authors of the article will receive a complete copy of the issue in which the article appears.

Journal of Enhanced Heat Transfer

Volume 17, No.4 **2010**

Journal of Enhanced Heat Transfer is abstracted and/or indexes in the Scisearch® online database, ISI Alerting Service, and Current Contents/Engineering, Computing, & Technology.
For online access to content, visit **www.begellhouse.com**

Journal of Enhanced Heat Transfer, 17(4) 293–300 (2010)
Reprints available directly from the publisher.
Photocopying permitted by license only.

Surfactant Effects on Critical and Minimum Heat Flux

J. M. BORSARI* **& P. D. FRIEDMAN**

University of Massachusetts Dartmouth, 285 Old Westport Road,
North Dartmouth, MA 02747

Experiments were conducted to determine the effect of Surfynol 465 surfactant on critical heat flux (CHF) and minimum heat flux (MHF) during voltage-controlled pool boiling at saturation temperature, using a small platinum wire connected to a controllable DC power supply. Bulk surfactant concentrations ranged from 0.001% to 0.405% as determined by measuring the equilibrium surface tension with a tensiometer using the du Noüy ring method. Results indicate that CHF increases and MHF decreases with increasing surfactant concentration, although the effect on both CHF and MHF is small relative to typical boiling heat transfer uncertainty. For example, at 0.405% Surfynol 465 CHF increases by 15% and MHF decreases by 34%, while accepted boiling heat transfer data uncertainty is about 50%. Results of the current study are compared with accepted correlations as well as previous studies that used different surfactants.

Key words: surfactant; surface tension; boiling heat transfer; film boiling; CHF; MHF

*Corresponding author: J. M. Borsari: borsarij@comcast.net

NOMENCLATURE

g	gravitational constant	**Greek symbols**	
h_{fg}	heat of vaporization	ΔT_e	excess temperature
q''_{max}	critical heat flux	ΔT_{sat}	saturation temperature of surfactant solution
q''_{min}	minimum heat flux	ρ	resistivity
R'	characteristic radius	ρ_l	liquid density
r	radius of wire	ρ_v	vapor density
T_s	surface temperature of wire	σ	surface tension

1. INTRODUCTION

Transition between nucleate and film boiling potentially causes dramatic temperature changes during flux-controlled operations, which may lead to catastrophic equipment failures. For example, exceeding critical heat flux (CHF) in a nuclear reactor may increase surface temperature by roughly 1000°C, leading to near instantaneous release of fission products into the reactor coolant. Reducing heat flux below minimum heat flux (MHF) may reduce surface temperature in excess of 100°C. One method of altering CHF and MHF is the addition of a surfactant, which reduces surface tension and modifies diffusion rates; even small concentrations of surfactants in aqueous solutions may significantly enhance heat transfer to the boiling fluid. Using a hot wire experimental setup, Yang and Maa (1983) report an increase in CHF corresponding to an increase in surfactant concentration. On the other hand, in experiments where a hot instrumented sphere was quenched in an aqueous surfactant solution, Wu et al. (1994) noted a reduction in CHF with increasing surfactant concentration. Both studies used the same surfactant and concluded that the effects of surfactants on CHF are more complex than simply altering surface tension. The Marangoni Effect, for example, reduces local concentration of surfactant on expanding bubble surfaces and thereby slows and stabilizes bubble growth (Yang, 1990). As indicated by the extensive and recent literature review (Cheng et. al., 2007), the effects of surfactants on boiling heat transfer are complex and still the subject of significant uncertainty. Readers with an interest in a more thorough literature search are referred to this reference.

This paper summarizes experiments investigating the effect of varying concentrations of Surfynol 465 surfactant (Air Products and Chemicals Inc.) on CHF and MHF during flux-controlled boiling using a small platinum wire. Results are compared to previous studies of surfactant effects (Yang, 1990; Yang and Maa, 1983) on CHF as well as more general correlations that predict the effect of surface tension on CHF (Lienhard and Dhir, 1973) and MHF (Lienhard and Wong, 1964). There is almost no literature reporting the effect of surfactants on MHF, however Qiao and Chandra (1997) report a decreasing MHF with increasing surfactant concentration in their research investigating droplets on a hot surface.

2. EXPERIMENTS

Flux-controlled boiling experiments were conducted in a temperature-controlled water bath using the apparatus shown in Fig. 1 for various surfactant concentrations. The heat source for the experiments was a small platinum wire (0.0147-mm diameter, 28.6-mm length) energized by a Matsusada Precision Inc. DC power supply. Output current and voltage were recorded using a Pico Technology Ltd. PC-based oscilloscope at a sampling rate of 15,000 samples per second. Voltage and current outputs from the power supply were calibrated and continuously monitored for consistency with a Fluke 85 III True RMS Multimeter.

Figure 2 shows the surface tension of aqueous solutions of water and Surfynol 465 for concentrations ranging from 0.001% to 1.0%.[1] The surface tension of

[1]It is important to note that the surface tension presented in Fig. 2 is the bulk surface tension measured at equilibrium. The local surface tension at the heater surface is complex and time-dependent due to adsorption/desorption processes at the fluid interface.

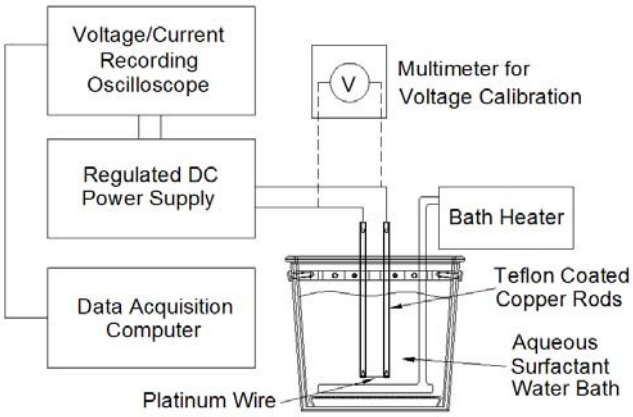

FIGURE 1. Experimental setup. Flux controlled experiments were conducted in a temperature-controlled water bath using the apparatus shown for various surfactant concentrations. For each surfactant concentration tested, a boiling heat flux vs. excess temperature curve ($\Delta T_e = T_s - T_{sat}$) was produced by slowly increasing heat flux in 0.3V increments until stable film boiling was established, and then decreasing heat flux to zero.

each solution was determined by measuring the liquid--air surface tension using a Cole Parmer tensiometer employing the du Noüy ring method. By testing a large number of concentrations at 23°C (each repeated three times), a clear semi-logarithmic trend was observed. Additionally, three concentrations were tested at elevated solution temperatures (40°C, 60°C, and 80°C) to determine the relationship between surface tension and concentration at elevated temperatures. Due to limitations of the tensiometer used, it was not possible to directly measure surface tension at 100°C. For comparative purposes, surface tension at 100°C was estimated by extrapolating data from 40°C, 60°C, and 80°C. Although extrapolated data should be viewed with caution the trends are considered reliable based on the relatively small variation in temperature (20°C) and the diminishing effect as temperature increases. No attempt was made to investigate interface age time,

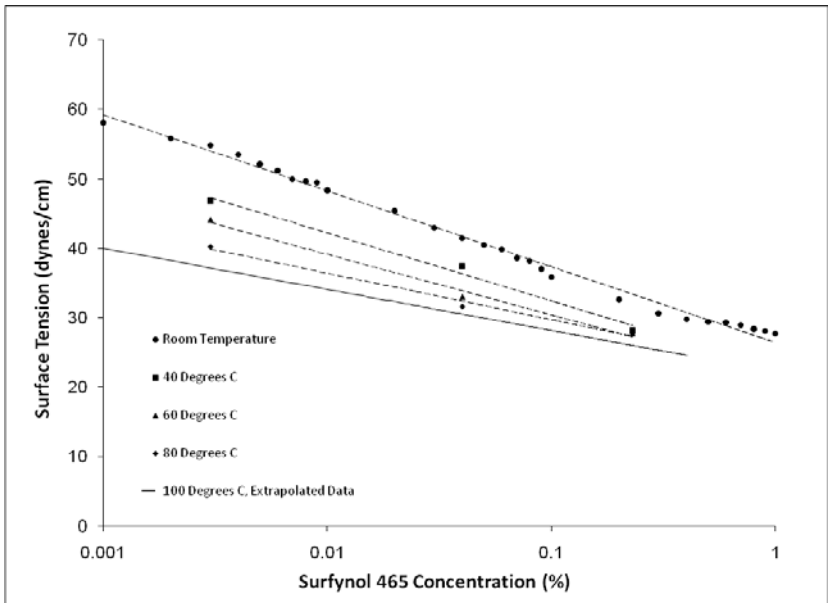

FIGURE 2. Surface tension vs. concentration of Surfynol 465 surfactant.

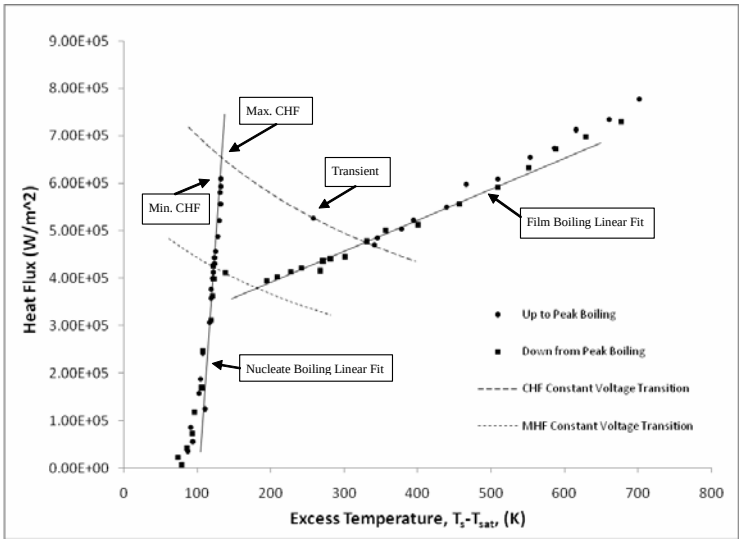

FIGURE 3. Corrected boiling curve. A curve similar to this one was generated for each experiment using the apparatus shown in Fig. 1. The actual CHF and MHF occurred between two recorded data points that were separated by the minimum voltage increment of the power supply (0.03 V).

which has been demonstrated to potentially affect the results (Cheng et al., 2007).

Boiling experiments were conducted over a wide range of surfactant concentrations that were prepared on a mass basis and cross-checked using surface tension measurements and the data in Fig. 2. For each surfactant concentration tested, a boiling heat flux vs. excess temperature ($\Delta T_e = T_s - T_{sat}$) curve was produced by slowly increasing heat flux until stable film boiling was established and then decreasing heat flux back to zero. Heat flux was controlled by adjusting voltage in 0.03 V increments. Figure 3 is a typical plot showing the "hysteresis loop" produced during a single experiment. Each point shown on the plot is calculated from the average of 75,000 current and voltage measurements recorded by the data acquisition system. Heat flux was determined based on current, voltage, and the surface area of the wire under quasi-steady conditions. (Based on typical experimental heat fluxes and temperature increments, the response time of the wire was on the order of 0.1 s, which was significantly less than the sampling interval of 5 s.) The two transient points plotted on the curve connecting the nucleate and film boiling regions are averages of properties before and after the constant voltage transition and do not represent stable conditions. The temperature of the wire was determined from the resistivity–temperature relationship of platinum, which was approximated as linear (T = 28.07E8ρ), where the resistivity (ρ) is in Ωm and temperature T is in Kelvin (Platinum Metals Review, 1984). Assuming uniform volumetric heat generation within the wire, the temperature difference between the surface of the wire and the center was less than 0.7 K (Borsari, 2008).

3. RESULTS AND ANALYSIS

Boiling curves were generated for deionized water and aqueous water/Surfynol 465 solutions with a mass concentration ranging from 0.001% to 0.405%. The minimum controllable voltage increment for the power supply was 0.03 V, which was large enough to generate an error of up to 4% in the observed CHF and 4.5% in the observed MHF. To reduce this uncertainty in CHF, the maximum and minimum possible CHF as shown in Fig. 3 were averaged. The minimum possible CHF was based on the voltage before the observed boiling crisis. The maximum possible CHF was based on the lowest voltage datum after the transition and determined from the intersection of the extrapolated nucleate boiling trend line and a constant voltage transition curve. This constant voltage transition curve was calculated from the known resistivity/temperature relationship of plati-

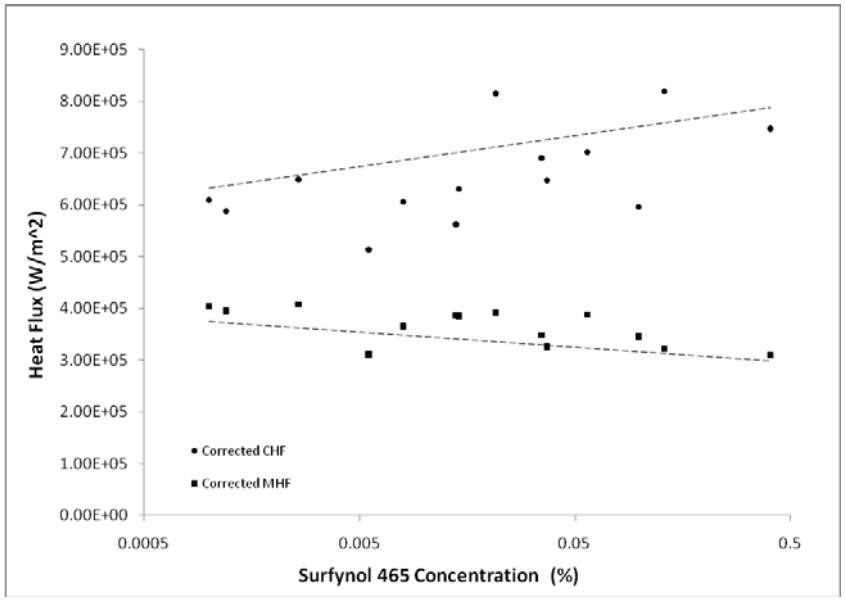

FIGURE 4. Effect of Surfynol 465 on CHF/MHF. Each corrected CHF and MHF point on the plot is an average of 5 to 10 individual experiments. Typical random uncertainty is 6% for CHF and 4% for MHF while the maximum fixed uncertainty based on very conservative instrumentation accuracy assumptions is 13.15% for CHF and 11.15% for MHF. Typical overall uncertainty is 14.45% for CHF and 11.85% for MHF (Borsari, 2008).

num. A similar procedure was used for MHF. Overall, this process reduced the maximum uncertainty in the voltage from 0.03 V to 0.015 V.

For each of 14 concentrations, 5 to 10 complete boiling curves were produced and individually analyzed to determine CHF and MHF as discussed above. As shown in Fig. 4, the results indicate a trend of increasing CHF with increasing surfactant concentration and decreasing MHF with increasing surfactant concentration. Typical overall uncertainty in these results is 14.45% for CHF and 11.85% for MHF (Borsari, 2008), due to a combination of both bias errors as well as random data uncertainty. Based on very conservative assumptions of power supply readability, measured clamping resistance and accuracy of the voltage and current recording instrumentation, the maximum bias error was estimated to be 13.15% for CHF and 11.15% for MHF. Typical random uncertainty was 6% for CHF and 4% for MHF, although maximum random uncertainty for both was approximately 12%.

The present CHF results are compared to previously presented data and analytical predictions in Fig. 5. The correlation by Lienhard and Dhir (1973) is an adjustment of Kutateladze and Zuber's infinite horizontal plate prediction and is derived for a small finite horizontally oriented cylinder:

$$q''_{\max} = \left(\frac{0.94}{(R')^{1/4}} \right) \frac{\pi}{24} \rho_v^{1/2} h_{fg} \left[\sigma g (\rho_l - \rho_v) \right]^{1/4} \quad (1)$$

where $R' = r[g(\rho_l - \rho_v)/\sigma]^{1/2}$. It should be noted that Lienhard and Dhir (1973) advise that Eq. (1) does not pertain to heaters with very small characteristic geometries, such as the geometry used in this research, because the hydrodynamic properties used to formulate the correlation do not apply to very small-scale geometries. Nevertheless, because of the dearth of relevant data, Eq. (1) is used for comparative purposes. The equation predicts CHF of 2.12e6 W/m^2 while CHF from pure water experiments is 6.21e5 W/m^2, approximately 30% of the predicted value; however, the trend with surface tension is opposite of our observed experimental trends.

Using a similar experimental apparatus with a nickel heating wire having a 0.117-mm diameter, Yang and Maa (1983) show a trend, comparable to this research, of CHF decreasing with increasing surface tension. Their data is based on two surfactants: sodium

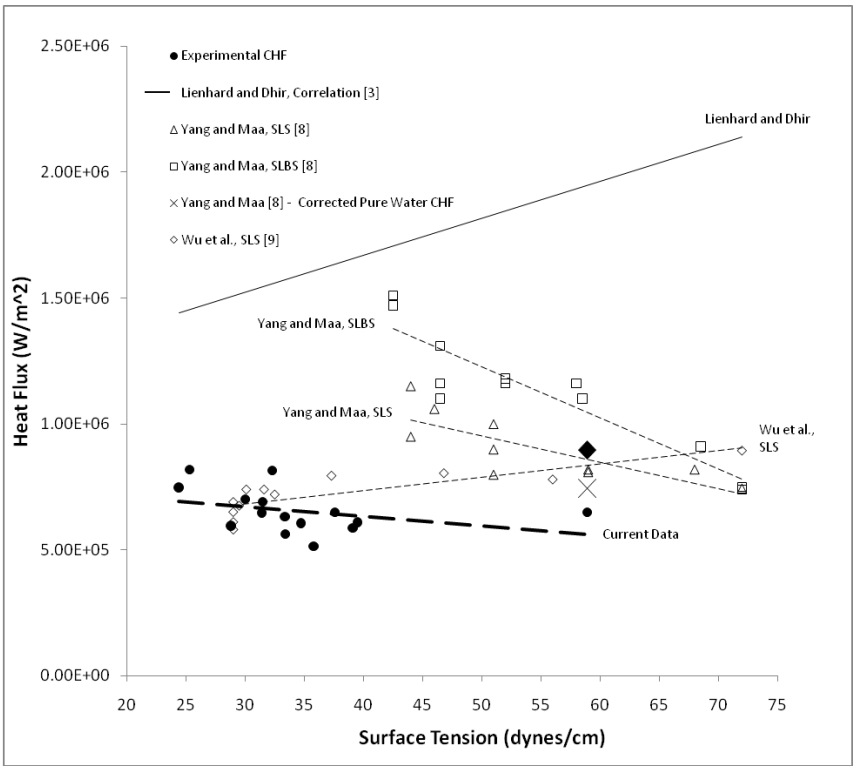

FIGURE 5. CHF results comparison to correlation and past experimental data. Experimental CHF results are compared to Lienhard and Dhir's pure water correlation (Lienhard and Dhir, 1973) as well as previous studies regarding surfactant effects on CHF. Yang and Maa (1983) used an experimental apparatus similar to this research and obtained results supporting the trend of decreasing CHF with surface tension. The present results are plotted for actual surface tension at saturation temperature while the results of Yang and Maa (1983) are reported for surface tension at room temperature. Without knowing the effects of temperature on surface tension for SLS and SLBS, we were unable to adjust the data of Yang and Maa to a consistent reference point. For comparative purposes, their data would pass through the large *X*, which is based on pure water. Wu et al. (1994) used a quenching method to measure CHF and reported a trend of increasing CHF with surface tension. Quenching tests using two different surfactants given by Wu et al. (1994) report trends consistent with the SLS results but with higher CHF values.

lauryl benzene sulfonante (SLBS) and sodium lauryl sulfate (SLS). The data provided by Yang and Maa is plotted for room temperature surface tension values, not the actual experimental temperature values; in contrast, the data from the current research is plotted for surface tension at saturation temperature as determined in Fig. 2. For comparative purposes, the data from Yang and Maa could be anchored to the point in the figure annotated with a large "X," based on the known surface tension characteristics of pure water. Because the relationship between surface tension and surfactant concentration for SLS and SLBS is not reported in the literature, the rest of their data was not modified. All of the heat flux-controlled experiments summarized in Fig. 5 show a trend of increasing CHF with decreasing surface tension, which is opposite of the trend of Eq. (1) based on surface tension alone. Although each of the surfactants displays a similar trend, the magnitude of the variation in CHF with surface tension is different. Yang and Maa (1983) concluded that this difference is most likely due to differences in the Marangoni effect[2] as well as other physical properties of the surfactant, notably diffusivity. In contrast to the present results and those of Yang and Maa, using an alterna-

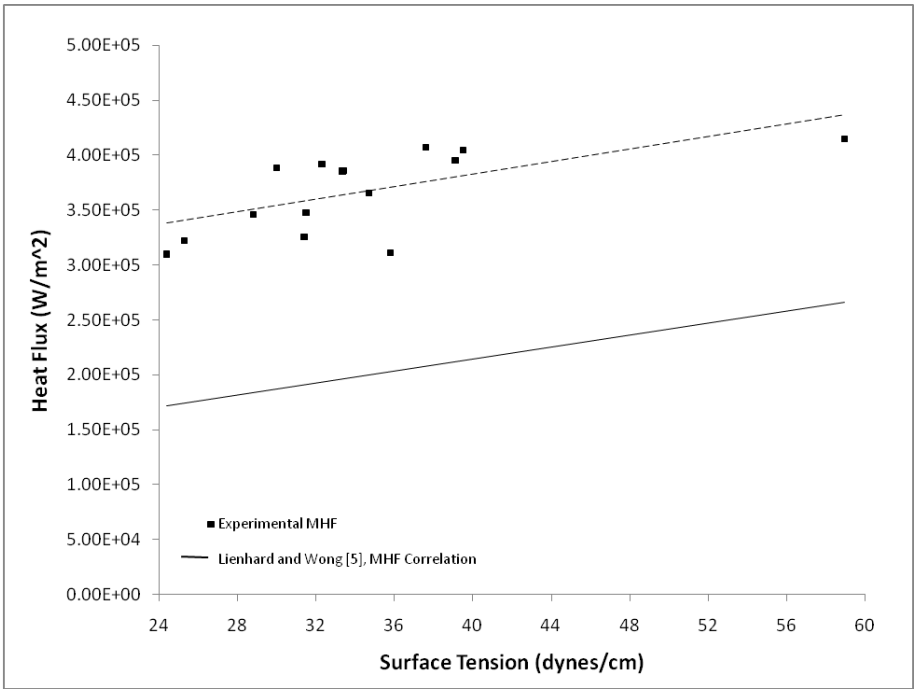

FIGURE 6. Experimental MHF comparison to correlation. Experimental MHF results are compared to the correlation for pure water formed by Lienhard and Wong (1964). Note that the experimental trendline has a slope that is very similar to that of the correlation prediction, although the values are significantly higher.

tive experimental procedure in which instrumented copper spheres were quenched in surfactant solutions, Wu et al. (1994) report CHF trends of increasing CHF with increasing surface tension.

Figure 6 contains MHF determinations from the present experiments and compares them with a correlation from Lienhard and Wong (1964). Lienhard and Wong derived their correlation based on stability theory with the assumption that a complete film has developed on the wire. This film oscillates in a sinusoidal manner, and the onset of the film collapse (MHF) depends on a critical wavelength, yielding:

The resulting MHF prediction for pure water is 2.626e5 W/m^2 and the average MHF for the pure water experiments is 4.08e5 W/m^2. Again, although the correlation is not intended for the small geometries, we use it for comparative purposes. The experimental MHF is approximately 55% higher than the value predicted by Eq. (2) and follows a similar slope. Qiao and Chandra (1997) also report a trend of decreasing MHF with increasing surfactant concentration, but this is based on research investigating the behavior of droplets evaporated on a hot surface; while the trends are similar they cannot be directly compared.

$$q''_{\min} = 0.057 \frac{\rho_v h_{fg}}{r} \left[2g \frac{\rho_l - \rho_v}{\rho_l + \rho_v} + \frac{\sigma}{(\rho_l + \rho_v) r^2} \right]^{\frac{1}{2}} \left[\frac{g(\rho_l + \rho_v)}{\sigma} + \frac{1}{2r^2} \right]^{-\frac{3}{4}} \quad (2)$$

[2]The Marangoni effect is a restoring force encountered during bubble growth on a heater submerged in an aqueous surfactant solution. As the interface between vapor and liquid stretches, surfactant is adsorbed from the liquid; because there is a finite rate of diffusion, the local surface tension in the stretching regions is higher than that of the non-stretching regions. Therefore, the local increase in surface tension at these regions of lower surfactant concentration has the effect of impeding further bubble growth (Yang, 1990).

4. CONCLUSIONS

Trends developed from experimental data indicate that increasing concentrations of Surfynol 465 in aqueous solutions up to 0.405% increases CHF and decreases MHF in flux-controlled boiling, although the effect is small and less than the typical uncertainty associated with boiling heat transfer (±50%) (Incropera and DeWitt, 2002). The results for CHF are consistent with other flux-controlled experiments in the literature but counter to accepted correlations based on surface tension. The results for MHF are consistent with the predictions based on surface tension as well as related research by Qiao and Chandra (1997).

REFERENCES

Borsari, J. M., *Experimental Investigation of the Effects of Surfactants on CHF and MHF*, MS, University of Massachusetts Dartmouth, 2008.

Cheng, L., Mewes, D., and Luke, A., Boiling phenomena with surfactants and polymeric additives: A state-of-the-art review, *Int. J. Heat Mass Transfer*, vol. 50, pp. 2744–2771, 2007.

Incropera, F. P. and DeWitt, D. P., *Introduction to Heat Transfer*, 4th Edition, New York: John Wiley and Sons, Inc., pp. 558–566, 2002.

Lienhard, J. H. and Wong, P. T. Y., The dominant unstable wavelength and minimum heat flux during film boiling on a horizontal cylinder, *ASME J. Heat Transfer*, vol. 86, pp. 220–226, 1964.

Lienhard, J.H. and Dhir, V. K., Hydrodynamic prediction of peak pool-boiling heat fluxes from finite bodies, *Trans. ASME C*, vol. 95, pp. 152–158, 1973.

Platinum Metals Review. *Notes for Electrical Resistivity v Temperature Attribute of Platinum.* Retrieved Dec 9, 2007 from http://www. platinum-metalsreview.com/jmpgm/index.jsp, 1984.

Qiao, Y. M. and Chandra, S., Experiments on adding a surfactant to water drops boiling on a hot surface, *Proc. Roy. Soc. A*, vol. 453, pp. 673–689, 1997.

Wu, W. T., Lin, H. S., Yang, Y. M., and Maa, J. R., Critical heat flux in pool boiling of aqueous surfactant solutions as determined by the quenching method, *Int. J. Heat Mass Transfer*, vol. 37, no. 7, pp. 2377–2379, 1994.

Yang, Y. M. and Maa, J. R., Pool boiling of dilute surfactant solutions, *ASME J. Heat Transfer*, vol. 105, pp. 190–192, 1983.

Yang, Y. M., Dynamic surface effect on boiling of aqueous surfactant solutions, *Int. Comm. Heat Mass Transfer*, vol. 17, no. 6, pp. 711–727, 1990.

Journal of Enhanced Heat Transfer, 17(4) 301–311 (2010)
Reprints available directly from the publisher.
Photocopying permitted by license only.

Experimental Study of Fluid Flow and Heat Transfer in a Rectangular Channel with Novel Longitudinal Vortex Generators

CHENGYING QI*, CHUNHUA MIN, SHANGQUN XIE, & XIANGFEI KONG

School of Energy and Environmental Engineering, Hebei University of Technology, Tianjin 300401, P. R. China

A novel combined longitudinal vortex generator (LVG), comprising a rectangular wing mounted with an accessory rectangular wing, was presented and studied. Gas flow and heat transfer characteristics of this LVG in a rectangular channel were obtained experimentally and compared with those of the original rectangular LVGs under identical pressure gradient conditions. Results showed that a 45^{o} orientation to the flow direction has optimal heat transfer characteristics for the original rectangular LVGs. In contrast, the combined LVGs, especially the upstream accessory wings, show higher heat transfer and lower gas flow resistance performances, with an optimal secondary orientation of 30^{o}. For the combined LVGs, because the strong longitudinal vortices generated by the LVGs enhance the heat transfer between gas and channel walls, the temperature gradually increases from the centerline of the heater wall to the edge. The wall equivalent temperature with accessory wings is lower than that without accessory wings.

Key words: longitudinal vortex generator; accessory wing; heat transfer enhancement; pressure drop

*Corresponding author: Chengying Qi: qicy@hebut.edu.cn

NOMENCLATURE

a, b	position of the accessory wing on the main wing, mm	U	velocity, m/s
c	length of the accessory wing, mm	V	electric voltage, V
c_p	specific heat of the fluid, J/(kg·K)	W	channel width, mm
d	width of the accessory wing, mm	w	rectangular wing width, mm
D_e	equivalent diameter, mm	x, y, z	Cartesian coordinates
f	friction factor	**Greek symbols**	
H	channel height, mm	α	angle of attack of the main wing, ^{o}
I	electric current, A	β	angle of attack of the accessory wing, ^{o}
L	channel length, mm	ν	kinematic viscosity, m^2/s
l	span of a rectangular wing, mm	ρ	density, kg/m^3
p	pressure, Pa	ζ	friction factor ratio between upper and lower channels
q	heat flux, W/m^2	**Subscripts**	
Q	heat transfer rate, W	e	equivalent
R	heat transfer enhancement ratio	i	index for upper passage (up) or lower passage (low)
Re	Reynolds number	in	inlet
s	distance, mm	low	lower passage
t	thickness, mm	out	outlet
T	temperature, K	up	upper passage

1. INTRODUCTION

Heat exchangers are widely used components in many industrial areas such as chemical engineering, automobile manufacturing, refrigeration, electronic chip cooling, and internal cooling for gas turbine blades. Universal types of heat exchangers incorporating plate-fins or fin-tubes are designed for the above industrial processes and systems, and for these types the flow is channeled between plates (Zhu *et al*., 1995). Longitudinal vortex generators (LVGs) can be mounted on channel walls to generate longitudinal vortices which create a secondary flow and disturb the boundary layer growth, thereby enhancing the heat transfer between the flowing fluid and channel walls. Generally, there are four basic forms of wing-type LVGs, including delta wing, rectangular wing, and winglet pairs (Pesteei *et al*., 2005). These triangular or rectangular appendages can be mounted on the walls with specific orientations to the direction of the main flow.

LVGs have been extensively studied due to their high heat transfer performance. Eibeck and Eaton (1987) have performed experiments and found the longitudinal vortices have a significant influence on heat transfer enhancement. Tigglebeck *et al*. (1994) have also provided a thorough analysis on the influence of LVG geometry in a rectangular channel flow. They found that a pair of delta winglets performs slightly better than a pair of rectangular winglets at higher angles of attack and Reynolds numbers. Results given by Biswas *et al*. (1996) indicated that flow loss due to a winglet pair was less than that due to a single wing, and zones of poor heat transfer that occur with single wings could be eliminated by using winglet pairs. Also, their application appeared to be a more attractive enhancement technique. Gentry and Jacobi (1997, 2002) experimentally studied, using a naphthalene sublimation technique, heat transfer enhancement characteristics of delta wing vortex generators in a flat-plate flow. Results showed that the average heat and mass transfer could be enhanced by 50–60% at low Reynolds numbers in comparison with the original configuration. Liou *et al.* (2000a,b) performed comparative studies in terms of heat transfer augmentation and uniformity and friction loss on 12 different LVG configurations. It was found that direction and strength of the secondary

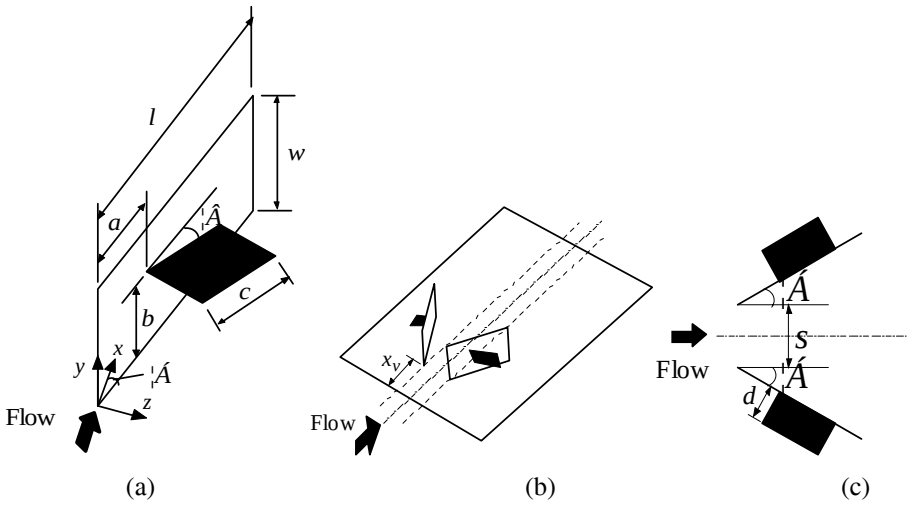

FIGURE 1. Schematic view of present combined longitudinal vortex generators: (a) angles of attack of main and accessory wings; (b) layout of common-flow-down; (c) top view of the vortex generators in a channel.

flow are the more important fluid dynamic factors affecting heat transfer, followed in importance by fluid velocity, and then turbulent kinetic energy. Liou *et al*. (2000a,b) also observed that secondary flow and convective mean velocity are more important to heat transfer enhancement than turbulent kinetic energy. Torii *et al*. (2002) and Kwak et al. (2005) proposed a novel delta winglet configuration, called common-flow-up, which is effective in 1) delaying boundary layer separation from the tube, 2) reducing form drag, and 3) removing zones of poor heat transfer from the near-wake of the tube. Heat transfer enhancement and pressure loss cost were also compared between common-flow-up and common-flow-down configurations. Chen and Shu (2004) experimentally investigated the effects of an external delta wing vortex generation on flow and heat transfer characteristics in fan flows and uniform flows. It was observed that the increase in turbulent kinetic energy by the delta wing has little effect on heat transfer in the inherently vertical fan flows. Pesteei *et al*. (2005) measured local heat transfer coefficients on a fin-tube heat exchanger with winglets using five different positions of winglet-type vortex generators and found that the experimental results show a substantial increase in heat transfer with their use. Wang *et al*. (2007) found that LVG configurations play an important role in heat transfer enhancement that can greatly improve heat transfer rates by 10–45%. Furthermore, heat transfer performance of channels with LVGs on both sides is better than those just on one. Lawson and Thole (2008) investigated the use of delta winglets to augment heat transfer on the tube surface of louvered fin heat exchangers. Results indicated that delta winglets placed on louvered fins produce augmentations in heat transfer along the tube wall as much as 47% with a corresponding increase of 19% in pressure loss.

The above literature has only concentrated on fluid flow and heat transfer of simple LVGs. To further improve heat transfer enhancement, Vasudevan et al. (2000) numerically investigated the delta winglets with piercings placed in triangular duct flow. These piercings were found to create a more complex flow within the channel. High heat transfer augmentations were still observed with piercings and they concluded that winglets with piercings are a practical method of augmenting heat transfer performance. Lawson and Thole (2008) compared heat transfer coefficients with and without piercings and found that piercings reduce average heat transfer augmentations, but significant increases still occurred without winglets present.

In the present work, a novel combined rectangular wing, comprising an original rectangular wing mounted with an accessory wing, is introduced, and fluid flow and heat transfer performances are experimentally investigated. Schematic views of the combined LVG are shown in Fig. 1. A combined LVG consists of a main rectangular wing with a smaller rectangular accessory

wing mounted perpendicular to the main wing. In the figure, the accessory wings are mounted upstream of the main wings, although it should be noted that they can be mounted downstream as discussed in the following sections. In our experiments, the accessory wing is welded to the main wing. The main angle of attack of the main wing is denoted by α, while the secondary angle of attack is denoted by β, which is defined as the angle between the accessory wing and the channel wall mounted with LVGs. We find the inclination of the two wings obviously affects gas flow and heat transfer characteristics of the heat exchanger. Other geometrical aspects are discussed in the following sections.

2. EXPERIMENTAL APPARATUS AND INSTRUMENTATION

Heat transfer experiments were performed in an open rectangular channel as depicted in Fig. 2. The experimental system consists of a contraction cone containing a honeycomb, entrance section and test section, a diffuser and exhaust. Air is drawn in by a variable speed fan and passes through the test section of the channel. The contraction cone, honeycomb and entrance section provide smooth, streamline flow through the channel. The heater is a layered structure consisting of two stainless steel plates with an electric heater element sandwiched between them, which is also shown in Fig. 2. The heater is centrally fixed in the middle of the channel, thereby dividing the channel into two identical passages. The vortex generators are mounted solely in the upper passage. The air passage heights can be adjusted by inserting division plates in the upper and lower passages, and in the present experiment, the height of the two passages is fixed at 40 mm. To determine the heat transfer enhancement of the vortex generators, the experimental results of upper and lower channels are directly compared. It should be noted that since the two passages have the same inlet and outlet

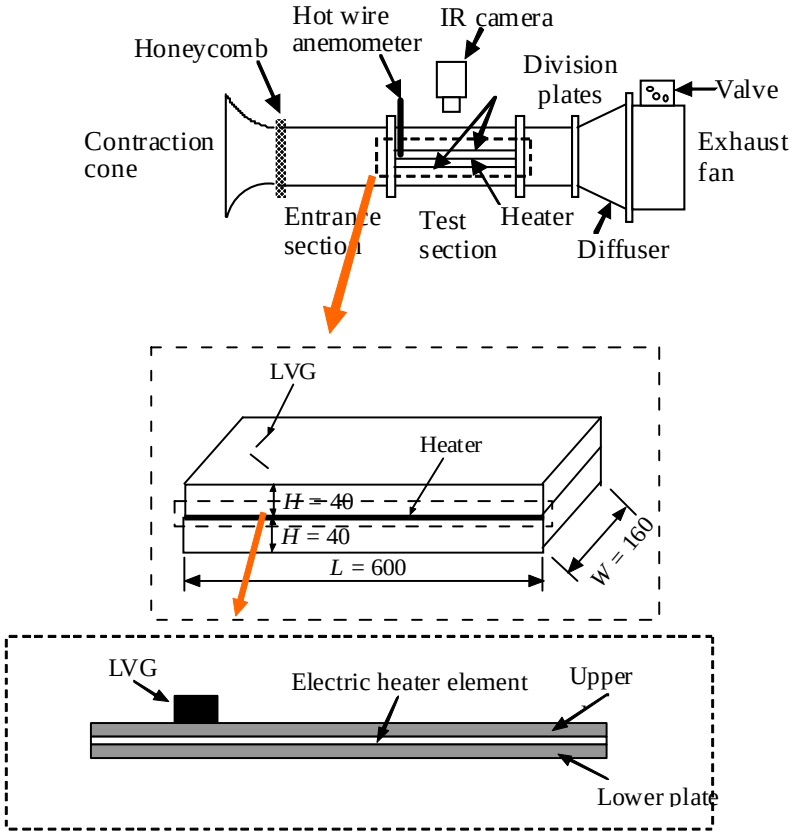

FIGURE 2. Schematic diagram of the experimental system.

profiles, the experimental work can be considered to be performing under identical pressure gradients within the passages. To enable thermal visualization of the upper heating surface, the iron plates are painted black, and the top wall of the channel is formed from transparent polyethylene film.

The rectangular test channels are mainly made of stainless steel, which have dimensions 600 × 160 × 640 mm^3 (length × width × thickness). The dimensions of the LVGs are 40 × 30 × 1.2 mm^3, while the accessory wings are 20 × 10 × 1.2 mm^3. The minimum distance between the two wings is s = 10 mm. To obviate heat loss, the side walls are covered with a polystyrene heat insulating layer. In the present experiment, the positioning of the LVGs is x_v = 40 mm along the upper heating plate, with the accessory wings being mounted at a = 15 mm and b = 20 mm from the lower leading corner of the LVG. All the above dimensions are shown in Fig. 1.

A hot wire anemometer was used to measure the channel inlet velocity. Two T-type thermocouples were installed at the inlet to measure bulk inlet temperatures, and twenty-seven thermocouples were installed uniformly at the outlet of the upper and lower channels to obtain bulk average outlet temperatures.

Quantitative thermal visualization images were obtained using an infrared imaging camera. The binary data files of the thermal images created by the camera's onboard processor were stored in a specialized TIFF format. Specific file-format information provided by FLIR was decoded for subsequent thermal analysis.

Both inlet and outlet average temperatures were obtained by T-type thermocouples and the uncertainty of the temperature is about 0.2°C. The inlet velocities at the centers were measured by a hot wire anemometer with an uncertainty of 0.01 m/s.

3. DATA REDUCTION

The Reynolds number in the present study is based on the equivalent diameter of the channel inlet and inlet velocity. It should be noted that when the upper passage is arranged with LVGs, velocities there will be lower than that of the lower passage due to the resistance of the LVGs which will increase the fraction coefficient. This velocity difference depends on the type and structure of the LVG. Hence, for convenience of analysis, the Reynolds number of the lower passage is adopted for different test cases and therefore the Reynolds number will be determined as:

$$Re = \frac{U_{\text{low}} D_{\text{e}}}{\nu} \tag{1}$$

where U_{low} is the inlet velocity of the lower passage, D_{e} is the hydraulic diameter of the lower passage.

Heat input Q is calculated from the power supply as:

$$Q = IV \tag{2}$$

Convective heat flux q can be expressed as:

$$q_i = c_p \rho U \left(T_{\text{out},i} - T_{\text{in},i}\right) \tag{3}$$

where T_{out} and T_{in} are the outlet and inlet average temperatures measured by T-type thermocouples, the subscript i denotes the upper or lower passage.

In the present work, heat transfer rates rather than heat transfer coefficients are employed to ascertain heat transfer enhancement. A heat transfer enhancement ratio R is defined as:

$$R = \frac{q_{\text{up}} - q_{\text{low}}}{q_{\text{low}}} \tag{4}$$

In the infrared imaging camera, some parameters need to be set according to the operating conditions, and these parameter values can result in measurement errors. To minimize the errors and for calculation convenience, an equivalent temperature T_{e} is defined as:

$$T_{\text{d}} = T_0 - T \tag{5a}$$

$$T_{\text{e}} = T_{\text{d}} - \overline{T}_{\text{d1}} \tag{5b}$$

where T and T_0 are the local wall temperatures for the upper passage with and without mounted LVGs, respectively, and $\overline{T}_{\text{d1}}$ is the average of T_{d} at x = 34 mm, where the wall temperature of the first row is recorded.

The friction factor f is defined as:

$$f = -D_{\text{e}} \frac{\Delta p / L}{2\rho U^2} \tag{6}$$

Since the pressure drop Δp, channel length L, equivalent diameter D_{e}, and gas density ρ of the upper passage are equal to those of the lower passage, the friction factor ratio between the upper and lower passages is expressed as:

$$\zeta = \frac{f_{\text{up}}}{f_{\text{low}}} = \frac{U_{\text{low}}^2}{U_{\text{up}}^2} \tag{7}$$

In our experiment, the fluid properties are assumed constant. The experimental uncertainties for Re, R, and ζ are estimated using a random uncertainty propagation technique proposed by Kline and McClintock (1953). In general, if F is a function of n independent variables, each of which is marked as X_i, the relative uncertainty of F is given by:

$$\frac{\delta F}{F} = [\sum_{i=1}^{n} (\frac{\delta X_i}{X_i})^2]^{1/2} \tag{8}$$

The uncertainties in the Reynolds number are mainly associated with the velocity and equivalent diameter. With W = 160 mm, H = 40 mm, δW = 0.1 mm, δH = 0.1 mm, the relative uncertainty of D_e is $\frac{\delta D_e}{D_e} = (\frac{\delta W}{W})^2 + (\frac{\delta H}{H})^2 + \frac{\delta W^2 + \delta H^2}{(W+H)^2}]^{1/2}$. For Re = 6900, U = 1.50m/s, δU = 0.01 m/s, and hence, $\frac{\delta U}{U}$ = 0.7%. Based on Eq. (8), the relative uncertainty of Re is $\frac{\delta \mathrm{Re}}{\mathrm{Re}} = [(\frac{\delta U}{U})^2 + (\frac{\delta D_e}{D_e})^2]^{1/2} = 0.8$.

For the heat transfer enhancement ratio R, individual uncertainties in flow velocity and air temperature were considered. For the upper passage without LVGs, $T_{out} - T_{in} = 6.8^oC$, $\delta T = 0.2^oC$. Using the above method, a value of the relative uncertainty for q is obtained of $\frac{\delta q}{q} = [(\frac{\delta U}{U})^2 + \frac{\delta T_{out}^2 + \delta T_{in}^2}{(T_{out} - T_{in})^2}]^{1/2}$ at Re = 6900. Hence, the relative uncertainty in R is 5.9%.

Based on Eq. (7), only the velocity was considered in regard to the friction factor ratio. The uncertainty estimation of ζ is about 1.3% at Re = 6900.

The relative difference between the total heat input by the heater and heat gained by gas represents the heat balance of the present test system and is less than 9% for all tests.

4. RESULTS AND DISCUSSION

To validate the reliability of the present experimental setup, the R-Re curve without LVGs is presented in Fig. 3 showing that the heat transfer difference of the two passages decreases with the Reynolds number. This is due to the fact that natural convection is the more dominant heat transfer process at low Reynolds numbers. However, we find these differences are actually lower than heat transfer enhancement ratio with LVGs mounted, as will be discussed below. The above comparison proves the reliability of the experimental setup and method.

The fluid flow and heat transfer characteristics of different LVGs are analyzed next. Figures 4 and 5 show the effect of the orientation of the original rec-

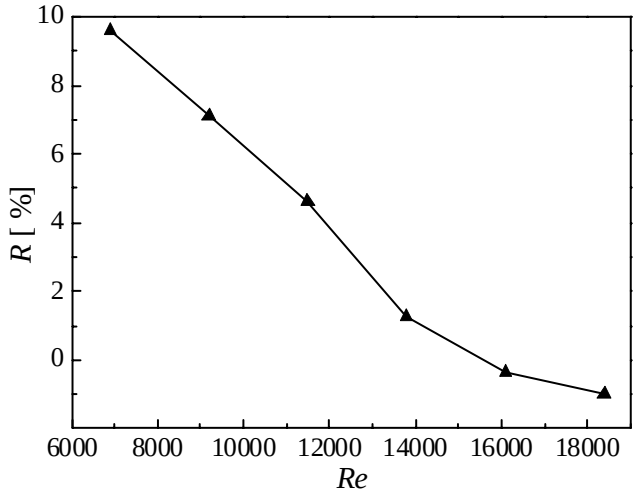

FIGURE 3. Comparison of the two passages without LVGs.

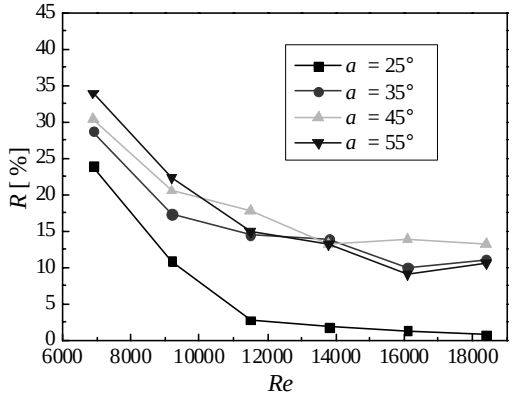

FIGURE 4. Effect of the angle of attack of the main wing on heat transfer.

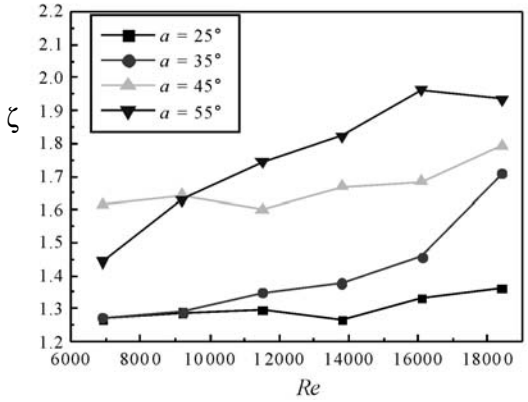

FIGURE 5. Effect of the angle of attack of the main wing on flow resistance.

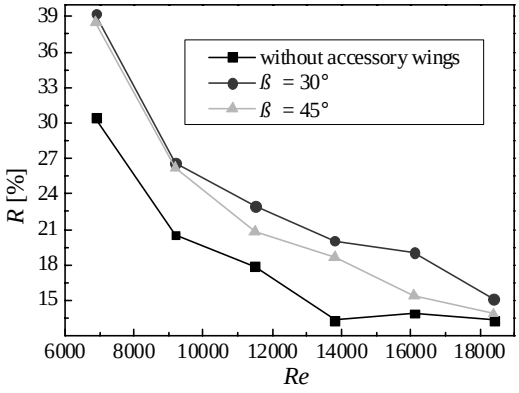

(a)

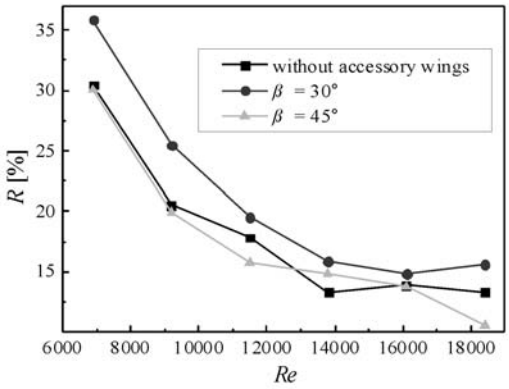

(b)

FIGURE 6. Heat transfer enhancement of the combined LVGs: (a) upstream; (b) downstream.

tangular wings on heat transfer and flow resistance, respectively. It can be seen that the a 45° angle of attack shows slightly better heat transfer characteristics with the exception of ratios for a 55° angle of attack which are marginally higher than those of 45° at lower Reynolds numbers. However, the friction coefficient of the 55° angle of attack is significantly higher than that of the 45° angle of attack. The above analysis shows that the 45° angle of attack is the more optimal angle for the original rectangular wings, and hence the following analyses are mainly carried out with this angular setting. The above trends are similar to results given by Tiggelbeck *et al*. (1994), which can be used to substantiate the present work.

The accessory wings, either mounted upstream or downstream of the main wings, can obviously affect gas flow and heat transfer as can be clearly seen in Figs. 6 and 7, respectively. The effects of the secondary angle of attack on gas flow and heat transfer can also be seen. The results show that the combined LVGs have higher heat transfer and lower gas flow resistance performances compared with the original rectangular LVGs. Moreover, both the heat transfer and flow resistance with upstream accessory wings are higher than those located downstream. Additionally, a 30 secondary angle of attack offers better heat transfer performance and larger gas flow resistance compared with a setting of 45°. The heat transfer and gas flow

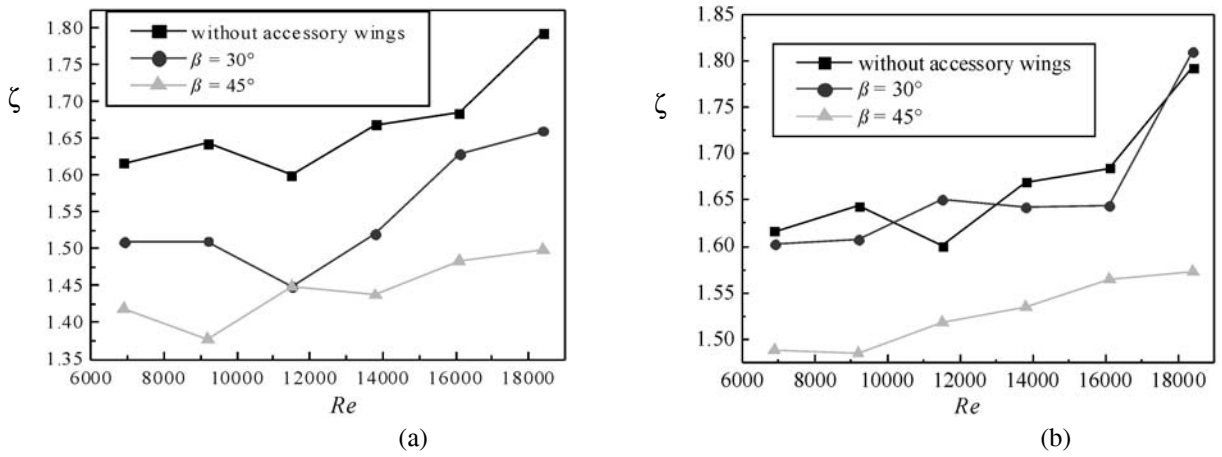

FIGURE 7. Gas flow resistance of the combined LVGs: (a) upstream; (b) downstream.

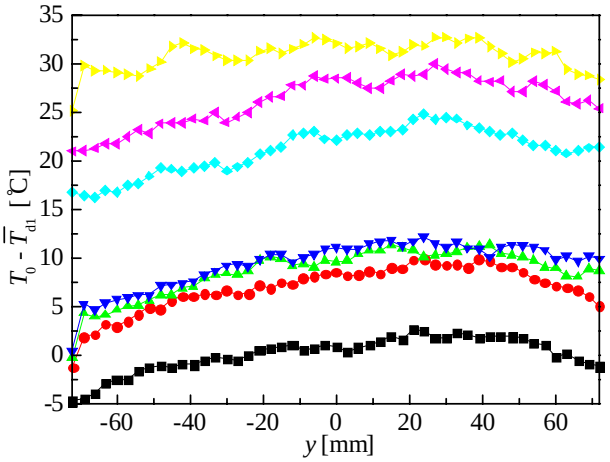

FIGURE 8. Variation of the wall temperature along cross-flow direction at Re = 13,800: no LVG.

resistance performances of the combined wings are better than those of the original rectangular wings, therefore, it can be concluded that the 30 secondary angle of attack is the better setting for combined LVGs studied in the present research.

Focus is now turned to the temperature distribution of the upper heater wall. The actual width of the heater is 160 mm, although to reduce boundary effects on thermal images, the visualization width is adjusted to 144 mm. Figure 8 shows the variation in temperature difference between T_0 and $\overline{T}_{d1}$ of the upper heater wall without LVGs. It can be seen that the temperature gradually decreases from the centerline of the heater to the edge. This is due to the fact that the heater is connected with the stainless steel side walls of the channel where heat conduction is considerably stronger. To highlight the effects of LVGs on the wall temperature distribution, a temperature difference is obtained by subtracting the local wall temperature with LVGs mounted from the local wall temperature without LVGs. This temperature difference is then subtracted from $\overline{T}_1$ giving the above equivalent temperature.

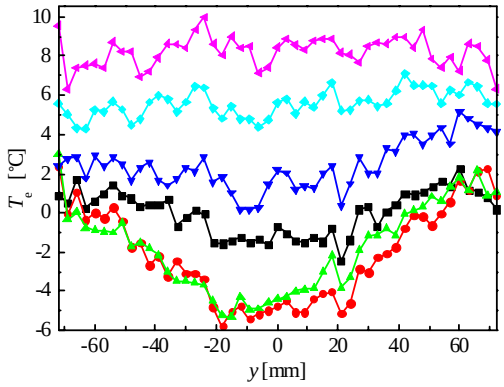

(a)

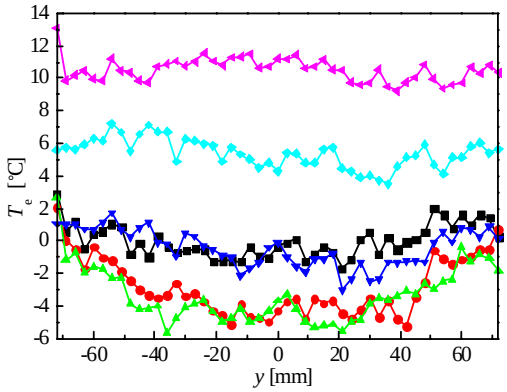

(b)

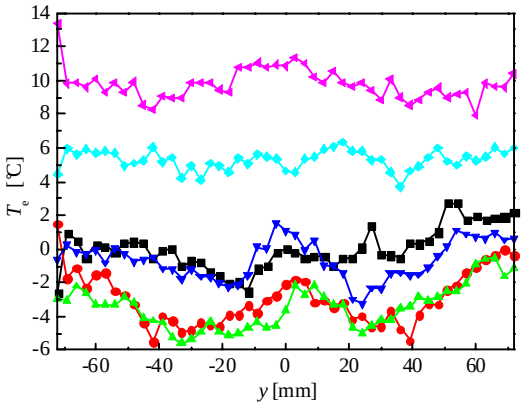

(c)

FIGURE 9. Variation of the wall temperature along cross-flow direction at Re = 13,800.

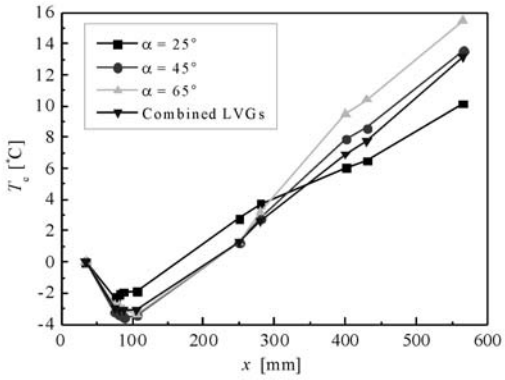

(a)

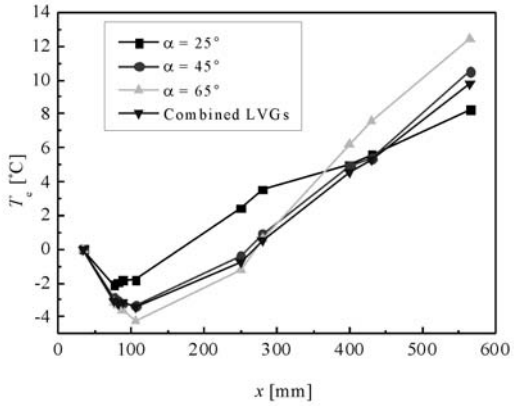

(b)

FIGURE 10. Mean equivalent temperature distribution along the flow direction.

As typical cases, Fig. 9 shows equivalent cross-flow temperature distributions along the heater length with LVGs at different angles of attack. First, it is obvious that the temperature gradually increases from the centerline to the edge, which is contrary to the above observation. This is due to strong longitudinal vortices generated due to the presence of LVGs and thus enhancement of heat transfer between gas and channel walls. Second, the figures reveal that the wall temperature distributions are affected by the angular relation between the main and accessory wings. Compared with a 25° angle of attack, the range of lower local temperatures is larger for a 45° angle of attack because the vortices generated are relatively stronger. For the combined LVGs, the local temperature behind the LVGs is

seen to be significantly cooler as a consequence of the air being forced to sweep over the heater wall. Hence, the combined LVGs have the highest heat transfer characteristics among the LVGs under study. Finally, we see that wall temperatures obtained for the combined LVGs are the coolest, followed by the original LVGs with a 45° angle of attack and then a 25° angle of attack. To clearly illustrate these observations, mean equivalent temperature distributions along the flow direction for the above cases are shown in Fig. 10 for Re = 6900 and Re = 13,800. The values of $\overline{T}_e$ are seen to decrease with increasing angle of attack of the original LVGs as x is lowered, the reason being that the longitudinal vortices generated become stronger as the angle of attack increases. When x is larger, the distribution of $\overline{T}_e$ is opposite to that of low x. This is due to increasing gas temperatures at a greater angle of attack because x is larger, and hence the heat at larger x cannot be effectively transferred. The figures also show that wall temperatures are lower with accessory wings than without them, revealing the better performance of the combined LVGs. As a final note, the vortex structure created by the LVGs is very complicated and a detailed analysis is needed which will be provided in another work.

5. CONCLUSIONS

Fluid flow and heat transfer characteristics of novel combined LVGs have been experimentally studied under identical pressure gradient conditions. The main conclusions are drawn as follows:

(1) For the original rectangular LVGs, a 45° angle of attack offers the better heat transfer characteristics, despite pressure gradients being less than that with a 55° angle of attack.

(2) Combined LVGs, especially upstream accessory wings, present the higher heat transfer and lower gas flow resistance performances compared with original rectangular LVGs. A setting of a 30° secondary angle of attack offers the better performance characteristics among the LVGs studied in the present research.

(3) For the heater wall mounted on LVGs, the temperatures gradually increase from the centerline to the edge, due to strong longitudinal vortices generated by the LVGs, and thereby enhance heat transfer between fluid and channel walls. Wall temperatures are lower when accessory wings are mounted on LVGs when compared with the situation without accessory wings.

ACKNOWLEDGMENT

The present work is financially supported by the National Natural Science Foundation of China (No. 50676027).

REFERENCES

Biswas, G., Torii, K., Fujii, D., and Nishino, K., Numerical and experimental determination of flow structure and heat transfer effects of longitudinal vortices in a channel flow, *Int. J. Heat Mass Transfer*, vol. 39, pp. 3441–3451, 1996.

Chen, T. Y. and Shu, H. T., Flow structures and heat transfer characteristics in fan flows with and without delta-wing vortex generators, *Exp. Thermal Fluid Sci.*, vol. 28, pp. 273–282, 2004.

Eibeck, P. A. and Eaton, J. K., Heat transfer effects of a longitudinal vortex embedded in a turbulent boundary layer, *Trans. ASME, J. Heat Transfer*, vol. 109, pp. 16–24, 1987.

Gentry, M. C. and Jacobi, A. M., Heat transfer enhancement by delta-wing vortex generators on a flat plate: Vortex interactions with the boundary layer, *Exp. Thermal Fluid Sci.*, vol. 14, pp. 231–242, 1997.

Gentry, M. C. and Jacobi, A. M., Heat transfer enhancement by delta-wing-generated tip vortices in flat-plate and developing channel flows, *ASME J. Heat Transfer*, vol. 124, pp. 1158–1168, 2002.

Kline, S. J. and McClintok, F. A., Describing uncertainties in single-sample experiments, *Mech. Eng.*, vol. 75, pp. 3–8, 1953.

Kwak, K. M., Torii, K., and Nishino, K., Simultaneous heat transfer enhancement and pressure loss reduction for finned-tube bundles with the first or

two transverse rows of built-in winglets, *Exp. Thermal Fluid Sci*., vol. 29, pp. 625–632, 2005.

Lawson, M. J. and Thole, K. A., Heat transfer augmentation along the tube wall of a louvered fin heat exchanger using practical delta winglets, *Int. J. Heat Mass Transfer*, vol. 51, pp. 2346–2360, 2008.

Liou, T. M., Chen, C. C., and Tsai, T. W., Heat transfer and fluid flow in a square duct with 12 different shaped vortex generators, *ASME J. Heat Transfer*, vol. 122, pp. 327–335, 2000a.

Liou, T. M., Chen, C. C., Tzeng, Y. Y., and Tsai, T. W., Non-intrusive measurements of near-wall fluid flow and surface heat transfer in a serpentine passage, *Int. J. Heat Mass Transfer*, vol. 43, pp. 3233–3244, 2000b.

Pesteei, S. M., Subbarao, P. M. V., and Agarwal, R. S., Experimental study of the effect of winglet location on heat transfer enhancement and pressure drop in fin-tube heat exchangers, *Appl. Thermal Eng*., vol. 25, pp. 1684–1696, 2005.

Tigglebeck, S., Mitra, N. K., and Fiebig, M., Comparison of wing type vortex generators for heat transfer enhancement in channel flow, *Trans. ASME, J. Heat Transfer*, vol. 116, pp. 880–885, 1994.

Torii, K., Kwak, K. M., and Nishino, K., Heat transfer enhancement accompanying pressure-loss reduction with winglet-type vortex generators for fin-tube heat exchangers, *Int. J. Heat Mass Transfer*, vol. 45, pp. 3795–3801, 2002.

Vasudevan, R., Eswaran, V. and Biswas, G., Winglet-type vortex generators for plate fin heat exchangers using triangular fins, *Numer. Heat Transfer*, vol. 38, pp. 533–555, 2000.

Wang Q., Chen Q., Wang L., Zeng, M., Huang, Y., and Xiao, Z., Experimental study of heat transfer enhancement in narrow rectangular channel with longitudinal vortex generators, *Nucl. Eng. Design*, vol. 237, pp. 686–693, 2007.

Zhu, J. X., Fiebig, M., and Mitra, N. K., Numerical investigation of turbulent flows and heat transfer in a rib-roughened channel with longitudinal vortex generators, *Int. J. Heat Mass Transfer*, vol. 38, pp. 495–501, 1995.

Journal of Enhanced Heat Transfer, 17(4) 313–329 (2010)
Reprints available directly from the publisher.
Photocopying permitted by license only.

Fluted Helix Channel Heat Transfer along a Vertical Tube

NING MEI,* JIE ZHAO, & YUAN-CHENG XU

College of Engineering, Ocean University of China, Qingdao, 266100, China

The paper investigates (a) thin film formation and (b) falling film heat transfer along a twisted and fluted helix channel on the surface of a vertical tube. Flow and heat transfer of a single-component liquid on the surface on a fluted helix tube are considered and investigated by both numerical simulation and experimental observation. It is found from the numerical study that in certain parameter regimes, the flow and temperature fields can be solved in a closed form. It is seen from experimental results that thin films can uniformly cover the surface of the tube and possess relatively higher heat transfer coefficient.

Key words: vertical fluted helix tube; falling film; flow and heat transfer

*Corresponding author: Mei Ning: nmei@ouc.edu.cn

NOMENCLATURE

a	groove width, m	s, n, z	dimensionless orthogonal curvilinear coordinates
B	body force of the fluid, N	T	local temperature of the fluid, ^{o}C
C_V	specific heat at a constant volume, kJ/kg·^{o}C	T_w	wall temperature of the fluted surface, ^{o}C
g	gravitational acceleration, m^2/s	T_{sat}	saturate temperature of the liquid, ^{o}C
H_0	dimensionless film thickness at the initial point	U^*	characteristic velocity
h_0^*	film thickness at the entrance	U_s	velocity in s direction
H	dimensionless film thickness at any point	V_n	velocity in n direction
H'	film thickness, mm	V^*	velocity of the fluid flow, m/s
h_{fg}	heat of vaporization, kJ/kg	W_z	velocity in z direction
h_1, h_2, h_3	Lame coefficient	We	Weber number
h	heat transfer coefficient, W/m^2·K	X_S^*, Y_S^*, Z_S^*	Cartesian coordinates
J_a	Jacobi number	**Greek symbols**	
K_b^*	surface curvature of the channel	δ	small parameter
K_F	curvature of the free surface	ε	small parameter
K_b	dimensionless K_b^*	θ	dimensionless temperature
K_s	integration of K_b	λ	thermal conductivity of the fluid, W/m^2·K
L	tube length, m		
$\dot{m}$	mass diffusion on the free surface, kg/m^2·s	μ	viscosity of the fluid, Pa·s
Nu	Nusselt number	ρ	density of the fluid, kg/m^3
P^*	local pressure of the fluid flow, Pa	σ	surface tension, N/m
P	dimensionless pressure of the fluid flow	$\vec{\tau}$	shear stress at the liquid–vapor interface, N/m^2
Pr	Prandtl number		
q	heat of evaporation/condensation, kJ/kg	Φ	dissipation function in the process
Q_0	nominal measure	ϕ	helix angle of the fluted channel
r	radius of the tube, m		
Re	Reynolds number	**Subscripts**	
s_a	any point in s domain definition	sat	saturated properties
s', n', z'	orthogonal curvilinear coordinates	w	wall

1. INTRODUCTION

A moving liquid thin film used for heating and cooling purposes provides enhanced heat transfer for many practical applications. However, it is difficult to obtain a uniform falling film in either vertical or horizontal tubes. Because of the surface tension, the contraction of the liquid film free surface leads the formed film to break up into rivulets. Therefore, to build up a uniform thin film, which covers the majority of the tube surface as much as possible, is one of the targets to enhance heat transfer in such a vertical or horizontal tube system.

In the early stages of the falling liquid film research, a great deal of work was performed on smooth cylindrical surfaces (Nusselt, 1982) and on axially fluted surfaces (Gregorig, 1954). Results from experimental and analytical work on the fluted surface (Johnson and Conlisk, 1987; Honda and Fujii, 1984) demonstrate that significant heat transfer enhancements take place when compared with the results for a vertical cylindrical smooth surface. When a liquid flows down on a vertical cylindrical tube, even at low flow rates, it may not completely cover the tube surface. The break up of the film limits the effectiveness of the surface for heat transfer operations. Theoretical

analysis on falling film formation on a fluted tube (Conlisk, 1994) shows a significant increase in heat and mass transfer even at low liquid flow rates, in comparison with at higher flow rates where the convective terms in the momentum equations remain to play an important role. Minimum thickness research involving a liquid film flowing down a vertical tube (Hughes and Bott, 1998) illustrates some rivulet behavior on the vertical tube. At low flow rates, the convective terms in the momentum equations may be neglected (Roberts, 1998). Considering relations between surface tension and gravity, multi-fluted helix channels on vertical tubes can provide sufficient geometric slope to promote fluid flow along both the helix channel and across the boundary of the channel to merge into the fluid of the adjacent channel. With this, it is possible for the surface of the tube to be nearly covered (Mei et al., 1995).

In recent years, a lot of theoretical and experimental researches on falling films have made some progress. The falling film formed on spirally sine fluted tubes is divided into two regions, namely the valley and the crest. The mathematical models of the two regions are depicted and treated separately. The results show a good heat transfer enhancement (Aly and Bedrose, 1995). To study the stability of the liquid falling film, the wall temperature is assumed linearly distributed along the wall and the free surface is taken to be adiabatic (Arghya, 2008). The inertia and convection terms are taken into account and the governing equations are solved numerically (Ouldhadda and Il Idrissi, 2001). The modified Keller box method is also applied to investigate the underlying physical features of film thickness, velocity and temperature distributions for large Reynolds numbers (Shu and Wilks, 2009). Absorbers based on falling film (Nitin, 2005) are demonstrated more compact and efficient. However, insufficient analytical or computational work on the flow and heat transfer properties of liquid film in the helix channel on a vertical tube has been reported in the open literature. In this paper, we investigate the flow and heat transfer on the twisted and fluted surface on the exterior vertical tube and introduce a modified mathematical model based on orthogonal curvilinear coordinate system. The flow velocity, variation of local film thickness, the distribution of temperature, and the heat transfer coefficient are theoretically and experimentally analyzed.

2. DESCRIPTIONS

The geometry to be investigated is depicted in Fig. 1. Fluid enters at the top of the tube through a thin slot and moves helically along the fluted channel under the action of gravity. The flow behavior in a single channel is considered.

The grooved channel surface is described by an explicit functional form using a Cartesian coordinate system X_S^*, Y_S^*, Z_S^* (Mei et al., 1995). In an orthogonal curvilinear coordinate system, as shown in Fig. 2, for each channel, the helix line is as z axis. At each position on the z axis, the normal intersection is on the wall, which is perpendicular to the tangent of the helix line, denoted as the s axis. The normal direction on each point of the s axis is the n axis.

So, the Lame coefficients of the curvilinear coordinate system are

$$h_1 = \sqrt{(\frac{\partial X_s^*}{\partial s'})^2 + (\frac{\partial Y_s^*}{\partial s'})^2 + (\frac{\partial Z_s^*}{\partial s'})^2} = 1 - K_b^* \cdot n' \quad (1)$$

$$h_2 = \sqrt{(\frac{\partial X_s^*}{\partial n'})^2 + (\frac{\partial Y_s^*}{\partial n'})^2 + (\frac{\partial Z_s^*}{\partial n'})^2} = 1 \quad (2)$$

$$h_3 = \sqrt{(\frac{\partial X_s^*}{\partial z'})^2 + (\frac{\partial Y_s^*}{\partial z'})^2 + (\frac{\partial Z_s^*}{\partial z'})^2}$$

$$= [(X_s^* + \frac{n' \cdot f'}{\sqrt{1+f'^2}} + r)^2 \frac{\cos^2\phi}{r^2} \quad (3)$$

$$+ (Y_s^* - \frac{n'}{\sqrt{1+f'^2}})^2 \frac{\cos^2\phi \sin^2\phi}{r^2} + \sin^2\phi]^{\frac{1}{2}}$$

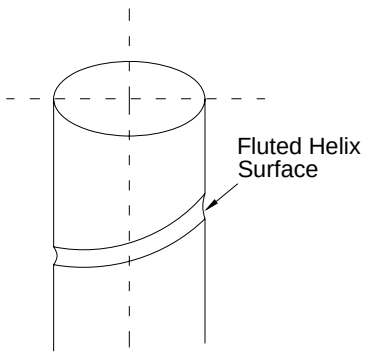

FIGURE 1. Geometry of the fluted helix surface.

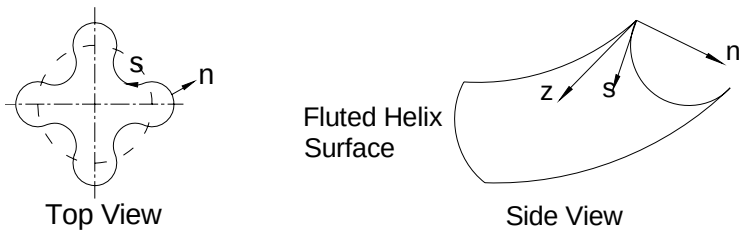

FIGURE 2. Orthogonal curvilinear coordinate system.

Equation (4) displays the function of the grooved channel surface. The Reynolds number, Re, defined by Eq. (5), is assumed to be small enough that inertial effects may be neglected. The characteristic velocity in the film is defined as U^*, as shown in Eq. (6). The surface of the channel can be an alternative curve in geometry and the curvature of its normal intersection to the tangent of the helix line is K_b^*. The dimensionless K_b^* can be expressed as K_b, where K_s is the integration of K_b as shown in Eqs. (7a), (7b), and (7c).

$$Y_S^* = f(X_S^*) \tag{4}$$

$$\mathrm{Re} = \rho \cdot U^* \cdot h_0^* / \mu \tag{5}$$

$$U^* = \rho \cdot g \cdot h_0^{*2} / \mu \tag{6}$$

$$K_b^* = f'' / (\sqrt{1 + f'^2})^3 \tag{7a}$$

$$K_b = a \cdot K_b^* \tag{7b}$$

$$K_s = \int_{s=0}^{S_a} |K_b| \, ds \tag{7c}$$

The velocity between the two coordinate systems is

$$\vec{V}^* = U_s \cdot \vec{e}_s + V_n \cdot \vec{e}_n + W_z \cdot \vec{e}_z \tag{8}$$

where $\vec{e}_s$, $\vec{e}_n$, $\vec{e}_z$ are unit vectors in s, n, z directions.

3. THEORETICAL ANALYSIS TO FLUID FLOW AND HEAT TRANSFER OF FALLING FILM IN THE CHANNEL ON THE VERTICAL FLUTED HELIX TUBE SURFACE

Gravity-driven laminar film flows are considered in a fluted helix channel. In accordance with the basic knowledge of fluid mechanics, the governing equations for this case in a rectangular Cartesian coordinate system are

Continuity equation:

$$\nabla \cdot \vec{V}^* = 0 \tag{9}$$

Momentum equation:

$$\rho(\vec{V}^* \cdot \nabla)\vec{V}^* = -\nabla \vec{P}^* + \rho \vec{B} + \mu \nabla^2 \vec{V}^* \tag{10}$$

Energy equation:

$$\lambda \nabla^2 T + \Phi = \rho \cdot C_V \vec{V}^* \cdot (\nabla T) \tag{11}$$

The basic assumptions for this case can be stated as

(1) The fluid flow is a steady flow with a low Reynolds number. The convective terms in thee Navier–Stokes equations are neglected; hence dissipation in the energy equation can also be neglected.

(2) The liquid density ρ, the gravitational acceleration g, and fluid viscosity μ are treated as constant.

(3) Mass transfer only takes place on the free surface and it is controlled by the local heat transfer behavior inwards of the fluid.

In the basis of the above assumptions, the governing equations of a liquid film transformed in the orthogonal curvilinear coordinate system can be given as follows

Continuity equation:

$$\frac{\partial(h_3 U_s)}{\partial s'} + \frac{\partial(h_1 h_3 V_n)}{\partial n'} + h_1 \frac{\partial W_z}{\partial z'} = 0 \tag{12}$$

Momentum equations:

$$\mu[\nabla^2 U_s + \frac{2}{h_1^2}\frac{\partial h_1}{\partial n'}\frac{\partial V_n}{\partial s'} - \frac{2}{h_1 h_2^2}\frac{\partial h_3}{\partial s'}\frac{\partial W_z}{\partial z'}$$

$$+\frac{U_s}{h_1}\frac{\partial}{\partial s'}(\frac{1}{h_1 h_3}\frac{\partial h_3}{\partial s'}) + \frac{U_s}{h_3}\frac{\partial}{\partial n'}(\frac{h_3}{h_1}\frac{\partial h_1}{\partial n'}) \quad (13)$$

$$+\frac{V_n}{h_1}\frac{\partial}{\partial s'}(\frac{1}{h_1 h_3}\frac{\partial (h_1 h_3)}{\partial n'})] = \frac{1}{h_1}\frac{\partial P}{\partial s'} - \rho g \cos\phi \cos K_s,$$

$$\mu[\nabla^2 V_n - \frac{2}{h_3^2}\frac{\partial h_3}{\partial n'}\frac{\partial W_z}{\partial z'} + \frac{2}{h_1^2}\frac{\partial h_1}{\partial n'}\frac{\partial U_s}{\partial s'}$$

$$-\frac{U_s}{h_1}[\frac{1}{h_3}\frac{\partial}{\partial s'}(\frac{h_3}{h_1}\frac{\partial h_1}{\partial n'}) - h_1\frac{\partial}{\partial n'}(\frac{1}{h_1 h_3}\frac{\partial h_3}{\partial s'})] \quad (14)$$

$$+V_n\frac{\partial}{\partial n'}(\frac{1}{h_1 h_3}\frac{\partial (h_1 h_3)}{\partial n'})] = \frac{\partial P}{\partial n'} + \rho g \cos\phi \sin K_s,$$

$$\mu[\nabla^2 W_z + \frac{2}{h_1 h_3^2}\frac{\partial h_3}{\partial s'}\frac{\partial U_s}{\partial z'} + \frac{2}{h_3^2}\frac{\partial h_3}{\partial n'}\frac{\partial V_n}{\partial z'} \quad (15)$$

$$+\frac{W_z}{h_1}\frac{\partial}{\partial s'}(\frac{1}{h_1 h_3}\frac{\partial h_3}{\partial s'}) + \frac{W_z}{h_1}\frac{\partial}{\partial n'}(\frac{h_1}{h_3}\frac{\partial h_3}{\partial n'})]$$
$$= \frac{1}{h_3}\frac{\partial P}{\partial z'} - \rho g \sin\phi$$

Energy equation:

$$\nabla^2 T = \frac{\rho C_v}{\lambda}(\frac{\partial T}{\partial t} + \frac{U_s}{h_1}\frac{\partial T}{\partial s'} + V_n\frac{\partial T}{\partial n'} + \frac{W_z}{h_3}\frac{\partial T}{\partial z'}) \quad (16)$$

In order to analyze the basic flow structure, the parameters are made dimensionless. Therefore the orthogonal curvilinear coordinate system can be made nondimensional as

$$s = \frac{s'}{a}, \quad n = \frac{n'}{h_0^*}, \quad z = \frac{z'}{L},$$

$$\delta = \frac{h_0^*}{a}, \quad \varepsilon = \frac{h_0^*}{L}, \quad \lambda = \frac{a}{L},$$

$$U^* = \frac{\rho \cdot g \cdot h_0^{*2}}{\mu}, \quad P = \frac{P^*}{\frac{\sigma}{a}}, \quad \theta = \frac{T - T_s}{T_w - T_s},$$

$$U = \frac{U_s}{U^*}, \quad V = \frac{V_n}{U^* \cdot \delta}, \quad W = \frac{W_z}{U^*}$$

The dimensionless velocity component is expressed as

$$\vec{V} = U \cdot \vec{e}_s + V \cdot \vec{e}_n + W \cdot \vec{e}_z \quad (17)$$

U, represents the velocity along the section line of the channel, V is the velocity in the direction of the film thickness, and W is the velocity in the tangent direction of the helix line, respectively. We neglect the terms with δ and ε (i.e., neglect higher order terms). The dimensionless governing equations in the curvilinear coordinate system reduce to Eqs. (18)–(22)

Continuity equation:

$$\frac{1}{h_1 h_3}\frac{\partial h_3 U}{\partial s} + \frac{\partial V}{\partial n} + \frac{\varepsilon}{\delta h_3}\frac{\partial W}{\partial z} = 0 \quad (18)$$

Momentum equations:

$$\frac{\partial^2 U}{\partial n^2} = \frac{W_e^{-1}}{h_1}\frac{\partial P}{\partial s} - \cos\phi \cos K_s \quad (19)$$

$$\delta\frac{\partial^2 V}{\partial n^2} + \delta \cdot U\frac{\partial}{\partial n}(\frac{1}{h_1 h_3}\frac{\partial h_3}{\partial s}) \quad (20)$$

$$= \frac{W_e^{-1}}{\delta}\frac{\partial P}{\partial n} + \cos\phi \sin K_s$$

$$\frac{\partial^2 W}{\partial n^2} = \frac{\varepsilon \cdot W_e^{-1}}{\delta \cdot h_3}\frac{\partial P}{\partial z} - \sin\phi \quad (21)$$

Energy equation:

$$\frac{\partial^2 \theta}{\partial n^2} = \delta R_e P_r(\frac{U}{h_1}\frac{\partial \theta}{\partial s} + V\frac{\partial \theta}{\partial n} + \frac{\varepsilon W}{\delta h_3}\frac{\partial \theta}{\partial z}) \quad (22)$$

Based on the geometry of the selected fluted helix tube, the domain definitions for the above governing equations are specified as

$$s \in [-1,1]\ n \in [0, H],\ z \in [0,1.414]$$

A no-slip boundary condition can be applied in this case, then the jump in the normal stress should be balanced by surface tension, thus

$$\vec{\tau} \cdot \vec{N} = -\sigma K_F \quad (23)$$

The leading order terms for Eq. (23) are

$$P \approx \frac{K_b}{h_1} + \frac{1}{h_3^2}[(\frac{a}{r}\frac{f'}{\sqrt{1+f'^2}}(\frac{a}{r}X_S + 1) \cdot \cos^2\phi) \quad (24)$$

$$-\frac{Y_s}{\sqrt{1+f'^2}}\frac{a^2\cos^2\phi\sin^2\phi}{r^2}]$$

where $\delta, \varepsilon << 1$ and the momentum equation in n direction gives the usual leading-order result. The governing equations are solved in the conjunction with the following boundary conditions:

$$\frac{\partial P}{\partial n} \approx 0, \quad P = P(s, z), \quad n = 0,$$

$$U = 0, \quad W = 0, \quad n = H(s, z),$$

$$\frac{\partial U}{\partial n} \approx 0, \quad \frac{\partial W}{\partial n} \approx 0$$

The velocity distribution in the thin film is obtained finally as

$$U = (W_e^{-1}\frac{\partial P}{\partial s} - \cos\phi\cos K_s)(\frac{1}{2}n^2 - nH) \tag{25}$$

$$V = -\frac{1}{h_1}(We^{-1}\frac{\partial^2 P}{\partial s^2} + \cos\phi\sin K_s \cdot K_s')$$

$$\times(\frac{1}{6}n^3 - \frac{1}{2}n^2 H) + \frac{1}{h_1}(We^{-1}\frac{\partial P}{\partial s} - \cos\phi\cos K_s) \tag{26}$$

$$\times\frac{n^2}{2}\frac{\partial H}{\partial s} - \frac{\varepsilon}{h_3\delta}\sin\phi\frac{n^2}{2}\frac{\partial H}{\partial z}$$

$$W = (\frac{\varepsilon W_e^{-1}}{\delta h_3}\frac{\partial P}{\partial z} - \sin\phi)(\frac{1}{2}n^2 - nH) \tag{27}$$

The mass flow in the normal direction of the free surface is supposed to be that vaporized or condensed on the free surface due to heat conduction in the normal direction of the free surface. It can be expressed as

$$\rho\vec{V}\cdot\vec{N} = -\frac{\lambda\nabla T\cdot\vec{N}}{q} \tag{28}$$

For evaporation/condensation on the free surface for a steady state, we have

$$\frac{\partial\theta}{\partial n} = \frac{\delta\,\mathrm{Re}\,\mathrm{Pr}\,\dot{m}}{J_a} \tag{29}$$

When evaporation/condensation on the free surface occurs due to heat conduction, the heat transferred is defined as $Q = Q_0\hat{Q}(s, z)$. Let $H = (3Q_0W_e)^{\frac{1}{4}}\hat{H}$, where $\hat{H}$ is a nominal measure. On account of $\varepsilon/\delta = a/L$, the flow driven by surface tension of the fluid should be coupled with flows due to other forces. Thus we have $\varepsilon/\delta = \mathrm{We}^{-1}$ or $L = \rho g a^3/\sigma = \mathrm{We}\cdot a$. When the tube radius r is much longer than the span of the channel, the Lame coefficient h_3 is nearly equal to $\sin\phi$, so that the governing equations can be solved. Introducing Eqs. (22), (29) and the velocity distribution in the thin film into Eq. (28) we can rewrite Eq. (28) as

$$\frac{\partial\hat{H}^3}{\partial z} + \frac{\partial(A_1\hat{H}^3)}{\partial s} = \frac{\hat{Q}}{\hat{H}} \tag{30}$$

where

$$A_1 = We\cos K_s\cos\phi - K_b'$$

$$Q = \frac{\lambda\Delta T}{\rho h_{fg} h_0^* \delta U^*}$$

If the initial condition is at the starting point of the thin film then

$$s = s_0, \quad z = 0, \quad H_0 = H(s_0, 0)$$

The quasi-linear partial differential equation in first order described by Eq. (30) above is a Cauchy case. When $A_1 \neq 0$, the characteristic line method is used to obtain the solution

$$H = [\frac{(A_1|_{s_0})^{\frac{4}{3}}}{(A_1|_{s_a})^{\frac{4}{3}}}H^4(s_0) + 4QWe\frac{\int_{s=s_0}^{s_a}(A_1|_s)^{\frac{1}{3}}ds}{(A_1|_{s_a})^{\frac{4}{3}}}]^{\frac{1}{4}} \tag{31}$$

When $A_1 = 0$, Eq. (30) becomes a linear partial differential equation in first order for $\hat{H}^4$. The solution is

$$H = [e^{-\frac{4}{3}A_1'z}H_0^4 + \frac{3}{4}\frac{1}{A_1}e^{-\frac{4}{3}A_1'z}$$

$$\times(4QWe\cdot e^{\frac{4}{3}A_1'z} - 4QWe)]^{\frac{1}{4}} \tag{32}$$

As the fluid moves helically along the fluted channel, heat is simultaneously transferred between the solid surface and the thin film. On account of the complex tube geometries, s will be assumed small in comparison to z and the temperature gradient in the normal direction plays a key role in heat transfer. Neglecting the liquid temperature variation along the s direction reduces the energy equation (22) to

$$\frac{\partial^2\theta}{\partial n^2} = \delta \mathrm{R}_e \mathrm{P}_r (V \frac{\partial\theta}{\partial n} + \frac{\varepsilon W}{\delta h_3}\frac{\partial\theta}{\partial z}) \tag{33}$$

The temperature boundary conditions are given by

$$n = 0, \quad \theta_w = 1, \quad n = H, \quad \theta_s = 0$$

A finite difference method is used to solve the nonlinear partial differential equations. The first-order differential terms in the differential equation using first-order accurate differences while second-order accurate differences are used in second-order differential terms. Divide the dimensionless z along a twisted channel and so do the thickness of film H into differential segments of an incremental length Δz and Δn respectively.

$$n_i = i*\Delta n, \quad \Delta n = H/10; \quad z = j*\Delta z,$$

$$\Delta z = 0.0707 \ (i = 0,1,2...10; \quad j = 0,1,2,...20).$$

A central difference approximation to $\frac{\partial^2\theta}{\partial n^2}$ is adopted, while forward difference approximations are applied to $\frac{\partial\theta}{\partial n}$ and $\frac{\partial\theta}{\partial z}$. The energy equation (33) is approximated as

$$\frac{\theta_{i-1,j} - 2\theta_{i,j} + \theta_{i+1,j}}{(\Delta n)^2} \tag{34}$$

$$= \delta R_e P_r (V_{i,j} \frac{\theta_{i+1,j} - \theta_{i,j}}{\Delta n} + \frac{\varepsilon}{\delta}\frac{W_{i,j}}{h_3}\frac{\theta_{i,j+1} - \theta_{i,j}}{\Delta z})$$

The discrete boundary conditions are expressed as

$$n_{0,j} = 0, \quad \theta_{0,j} = 1; \quad n_{10,j} = \mathrm{H}, \quad \theta_{10,j} = 0.$$

The further form of Eq. (26) is

$$\theta_{i,j+1} = A\theta_{i-1,j} + B\theta_{i,j} + C\theta_{i+1,j} \tag{35}$$

where

$$A = \frac{\delta h_3 \Delta z}{\varepsilon W_{i,j} \Delta n^2}$$

$$B = \frac{\delta \,\mathrm{Re}\,\mathrm{Pr} V_{i,j}}{\Delta n} \cdot \frac{\delta h_3 \Delta z}{\varepsilon W_{i,j}} - \frac{2\delta h_3 \Delta z}{\varepsilon W_{i,j} \Delta n^2} + 1$$

$$C = \frac{\delta h_3 \Delta z}{\varepsilon W_{i,j} \Delta n^2} - \frac{\delta h_3 \Delta z}{\varepsilon W_{i,j}} \cdot \frac{\delta \,\mathrm{Re}\,\mathrm{Pr} V_{i,j}}{\Delta n}$$

When $A > 0$, $B > 0$, $C > 0$, Eq. (35) satisfies the stability condition. The temperature field can be numerically obtained by combining Eq. (35) with the temperature boundary conditions, the velocity distribution, and thickness of the thin film.

The heat flux across the surface of the twisted tube and the bottom of the thin film q_z is given by the Fourier law

$$q_z = -\lambda(T_{sat} - T_w) \left.\frac{\partial\theta}{\partial n}\right|_{w,z} \tag{36}$$

Energy balance at the interface between the liquid and the wall produces the interfacial boundary condition

$$h_z(T_w - T_f) = -\lambda(T_{sat} - T_w) \left.\frac{\partial\theta}{\partial n}\right|_{w,z} \tag{37}$$

The heat transfer coefficient of the twisted tube surface can be expressed as

$$h_z(T_w - T_f) = -\lambda(T_{sat} - T_w) \left.\frac{\partial\theta}{\partial n}\right|_{w,z} \tag{38}$$

An analytical solution of the velocity distribution, liquid film thickness, numerical solution of temperature distribution, and heat transfer properties of a falling liquid film are obtained in the case of evaporation.

4. EXPERIMENT DESCRIPTIONS

Figure 3 shows a schematic diagram of the test bed. It consists of a vertical twisted and fluted tube, power supply, falling fluid (water) film circulation, stereomicroscope, and a data processing system. The parameters of the test tube with a sine cross-section helix flutes are given in Table 1. Liquid flows in from the top of the tube through a thin slot and moves helically along the fluted channels. Due to gravity and surface tension, a continuous and uniform thin falling film is formed. The top edge of the groove in the curvilinear coordinate system is given by $s = -1$, while the bottom edge is given by $s = 1$. Six pre-selected positions along

TABLE 1: Parameters of the Fluted Helix Tubes

Parameters	n^*	R	L	a	ϕ
Value	3	0.0115	0.167	0.007	45°

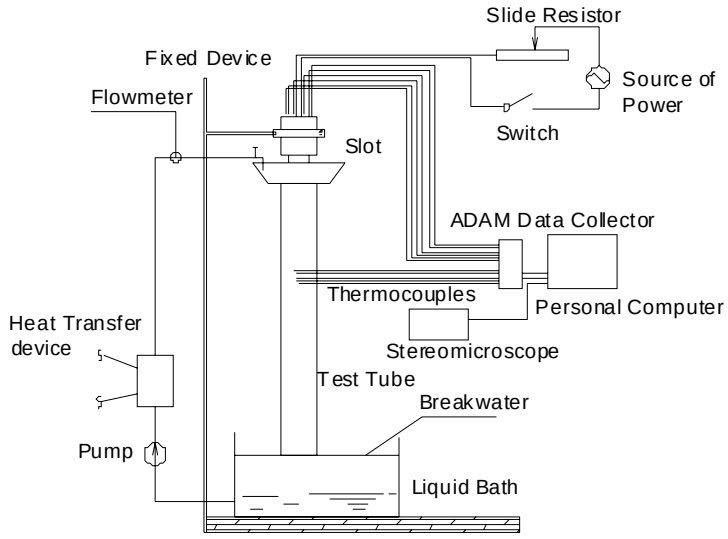

FIGURE 3. Sketch of equipment for falling film experiment.

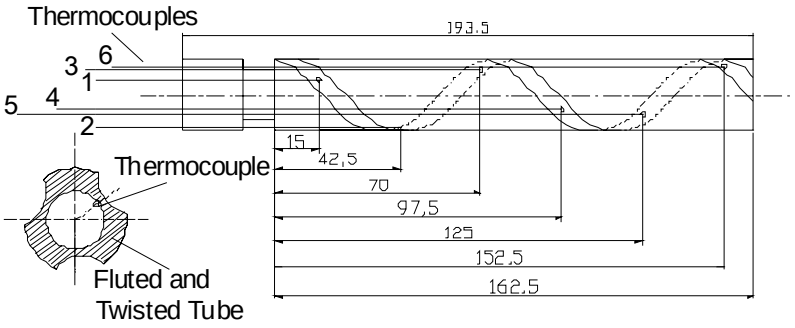

FIGURE 4. Sketch of thermocouples embedded scheme.

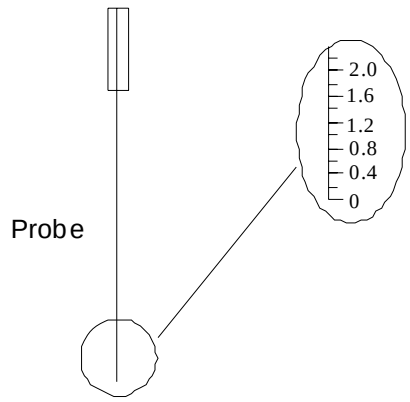

FIGURE 5. The probe marked with microscale.

the helix channel are measured to obtain the film thickness, the tube wall temperature and fluid temperature in the liquid film, as shown in Fig. 4.

In order to measure the falling film profile on the surface of the tube, a probe marked with micro-scale is applied, as shown in Fig. 5. As the liquid film flows down with a low flow rate, and the probe is relatively thin, thus the liquid slight climb on the probe can be neglected. When the probe is inserted into the liquid film, the film thickness can be detected by means of a stereomicroscope. In the case of a larger flow rate, the observing value in the direction of countercurrent can be adopted to eliminate the impact of the liquid climb on the film thickness measurement. In the helix chan-

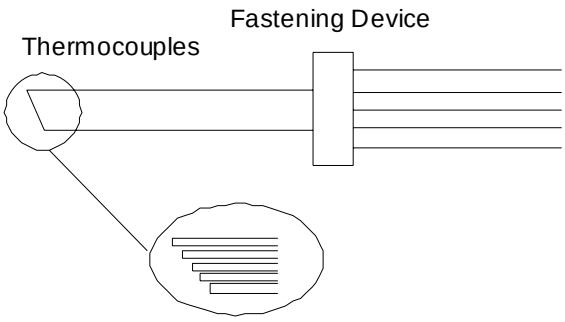

FIGURE 6. The sketch of attached thermocouples.

nel, the measurement positions 1 and 6 of the six preselected positions are affected by some factors, because the film thickness measurements at the two points are lack in accuracy. Thus, from points 2 to 5, the thickness of the liquid film along the s direction is explored.

In order to measure the temperature distribution in the direction of a film thickness at some position, the tips of five thermocouples are made in an array with different tip length, as shown in Fig. 6. When the thermocouple array is vertically inserted into the fluid film, different terminations of the thermocouples have different distances from the tube wall due to the special arrangement of thermocouples, thus the temperature distribution in the vicinity of a selected point can be measured along the direction of the film thickness with the help of the ADAM data collector, then the average fluid temperature at each point can be obtained. To investigate the tube wall temperature, six K-type thermocouples are embedded along the length of the vertical tube z at the six pre-selected points, as shown in Fig. 4. A series of repeating experiments are carried on.

5. RESULTS AND DISCUSSIONS

The numerical solution to velocity distribution in the s direction denoted by U is shown in Fig. 7. The velocity on the wall meets the no-slip boundary condition. The velocity in the liquid film increases along the n direction. The velocity U becomes negative in the regions from $s_1 = -1.0$ to $s_2 = -0.2$ and from $s_3 = 0.8$ to $s_4 = 1.0$. This implies that a film between s_1 and s_2 congregates in the trough of the groove, as shown in Fig. 8. Whereas the film between s_3 and s_4 tends to cross the boundary of the channel and merge into the fluid flow in the adjacent channel. Additionally, the fluid tends to move to the crest region and accumulates in the trough region. The velocity U is mainly influenced by the surface geometry of the fluted tube, which has a crucial influence upon the surface tension of the liquid.

Figures 9 and 10 show the variations of V and W along the s axis. There is an intermittent point at $s_3 = 0.8$ which occurs when $A_1 = 0$. Thus, the numerical so-

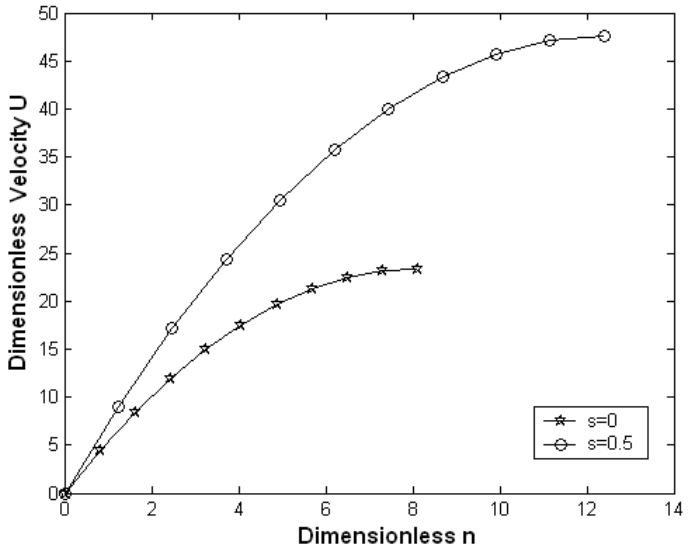

FIGURE 7. Variation of the dimensionless velocity U with n.

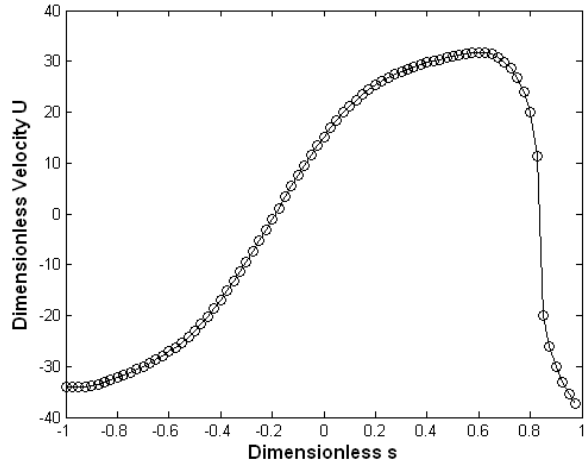

FIGURE 8. Variation of the dimensionless mean velocity *U* with *s*.

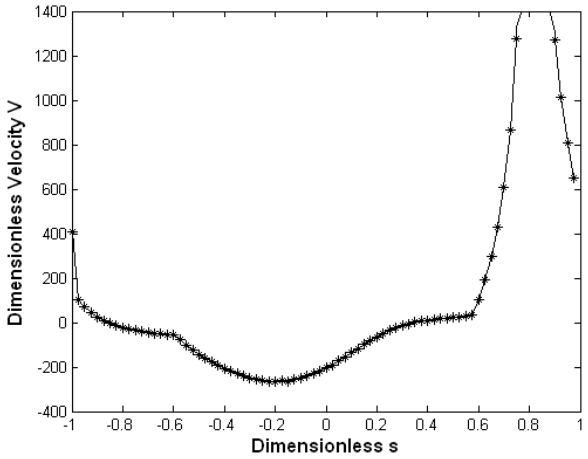

FIGURE 9. Variation of the dimensionless mean velocity *V* with *s*.

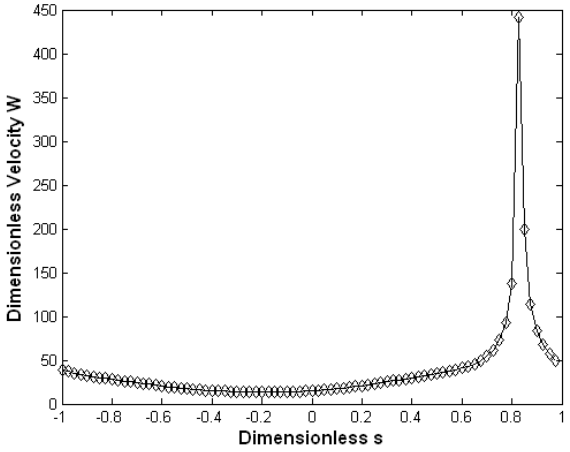

FIGURE 10. Variation of the dimensionless mean velocity *W* with *s*.

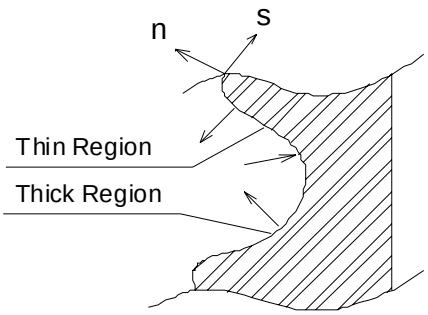

FIGURE 11. Schematic diagram of the direction of the dimensionless velocity *V*.

lution to the velocity around this point is unreasonably high, as shown in Figs. 9 and 10. This indicates that the liquid accumulates in this area. A schematic diagram of the flow is shown in Fig. 11. It can be deduced by the discussion above that the surface geometry of the fluted tube, surface-tension effects, and gravity produce to the described complex velocity distribution in the channel.

The thickness of the film formed on the spiral tube is shown in Fig. 12. The curve of the bottom-up in the figure shows the entire development of the film that changed from the formation to the steady state. The film thickness increases slowly at the beginning and then remains constant as the fluid falls. The numerical solution shows that the film thickness H approaches a uniform value. The maximum value of the film thickness appears when the velocity reaches its maximum. This implies that the fluid accumulates in the trough.

Figure 13 presents the typical steady state. When the film develops to a stable film in the channel, two regions in the film thickness form, as shown in Fig. 13. In the thin region, fluid accumulates gradually to form a thin film. It is deduced that the surface tension plays a key role on this thin film formation. It is the surface tension to avoid fluid rivulet in this region. In the thicker region, the fluid converges around the trough.

Figure 14 displays experimental film profile data. These data indicate that variations of the film thickness nearly replicate the results from numerical simulation. No rivulet around the crest and a large amount of liquid accumulated around the trough were found from both experimental observation and numerical simulation.

The numerical temperature solution is shown in Fig. 15. The results indicate that the temperature decreases from the tube wall to the free surface of the liquid film. Additionally there is little change in the temperature distribution along the channel. Laminar flow conditions cause this lack of temperature change along the channel. That is, the boundary layer develops slowly as the fluid moves along the twisted channel. This is evidenced from the numerical solution of the film temperature that remains nearly constant in the region of , where the film thickness is about 50% of its total value.

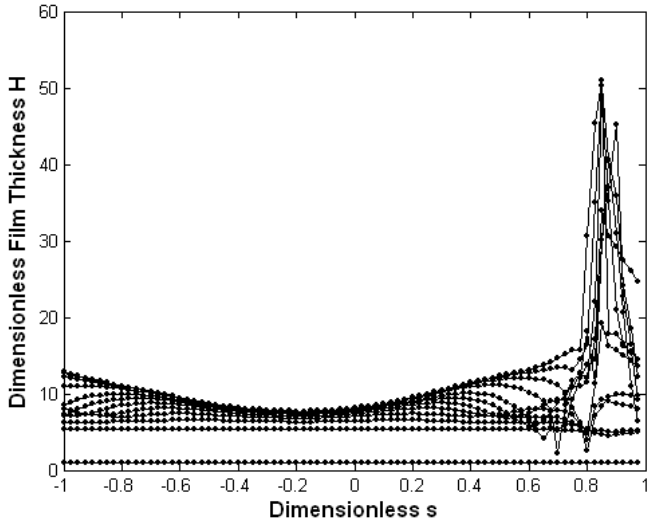

FIGURE 12. Variation of the dimensionless film thickness with *z* in *s* direction.

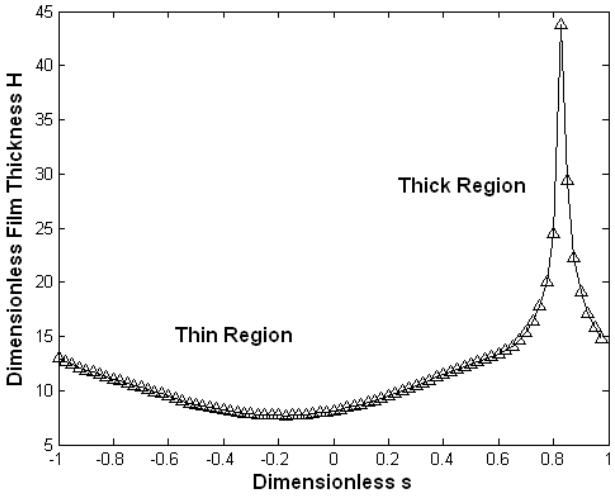

FIGURE 13. Distribution of the dimensionless film thickness *H* in *s* direction.

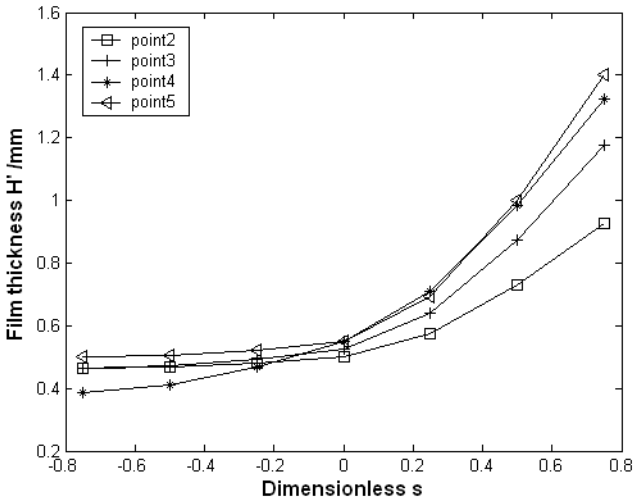

FIGURE 14. Experimental film profile in *s* direction.

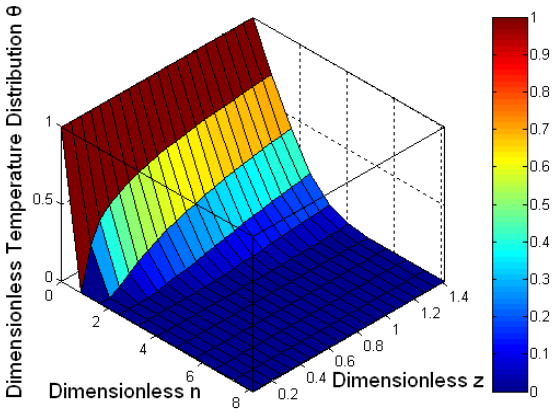

FIGURE 15. Variation of the dimensionless temperature with *n* and *z*.

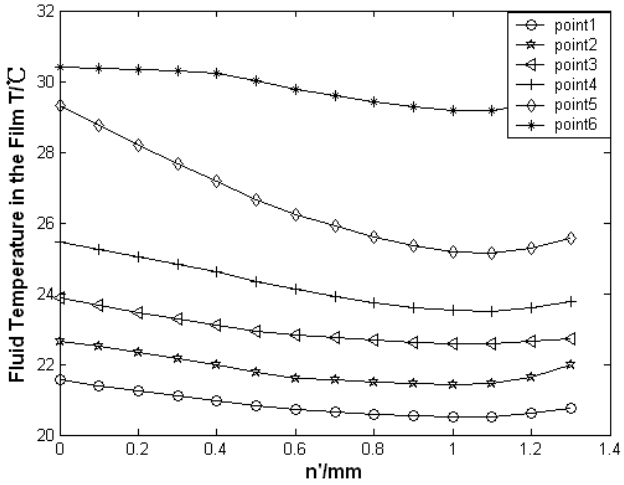

FIGURE 16. Variation of the fluid temperature with n'.

Figure 16 illustrates experimental results for the temperature distribution in the liquid film. The film temperature increases as the liquid flows down. A dimensionless temperature distribution is obtained by using the highest temperature distribution as the datum in Fig. 16. The corresponding dimensionless temperature distribution is shown in Fig. 17. Comparing Fig. 17 with the numerical solution of the dimensionless temperature, as shown in Fig. 15, reveals that nearly the same variation occurs; however the physical thermal boundary thickness is thinner.

Figures 18 and 19 show the experimental results of the tube wall temperature and the average film temperature. The wall temperature is initially low at the beginning and increases in the z direction. This occurs since the fluid temperature enters the spiral grooves at a low temperature and has a strong cooling capacity when a constant heating rate is maintained. The fluid temperature increases gradually as the liquid falls down, as described in Fig. 19. The wall temperature increases gradually until it reaches its maximum value in the region of $z = 0.8 \sim 1.0$ and begins to decrease. This occurs since the electrical heating wire is shorter than the test tube length. The end part of the tube cannot be directly heated and thermal radiation at the end cross section removes heat from the system. The

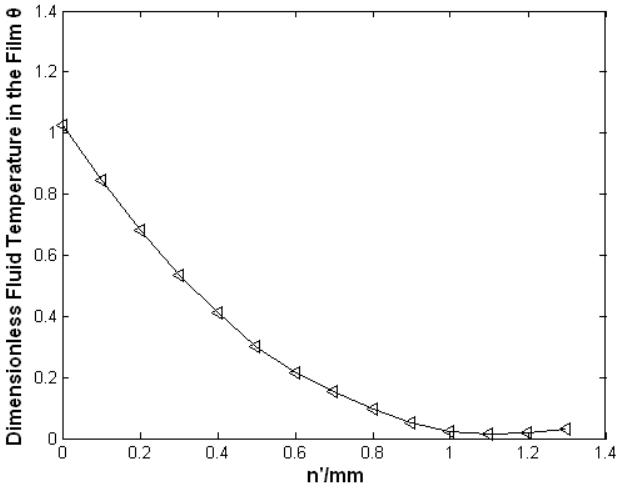

FIGURE 17. Variation of the dimensionless fluid temperature with n'.

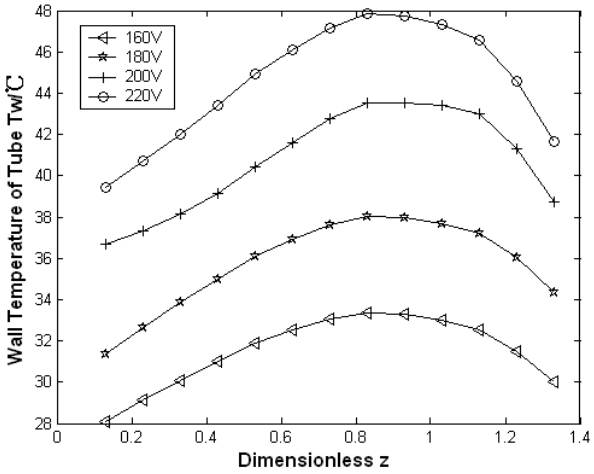

FIGURE 18. Distribution of the tube temperature in *z* direction.

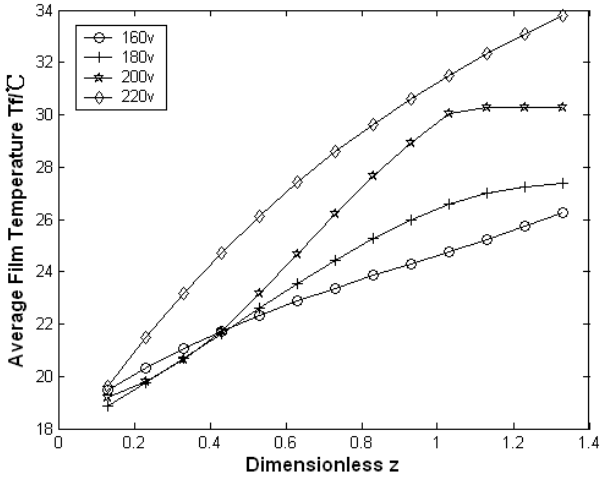

FIGURE 19. Distribution of the cross-section average film temperature in *z* direction.

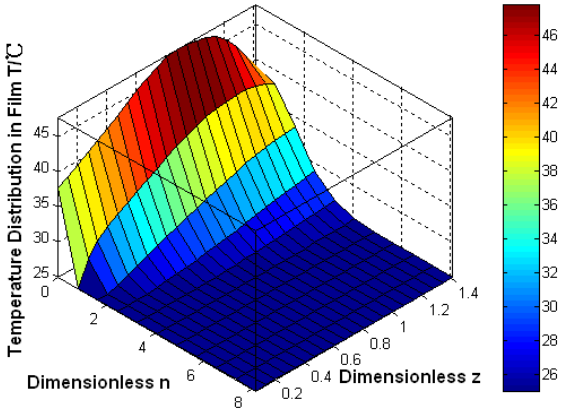

FIGURE 20. Variation of temperature in the falling film with *n* and *z*.

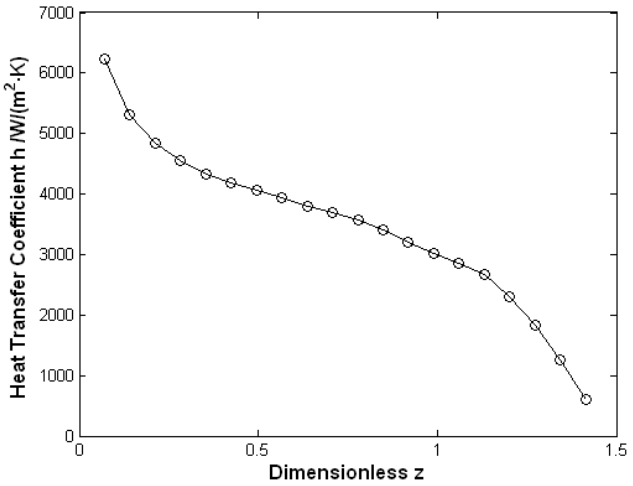

FIGURE 21. Variation of the heat transfer coefficient *h* with *z*.

higher the input heating voltage is, the higher the wall and film temperature level, as shown in Fig. 18.

The wall temperature distribution obtained by the experiment is then used as the boundary condition to the energy equation for the numerical model (other than the initial constant wall temperature used in the numerical simulation). A similar film temperature field is obtained, as shown in Fig. 20, when compared to Fig. 15. This suggests that the wall temperature has little influence on the characteristic film temperature distribution.

The numerical solution for the heat transfer coefficient is shown in Fig. 21. When the cold fluid enters into the twisted channel in which the temperature is relatively high, significant amounts of heat is transferred from the wall to the film. Thus the film temperature of fluid increases gradually along the surface of the fluted helix tube while the heat transfer coefficient decreases.

In this paper, all of the studies above are based on a three-fluted helix tube. To investigate the effect of the surface structure of the fluted helix tube on the heat transfer coefficient, a series of repeated tests are carried on single-fluted, two-fluted, and three-fluted helix tubes. The ranges of average heat transfer coefficients are shown in Fig. 22. The results indicate that

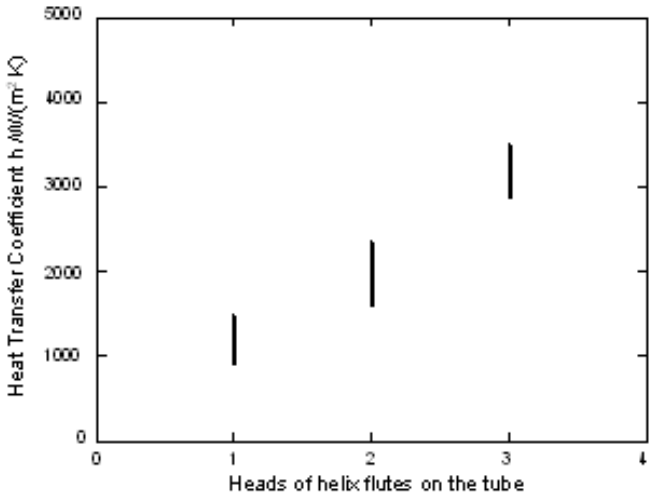

FIGURE 22. Effect of heads of helix flutes on the heat transfer coefficient.

the heat transfer coefficient of a multi-fluted helix tube is significantly higher than the single one in the same experimental condition because the film distribution is more uniform in the multi-fluted tube when compared with the single fluted tube (Wu et al., 2005). And the average heat transfer coefficient range of a three-fluted tube compares favorably with the numerical solution, as shown in Fig. 21.

6. CONCLUSIONS

This paper describes the film formation and heat transfer along a channel surface of a fluted helix tube. The proposed hierarchal description is based on mathematical, physical, and experimental observations. The numerical models that describe the behaviors of the liquid film formation and heat transfer in the fluted and twisted helix channel of a vertical tube in the orthogonal curvilinear coordinate system is established. An analytical solution of the velocity distribution, liquid film thickness, and numerical solution of temperature distribution all suggest that the velocity distribution changes only slightly along the helix channel but relative larger in the film thickness and channel cross section. The liquid thin film can cover the entire surface of the helix channel due to the results of interaction between gravity and surface tension. The film thickness distribution remains nearly constant along the helix channel but accumulates in the trough. The film temperature increases along the helix channel at condition of a constant heat flux supplied, but drops at the end of the heating tube. The heat transfer coefficient is high in the region where liquid enters into the channel and then decreases as the fluid continues to flow in the downward path.

An experimental test bed is developed to verify the results of the numerical solution. The film thickness and distribution of temperature are measured by microscale probes and thermocouples. The experimental results show that the film distribution characteristics nearly replicate the numerical solution for the film temperature distribution. The thermal boundary thickness is thinner than that of thee predicted numerical solution. The experimental and numerical results predicted that average heat transfer coefficients produce similar orders-of-magnitude results.

ACKNOWLEDGMENTS

This work is sponsored by the National Natural Science Foundation of China (project No. 50676086) and the Ministry of Science and Technology of China (project No. 2008AA05Z208).

REFERENCES

Aly, N. H. and Bedrose, S. D., Enhanced film condensation of steam on spirally fluted tubes, *Desalination*, vol. 101, pp. 295–301, 1995.

Arghya, S., Stability of liquid film falling down a vertical non-uniformly heated wall, *Physica D*, vol. 237, pp. 2587–2598, 2008.

Conlisk, A. T., Structure of falling film heat and mass transfer on a fluted tube, *AICHE J.*, vol. 40, no. 5, pp. 145–148, 1994.

Gregorig, R., Hautkondensation a feigewellten Oberflachen bei beruksichtigung der Oberflachenspannungen, *Z. ang. Math. Physik*, vol. 5, pp. 36–39, 1954.

Honda, H. and Fujii, T., Semi-empirical equation for condensation heat transfer on vertical fluted tube, *Winter Annual Meet. ASME*, New Orleans, LA, pp. 9–14, 1984.

Hughes, D. T. and Bott, T. R., Minimum thickness of a liquid film flowing down a vertical tube, *Int. J. Heat Mass Transfer*, vol. 41, no. 2, pp. 253–260, 1998.

Johnson, R. E. and Conlisk, A. T., Laminar-film condensation/evaporation on a vertically fluted surface, *J. Fluid Mech.*, vol. 184, pp. 245–266, 1987.

Mei, N., Jin, H. P., and Li, H. J., Heat transfer of moving liquid film on a hot wall, *Numer. Meth. Thermal Probl.*, vol. 9, pp. 1113–1114, 1995.

Nitin, G., A compact falling film absorber, *J. Heat Transfer*, vol. 127, pp. 957–965, 2005.

Nusselt, W., The condition of stream on cooling surface, *Chem. Eng. Fund.*, vol. 1, no. 2, pp. 6–19, 1982.

Ouldhadda, D. and Il Idrissi, A., Laminar flow and heat transfer of non-newtonian falling liquid film

on a horizontal tube with variable surface heat flux, *Int. Comm. Heat Mass Transfer*, vol. 28, no. 8, pp. 1125–1135, 2001.

Roberts, A. J., An accurate model of thin 2D fluid flows with inertia on curved surface, in Free Surface Flow with Viscosity, *Computational Mechanics Publication*, UK, pp. 69–88, 1998.

Shu, J. J. and Wilks, G., Heat transfer in the flow of a cold, two-dimensional draining sheet over a hot, horizontal cylinder, *Eur. J. Mech. B/Fluids*, vol. 28, pp. 185–190, 2009.

Wu, Y. J., Mei, N., and Liang, Z. D., Flowing state of falling liquid film outside a multi-fluted helix tube when blending, *J. Eng. Thermophys.*, vol. 26, no. 2, pp. 280–282, 2005.

Journal of Enhanced Heat Transfer, 17(4) 331–341 (2010)
Reprints available directly from the publisher.
Photocopying permitted by license only.

Experimental Investigation of the Applied Performance of Several Typical Enhanced Tubes

ZHI-MING XU* **& ZHONG-BIN ZHANG**

Northeast China Dianli University, Jilin, China, 132012

The main purpose of this paper is to investigate the applied performance of the four typical enhanced tubes and parameters such as flow pressure drop, the friction factor, enhanced heat transfer, and anti-fouling performance. The results show that each enhanced tube has certain features. The arc line tube has the greatest friction factor, whereas the corrugated tube has the highest average energy efficiency and the best anti-fouling performance, etc. In addition, these enhanced tubes have better anti-fouling performance in comparison with the corresponding plain tube.

Key words: enhanced tubes; friction factor; enhanced heat transfer; anti-fouling performance; induction period

*Corresponding author: X. Zhi-Ming: xuzm@mail.nedu.edu.cn

NOMENCLATURE

A	surface area used in heat transfer, m^2	ε	relative error, %
c_p	specific heat, J/kg·K	η	exergy coefficients
d	inner diameter of tube, m	λ	coefficient of thermal conductivity, W/m·K
E	exergy of heat absorption, W	ν	movement viscosity, m^2/s
E_{XQ}	exergy of heat, W	ρ	density, kg/m^3
f	friction factor	Φ	heat flux, W
g	gravitational acceleration, m/s^2	**Subscripts**	
h	convective heat transfer coefficient, $W/m^2 \cdot K$	0	clean conditions
l	length of tube, m	1, 2, 3	serial number
Nu	Nusselt number	a	arc line tube
Q	heat quantity, J	cf	convergent-divergent tubes I
q_v	fluid volumetric capacity, m^3/s	cs	convergent-divergent tubes II
R	fouling thermal resistance, $m^2 \cdot K/W$	c	corrugated tube
Re	Reynolds number	f	fouling; fluid
T	constant heat source temperature, K	fi	fluid inlet
T_0	ambient temperature, K	fo	fluid outlet
t	temperature, ^oC	i	inlet
U	overall heat transfer coefficient, $W/m^2 \cdot K$	o	outlet
Greek symbols		p	plain tube
ΔP	pressure drop, Pa	sy	water-bath
Δt_m	logarithmic mean temperature difference, ^oC	w	pipe wall

1. INTRODUCTION

Since the 1960s, energy resources have become increasingly scarce as a result of the rapid development of industry. In order to maximize the use of energy and raw materials, various kinds of techniques have been used in the past for heat transfer enhancement in the petroleum industry, refrigeration engineering, and the power and nuclear energy industries. Among them are the following: (a) mixing the main flow with the flow in the wall region using rough surface and inserts, (b) reducing the boundary layer thickness using interrupted fin geometries or jet impingement, (c) creating rotational or secondary flow using swirl flow devices or duct rotation, and (d) raising the turbulence intensity with rough surfaces and turbulence promoters (Webb, 1994). Enhanced tubes are high-efficiency heat exchange elements. They have been widely applied in the chemical, petroleum, power, and seawater desalinization industries. Several new enhanced heat transfer elements have attracted people's attention to their performance. Extensive research has been conducted on the performance of enhanced heat transfer elements. Chen et al. (2004a,b) suggested that the augmentation of heat transfer in convergent-divergent tubes should be attributed to the disturbance of the near-wall fluid, intensified radial velocity, and turbulent intensity. Webb and Li (2000) analyzed the results of long-term fouling tests for cooling tower water flowing inside enhanced tubes and found that the potential for fouling increases as the number of starts and helix angle increases. Deng and Zhang (2004) indicated that a convergent-divergent tube is famous for its augmentation of heat transfer on both inside and outside fluid as well as its good anti-fouling characteristics. Some investigators (Xiao et al., 2007; Zeng et al., 2002) revealed that corrugated tubes can significantly enhance heat transfer under the same conditions. However, enhanced heat transfer elements have an advantage on heat transfer and exergy efficiency over the corresponding plain tube, although experiencing an increased pressure drop. At the same time, to consistently evaluate enhanced heat transfer elements on their anti-fouling performance is difficult. In this paper, experimental investigations are reported

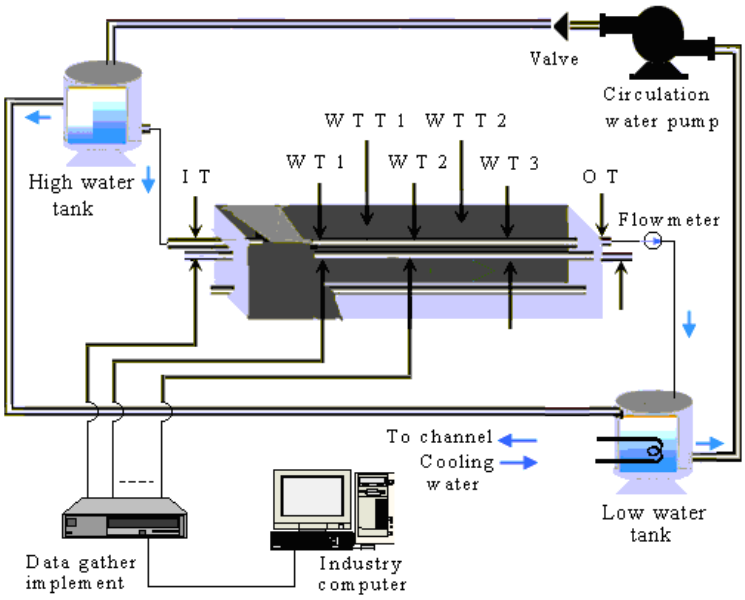

FIGURE 1. Experimental system.

in an attempt to gain a better understanding of the applied performance of several enhanced heat transfer elements. The final aim is to identify optimal enhancement techniques for heat exchangers.

2. EXPERIMENTAL PROCEDURES

2.1 Experimental System

The experimental system is shown in Fig. 1. Two single-tube heat exchangers share a constant temperature water tank (only one set of the two experimental systems is shown in the figure). In this system, one is composed of a plain tube, and the other, enhanced tubes. Experimental working fluid flows inside the tubes, which is collocated in the constant temperature water tank. The water in the tank is heated by a rod type electricity heater, which is controlled by a temperature control instrument to keep the water temperature constant. The water tank temperature (WTT) and wall temperature (WT), as well as inlet and outlet water temperatures (ITs and OTs) and water flow through the water tank, are monitored during the experimental process. Those monitored points are all fixed on the experimental tube segments. During the process, the water is pumped from a low (position) water tank to a high water tank. The high water tank supplies the water to the experimental tube segment and keeps the water flow constant. A computer is used for data collection, processing, display, and storage.

The ITs and OTs and WTTs are measured by Pt100 thermal resistance, whose permissible error is $\pm(0.15 + 0.002|t|)\%$. The WTs are measured by T-type thermocouples, whose permissible error is $\pm 0.4\%\ t\ ^{\circ}\mathrm{C}$. The water flow is measured by a turbine flux sensor, whose permissible relative error is ±1%.

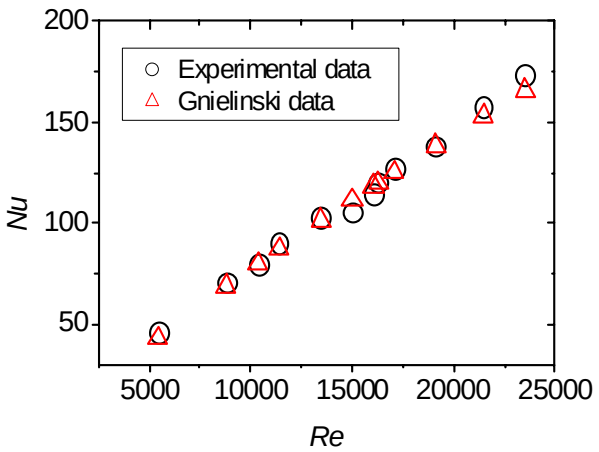

FIGURE 2. Comparison of the Nusselt number between the experimental data and the Gnielinski correlation data for the plain tube.

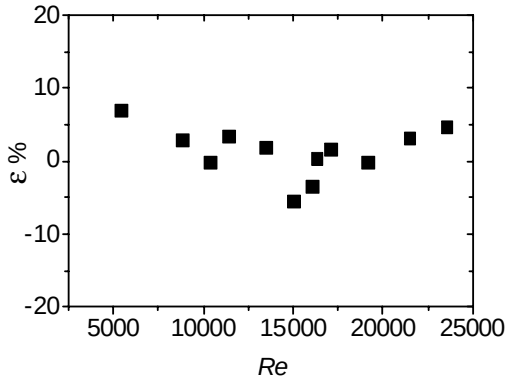

FIGURE 3. The relative error between the experimental data and the Gnielinski correlation data for the plain tube.

The error analysis of the measuring system is carried out based on the methods introduced in (Gnielinski, 1976; Yang and Tao, 2003; Glen et al., 1997). Figure 2 shows the results of the experimental Nusselt number and the calculated data by the classical Gnielinski correlation. The relative error of the Nusselt number between the experimental and calculated data is also given in Fig. 3. The relative error of the experimental system is within 7%. The experimental results are thus reasonable and reliable.

2.2 Interrelated Formulas

The definitions of the Nusselt number and friction factor are as follows:

$$Nu = \frac{hd}{\lambda} \tag{1}$$

$$f = \frac{\Delta p}{2\rho u^2}\frac{d}{l} \tag{2}$$

The overall heat transfer coefficient U can be obtained from the heat transfer equation:

$$U = \Phi/(\pi d l \Delta t_{\mathrm{m}}) \tag{3}$$

$$\Phi = \rho \pi d^2 u c_p (t_{\mathrm{fo}} - t_{\mathrm{fi}})/4 \tag{4}$$

where Φ, ρ, and c_p are the heat flux, the density, and the specific heat at constant pressure of the working fluid, respectively. Δt_{m} is the logarithmic mean temperature difference, which is given by:

$$\Delta t_{\mathrm{m}} = \frac{(t_{\mathrm{sy}} - t_{\mathrm{fi}}) - (t_{\mathrm{sy}} - t_{\mathrm{fo}})}{\ln((t_{\mathrm{sy}} - t_{\mathrm{fi}})/(t_{\mathrm{sy}} - t_{\mathrm{fo}}))} \tag{5}$$

Here, t_{sy} is the WTT of the tube side.

The fouling thermal resistance is defined as follows (Yang and Tao, 2003):

$$R_{\mathrm{f}} = \frac{1}{U} - \frac{1}{U_0} \tag{6}$$

where U_0 and U are the overall heat transfer coefficients under clean and fouling conditions, respectively, which can be determined by Eq. (3). In the end, fouling thermal resistance can be calculated.

The exergy efficiency is defined as (Chen and Li, 1999):

$$\eta = \frac{E}{E_{\mathrm{XQ}}} \times 100\% \tag{7}$$

where, E and E_{XQ} are the exergy of heat absorption and the exergy of heat transfer, which can be determined by Eqs. (8) and (9)

$$E_{XQ} = Q(1 - \frac{T_0}{T}) \tag{8}$$

$$E = \int_T^{T_0} (1 - \frac{T_0}{T}) G c_p dT = Q - G c_p T_0 \ln \frac{T_0}{T_i} \tag{9}$$

2.3 Experimental Material and Configuration

Figure 4 shows a sketch of the enhanced tubes used in the present study. The geometry details are listed in Table 1. Additionally, the picture of enhanced tubes in the experiments is shown in Fig. 5.

3. EXPERIMENTAL RESULTS

3.1 Pressure Drop and Friction Factor

Enhanced tubes must have a small pressure drop and friction factor, which have a significant effect on their practicality. In order to compare and contrast the advantages and disadvantages of different enhanced tubes, the test experiments were carried out in a lab. For different enhancement tubes, the pressure drop relies heavily on the Reynolds number, as shown in Fig. 6. The plain tube has the smallest pressure drop, the arc line tube has the largest pressure drop, and convergent-divergent tubes and the corrugated tube fall in between. With various Reynolds numbers, the pressure drop for the arc line tube is 3.7–9.0 times that for the plain tube, 3.4–5.4 times and 3.2–4.4 times for convergent-divergent tubes I and II, respectively, and 2.0–4.3 times for the corrugated tube. The friction fac-

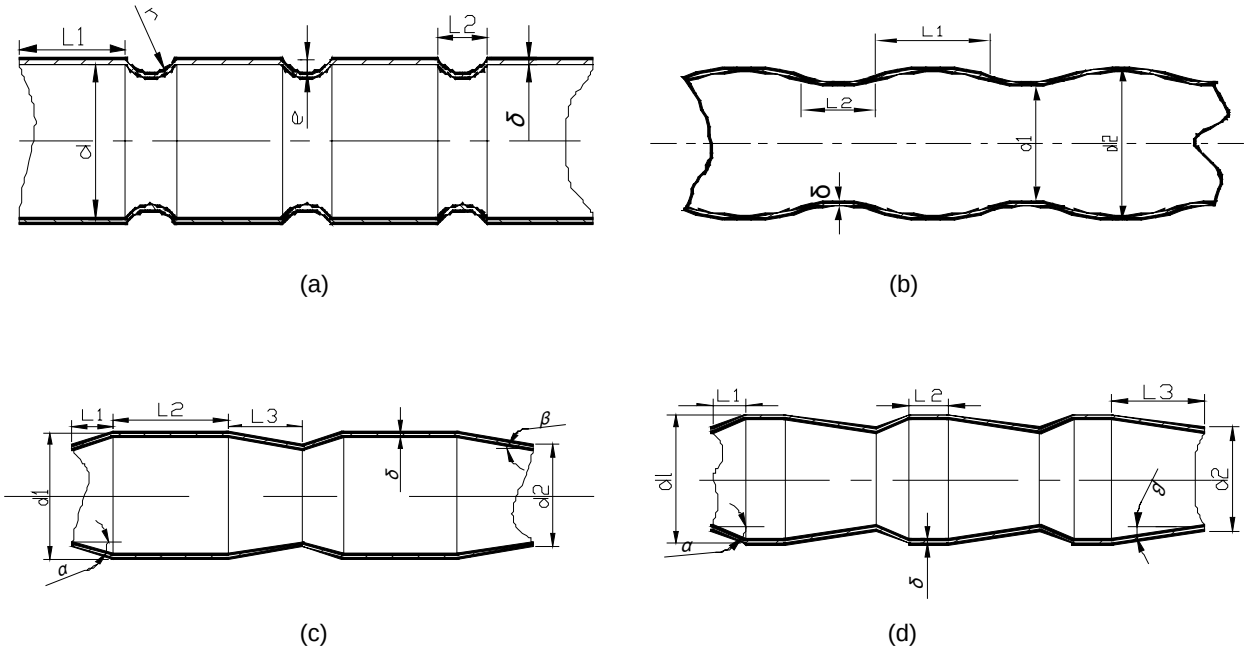

FIGURE 4. Section sketch map of enhanced tubes.

TABLE 1: Material and Geometry Dimension

Type	Material	Geometry dimension, mm							Degree	
		L1	L2	L3	d1	d2	δ	*r*	α	β
Arc line tube	*St*	17	8		22		1.5	5		
Corrugated tube	*St*	16	10		24	30	0.8		27	10
Convergent-divergent tube I	*St*	5	6	14	25	20	1.5		20	11
Convergent-divergent tube II	*St*	7	20	13	25	20	1.5			
Plain tube	*St*				25		1.5			

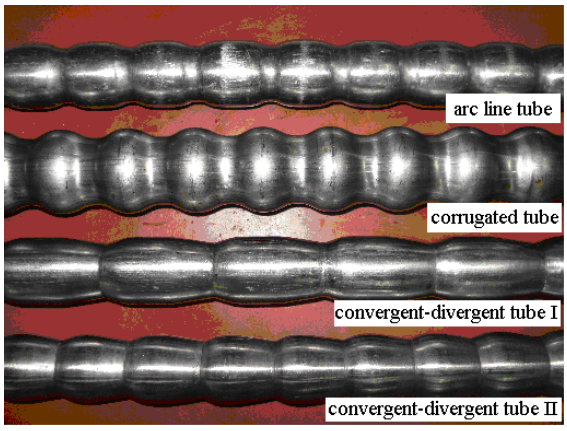

FIGURE 5. Picture of enhanced tubes.

tor versus the Reynolds number for the enhanced tubes and the plain tubes is shown in Fig. 7. Each enhanced tube has a higher friction factor than that of the plain tube. The friction factor of arc line tubes is the largest, approximately 7.2 times that of plain tubes. However, the corrugated tubes have the smallest friction factor, approximately 3.1 times that of plain tubes, the convergent-divergent tubes I and II fall in between, their friction factor being approximately 6.1 and 3.3 times that of plain tubes, respectively. A comparison of the friction factor for the plain tube and the enhanced tubes is summarized in Table 2. According to Figs. 6 and 7, we could conclude that arc line tubes would be at a disadvantage in applicability.

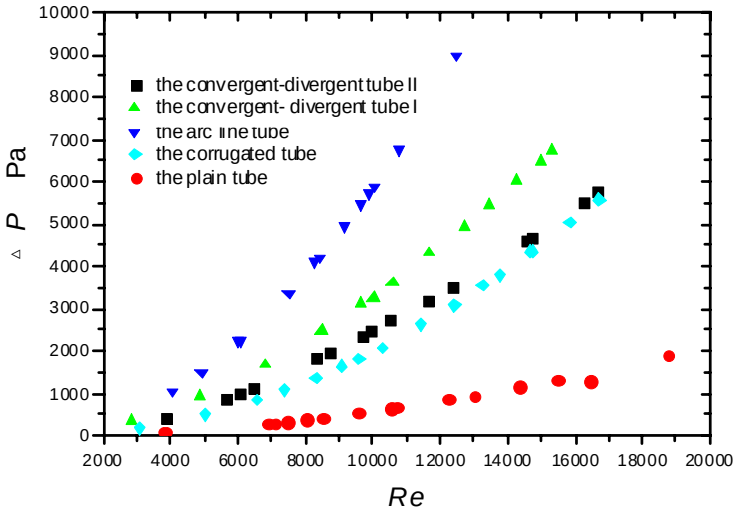

FIGURE 6. Pressure drop characteristic.

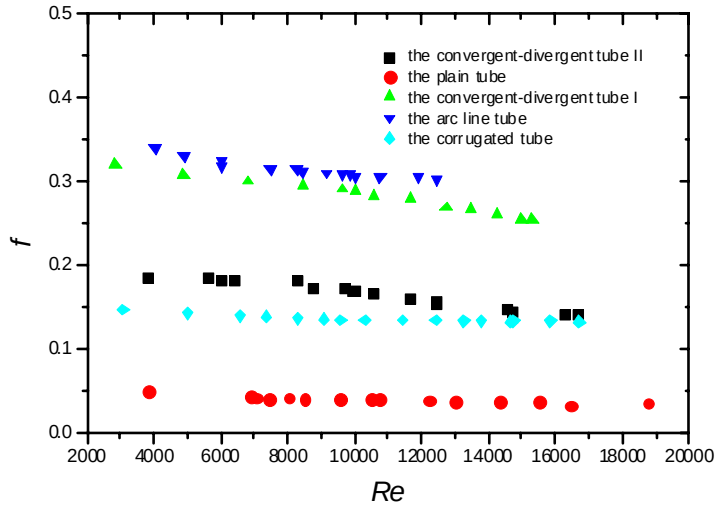

FIGURE 7. Friction factor characteristic.

TABLE 2: Comparison of Friction Factors for Enhanced Tubes and Plain Tube

Type	Re	Correlation of friction factor	f_e/f_p
Arc line tube	4045 < Re < 12,479	$f = 0.75268\ \mathrm{Re}^{-0.09697}$	7.2
Corrugated tube	3687 < Re < 17,654	$f = 0.23951\ \mathrm{Re}^{-0.06097}$	3.1
Convergent-divergent tubes I	2855 < Re < 15,306	$f = 0.92551\ \mathrm{Re}^{-0.1297}$	6.1
Convergent-divergent tubes II	3826 < Re < 16,643	$f = 1.05023\ \mathrm{Re}^{-0.2009}$	3.3
Plain tube	3826 < Re < 18,747	$f = 0.26804\ \mathrm{Re}^{-0.20518}$	1

3.2 Comparison of Heat Transfer Performance

Figure 8 shows the variation of the Nusselt number with the Reynolds number. The heat transfer of a plain tube is compared with that of enhanced tubes. The Nusselt number correlations for enhanced tubes and a plain tube are obtained based on the experimental data and are given in Table 3. The experimental results show that all Nusselt numbers increase with increasing Reynolds number, and the Nusselt numbers of enhanced tubes are larger than that of the corresponding plain tube. The main reason is that the thickness of the boundary layer in enhanced tubes is thinner and therefore offers a smaller thermal resistance. Even if the enhanced tubes have an advantage in heat transfer performance, the increase in the Nusselt number is fairly flat for convergent-divergent tubes I and II and arc line tubes. The Nusselt number of a corrugated tube increases dramatically with the increased Reynolds number. Clearly, with high Reynolds numbers a corrugated tube has the best heat transfer performance. The experimental data shows that with a low Reynolds number (Re ≤ 10,000) for an arc line tube, convergent-divergent tubes I and II, and a corrugated tube, the corresponding increases in heat transfer are 57.1%, 42.5%, 31.5%, and 114%, respectively. With high Reynolds numbers, convergent-divergent tube II has no distinct advantage. A comparison of heat transfer for a plain tube and enhanced tubes is summarized in Table 3.

The exergy coefficients of the four tubes can be obtained using Eq. (7). Figure 9 shows the curves for the exergy coefficients under the same experimental conditions. Clearly, all the enhanced tubes have a higher exergy coefficient than the plain tube. The corrugated tube has the highest exergy coefficient, which is approximately 1.14–1.19 times that of the other tubes. Convergent-divergent tube II does not have a distinct advantage in terms of the exergy coefficient over the other enhanced tubes. Additionally, with the change in

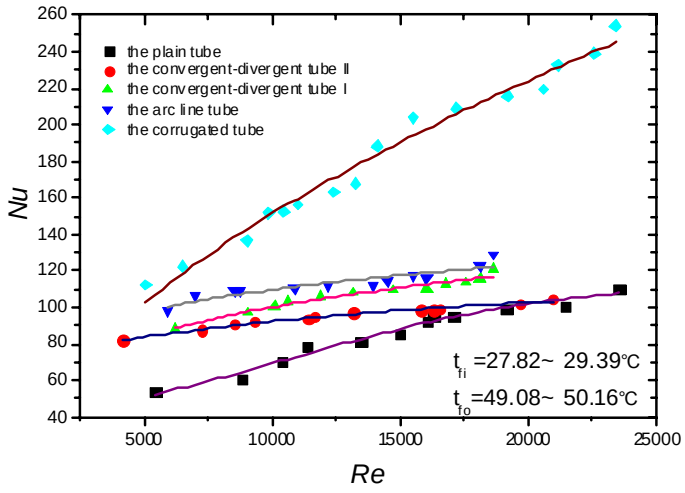

FIGURE 8. Comparison of the Nusselt number between enhanced tubes and a plain tube.

TABLE 3: Comparison of Heat Transfer for Enhanced Tubes and Plain Tubes

Type	Re	Correlation of Nu	U_p/U_e (clean)	U_p/U_e (fouled)
Arc line tube	5949 < Re < 18,624	Nu = 22.436 $Re^{0.1723}$	1.08	1.21
Corrugated tube	5079 < Re < 23,422	Nu = 0.815 $Re^{0.5671}$	1.28	1.39
Convergent-divergent tube I	6208 < Re < 18,624	Nu = 9.908 $Re^{0.2511}$	1.09	1.17
Convergent-divergent tube II	4138 < Re < 20952	Nu = 23.578 $Re^{0.1484}$	1.13	1.21
Plain tube	5432 < Re < 23,539	Nu = 0.5993 $Re^{0.5179}$		

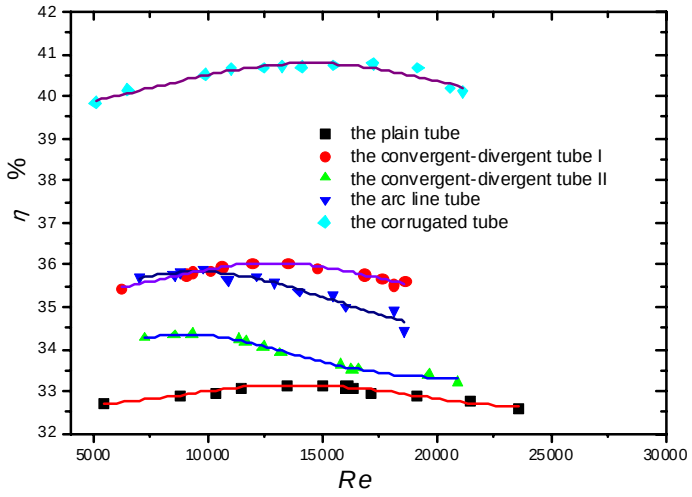

FIGURE 9. Comparison of the coefficient of exergy.

the Reynolds number, the exergy coefficient curves show peak values. A possible reason is that as the heat transfer performance and the friction factor increase with increasing Reynolds number, so the peak value is a result of the combined effects of both properties.

3.3 Comparison of Anti-Fouling Performance

The anti-fouling performance of enhanced tubes must be tested in practical applications. A certain proportion of calcium chloride and sodium hydroxide was added in solution. Calcium ions (Ca^{2+}) react with the carbonate ions (CO_3^{2-}) in the solution, forming calcium carbonate crystal ($CaCO_3$). Since $CaCO_3$ does not dissolve easily in water, its deposition on the heat transfer surface leads to crystallization fouling. The anti-fouling performance of the enhanced tubes is shown in Fig. 10 under constant experimental conditions. The experimental results show that the fouling asymptotic resistance of enhanced tubes is smaller than that of the corresponding plain tube. The arc line tube,

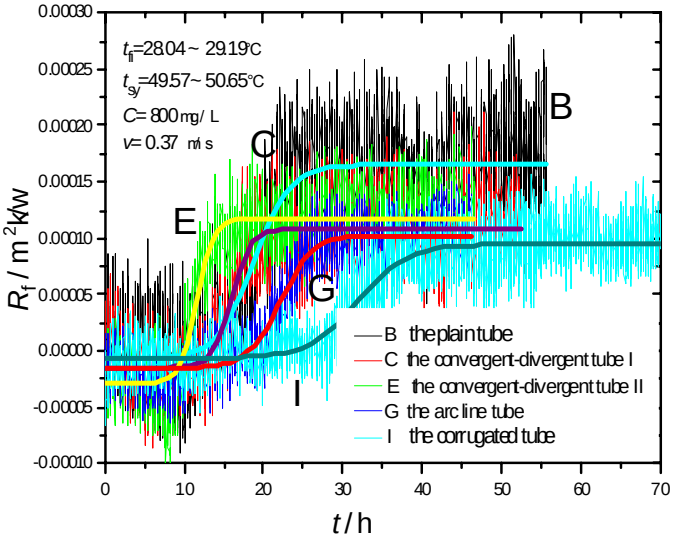

FIGURE 10. Fouling characteristics of enhanced tubes and a plain tube.

TABLE 4: The Experimental Values of Fouling for Enhanced Tubes and Plain Tube

Type	Induction period (h)	Fouling asymptotic resistance (m^2·K/W)	Fouling asymptotic resistance ratio
Arc line tube	20	1.0299E-4	0.623
Corrugated tube	27	9.4658E-5	0.655
Convergent-divergent tubes I	15	1.0841E-4	0.573
Convergent-divergent tubes II	10	1.1793E-4	0.713
Plain tube	13	1.6543E-4	1

convergent-divergent tubes I and II, and the corrugated tube display 62.3%, 57.3%, 71.3%, and 65.5% of the fouling asymptotic resistance of plain tubes, respectively. This is because the increase in turbulent intensity can increase the fouling remove rate and enhance the anti-fouling performance of the enhanced tubes. On the other hand, the induction period is a very important factor for assessing the anti-fouling performance of enhanced tubes. The induction period is strongly dependent on the operating conditions. For commercial applications, the induction period should be as long as possible. The induction periods of the enhanced tubes and the plain tube are shown in Fig. 10. The corrugated tube has the longest induction period, which is approximately 27 hours. Convergent-divergent tube II has the shortest induction period, which is approximately 10 hours. The induction periods of convergent-divergent tube I and the arc line tube are approximately 15 hours and 20 hours, respectively. A comparison of the fouling characteristic for a plain tube and enhanced tubes is summarized in Table 4. Based on these results, one can observe that the corrugated tube has advantages on the fouling asymptotic value and the induction period over other tubes.

3.4 Comparison of Heat Transfer Performance under Clean and Fouled Condition

In order to compare the heat transfer performance change caused by fouling between the enhanced tubes and the plain tubes, the experimental data were measured once a minute at the end of experiments. The experimental results are shown in Figs. 11 and 12. In the

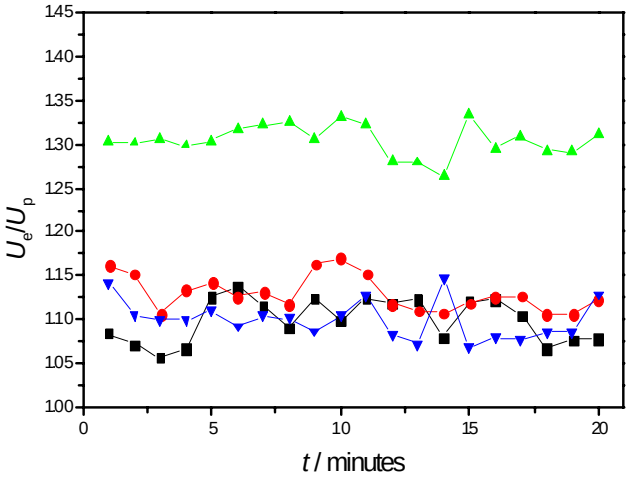

FIGURE 11. Comparison of enhancement ratio under clean conditions: –■– — convergent-divergent tube I and plain tube; –▲– — corrugated tube and plain tube; –●– — convergent-divergent tube II and plain tube; ▾ — arc line tube and plain tube.

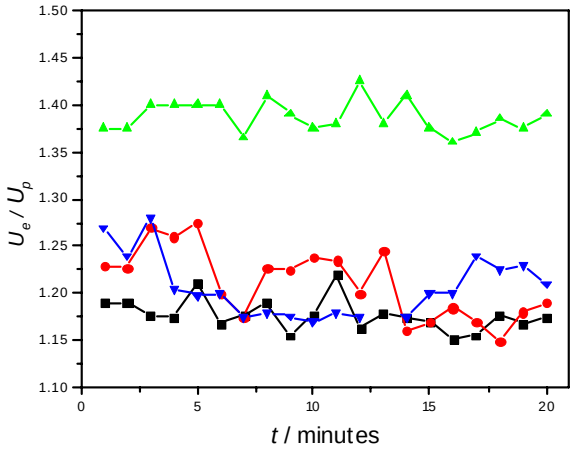

FIGURE 12. Comparison of enhancement ratio under fouled conditions: –■– — convergent-divergent tube I and plain tube; –▲– — corrugated tube and plain tube; –●– — convergent-divergent tube II and plain tube; ▼ — arc line tube and plain tube.

two figures, the enhanced ratio (U_e/U_p) of the arc line tubes under clean conditions is approximately 1.11, and 1.21 under fouling conditions. The enhanced ratios for convergent-divergent tubes I and II are 1.09 and 1.13 under clean conditions, and 1.17 and 1.21 under fouling conditions, respectively. A comparison of the enhanced ratio for a plain tube and enhanced tubes is summarized in Table 3. One can observe that the enhanced tubes have a better heat transfer performance than the plain tube under both clean and fouled conditions.

4. CONCLUSIONS

The friction factor, the heat transfer performance, and the fouling characteristics of the enhanced tubes and the plain tubes have been experimentally investigated in this paper. The results show that although the enhanced tubes tested in this work have a higher pressure drop, they have the advantage in anti-fouling performance over plain tubes. Moreover, they have better heat transfer performance both under clean and fouling conditions. According to the comparison of the experimental results, the corrugated tube has the best heat transfer and anti-fouling performance. The second best is convergent-divergent tube II, and the third best is convergent-divergent tube I, with the arc line tube ranked last.

ACKNOWLEDGMENT

This work is supported by the Special Funds for Major State Basic Research Projects of China (2007CB206904), National Natural Science Foundation of China (50576009) and Technology Bureau of Jilin Province (20070529). The authors are grateful for this support.

REFERENCES

Chen, W. W. and Li, H. P., *Thermodynamic Analysis and Energy Conservation*, Science Press, Beijing, pp. 166–167, 1999.

Chen, Y., Deng, X. H., and Ding, X. J., Augmentation heat transfer of converging-diverging tube. I. Mechanism of field synergy principle, *J. Chem. Ind. Eng.*, vol. 55, no. 11, pp. 1760–1763, 2004.

Chen, Y., Deng, X. H., and Ding, X. J., Augmentation heat transfer of converging-diverging tube. II. Optimal geometry configuration, *J. Chem. Ind. Eng*, vol. 55, no. 11, pp. 1764–1767, 2004.

Deng, X. H. and Zhang, Y. J., Axial flow-type heat exchanger with convergent-divergent tube, China, 1140764, 2004-03-03, 2004.

Glen, N. F., Howarth, J. H., and Jenkins, A. M., The estimation of errors and uncertainty in the determination of fouling resistances, *Proc. Int. Conf.*

on Understanding Heat Exchanger Fouling and Its Mitigation, Italy, pp. 342–451, 1997.

Gnielinski, V., New equations for heat and mass transfer in turbulent pipe and channel flows, *Int. J. Chem. Eng*., vol. 16, pp. 359–368, 1976.

Webb, R. L., *Principles of Enhanced Heat Transfer*, John Wiley & Sons, New York, pp. 3–11, 1994.

Webb, R. L. and Li, W., Fouling in enhanced tubes using cooling tower water. Part I: Long term fouling data, *Int. J. Heat Mass Transfer*, vol. 43, no. 19, pp. 3567–3578, 2000.

Xiao, J. H., Qian, C. F., and Huang, Z. X., Study of effects and mechanisms of heat transfer enhancement of corrugated tubes, *Chem. Eng. (China)*, vol. 35, no. 1, pp. 12–15, 2007.

Yang, S. M. and Tao, W. Q., *Heat Transfer*, 3rd ed., Higher Education Press, Beijing, pp. 164–166, 2003.

Zeng, M., Wang, Q. W., Qu, Z. G., Experimental study on the pressure drop and heat transfer characteristics in corrugated tubes, *J. Xi'An Jiaotong Univ*., vol. 36, no. 3, pp. 237–240, 2002.

Journal of Enhanced Heat Transfer, 17(4) 343–352 (2010)
Reprints available directly from the publisher.
Photocopying permitted by license only.

Effects of Nanoparticle Parameters on Thermal Performance of the Evaporator in a Small Capillary Pumped Loop Using Nanofluid

LUN-CHUN LV & ZHEN-HUA LIU*

School of Mechanical and Power Engineering, Shanghai Jiaotong University,
Shanghai 200240, P. R. China

An experimental study was carried out to understand the effects of the nanoparticle parameters on the thermal performance of the evaporator in a capillary pumped loop (CPL) with nanofluid as the working fluid. The study focused on the influence of the nanoparticles mass concentration, the nanoparticle type, and the nanoparticle size on the heat transfer coefficient of the evaporator and the maximum heat flux. The experimental results indicated that the thermal performance of the evaporator in the CPL is improved with the addition of nanoparticles. There exists an optimal nanoparticles mass concentration corresponding to the maximum heat transfer enhancement. And the optimal nanoparticles mass concentrations are 1.0% and 0.5% for Cu nanofluid and CuO nanofluid, respectively. The nanoparticle type and the nanoparticle size influence the thermal performance of the CPL. The maximum heat flux is increased with the addition of nanoparticles in the working liquid.

Key words: capillary pumped loop; nanofluid; heat transfer; nanoparticle

*Corresponding author: Zhen-hua Liu: liuzhenh@sjtu.edu.cn

NOMENCLATURE

A	area of the bottom of the evaporator, m^2	T_s	saturated temperature of the vapor, ^oC
h	average heat transfer coefficients of the evaporator, $W/m^2 \cdot K$	**Greek symbols**	
P_s	saturated pressure of vapor, kPa	δ	thickness of the bottom of the evaporator, m
Q	heat input, W	λ	thermal conductivity, W/m·K
q	heat flux, kW/m^2	ω	nanoparticles mass concentration, %
q_{max}	maximum heat flux, W/m^2	**Subscripts**	
T_{eo}	average outer wall temperature of the evaporator, ^oC	n	nanofluid
T_{ew}	average inner wall temperature of the evaporator, ^oC	w	water

1. INTRODUCTION

The pursuit of high performance and miniaturization of electronic component in recent years leads to the production of more heat per unit volume. As a result, how to dissipate the heat becomes a critical factor in the electronic product design. As a high-efficiency, convenient heat-exchanging device, the capillary pumped loop (CPL) has caught more and more attention.

The CPL is a two-phase thermal control system which uses capillary forces formed at the vicinity of the porous wick surface to transport the working liquid. The major advantages of the device include a very high thermal conductivity, no moving parts, no pumping power requirement and it is capable of transporting heat over large distances with a minimal temperature difference.

A large number of investigations have been conducted on heat transfer in CPL. The first CPL was proposed by Stenger (1966) but it received special attention in the late 1970s. At that time, CPL technology had been developed as an option for transporting thermal energy within spacecrafts, satellites (Jentung Ku, 1993; Maidanik, 1999), and the reservoir of the CPL had been used for temperature control as well as storing excess working fluid and providing pressure priming (Faghri, 1995). Currently, miniaturization of CPL is at the forefront of an extensive research and development to provide cooling solution to the high load/heat flux problem of advanced electronic packaging (Triem et al., 2003). At the same time, CPLs without the reservoir have appeared. Chen and Lin (2001) carried out a research on using the CPL for cooling electronic chips. The CPL they designed had no reservoir and the evaporator was a flat one with porous material as a capillary structure. They investigate the parameters affecting the thermal performance of the CPL. Figus et al. (2003) carried out a research to apply the CPL for cooling the printed circuit board (PCB). The evaporator is a flat evaporator and their device did not have the reservoir. Muraoka et al. (1998) carried out an experimental and theoretical research on a CPL with a flat evaporator and no reservoir. Their research showed that the CPL without a reservoir could be used in the heat resource that does not need a precise control.

Since the heat pipe utilizes phase change of the working fluid to transfer heat, the selection of working fluids is of essential importance in achieving maximum heat transfer. The concept of nanofluid (nanoparticle suspension) as a working fluid was first proposed due to its anomalous heat transfer characteristics by Choi (1995). Nanofluid is a colloidal suspension with nanoparticles dispersing uniformly in a base fluid. A lot of researches then have been carried out to study the thermal characteristics, convective heat transfer, and pool boiling heat transfer. Recently, enlightened by the enhanced heat transfer of nanofluids, some researchers used nanofluids in heat pipes to enhance their heat transfer performance. But these researches were on the thermosyphon (Liu et al., 2007; Xue et al.,

2006b), traditional heat pipes with grooves as the wick structure (Wei et al., 2005; Kang et al., 2006; Liu et al., 2007a) or a wire mesh screen as the wick structure (Tsai et al., 2004) and oscillating heat pipe (Ma et al., 2006). All these researches proved that the addition of nanoparticles in the working fluid could lead to a decrease in the wall temperature of the evaporator and an increase in the heat transport capability. So far, no investigation has been performed to understand the effects of the type of nanoparticle and the size of nanoparticle on the thermal performance of CPL with nanofluid as the working liquid. Most of the researches were carried out under the condition that the input was same and the cooling condition was stable, which lead to the heat pipe working under different operational temperature. It is imperfect to understand the effect of nanoparticles on the thermal performance of the heat pipe.

The present study is aimed at fundamental understanding of the application of nanofluid in the CPL with a flat evaporator. Effects of the nanoparticles mass concentration, the type and the size of nanoparticles on the heat transfer coefficient and the maximum heat flux of the CPL were investigated.

2. EXPERIMENTAL APPARATUS AND PROCESS

2.1 Experimental Apparatus

Figure 1 shows the schematic diagram of the experimental apparatus. The apparatus consisted of a capillary pumped loop, the DC power supply, a data acquisition system, and a computer. The capillary pumped loop was composed of a flat evaporator, a condenser, a vapor line, and a liquid line. The evaporator was made of copper. The evaporator was heated by a skin heater which was mounted at the bottom wall of the evaporator and the heat power was supplied by a DC power supply. The measured voltage drop across the skin heater and the current were used to calculate the heat input. The vapor in the condenser was cooled by the cooling water from a constant-temperature thermal bath. All signals from the thermocouples and pressure transducer were input to the data acquisition system (Agilent-34970) which was fed into the computer. The temperature of the cooling water was adjusted to keep the operational pressure at a constant value for varying heat inputs. The design characteristics of the CPL are shown in Table 1.

Figure 2 shows the detailed schematic diagram of the evaporator, which is similar to one of the three types of evaporators mentioned by Faghri (1995). The evaporator consisted of the base, mesh screens, the supporter of the screen, the vapor line, the liquid line, and the flange. The viton o-ring was used to seal between the base and the flange. The supporter of the mesh screens was used to keep the mesh close to the wall. Two mesh layers were used in this CPL and the wick was made of a stainless steel mesh screen. The mesh screens at the bottom were 150 meshes with a thickness of 2 mm, and the mesh screens at the top were 300 meshes with a thickness of 6 mm. The reason for choosing the lower mesh is to decrease the flow resistance of the fluid in the mesh layers.

Ten 0.1-mm Omega thermocouples were mounted on the CPL to measure the surface temperature distribution. Five thermocouples were installed on the bottom wall of the evaporator, one of which at the center

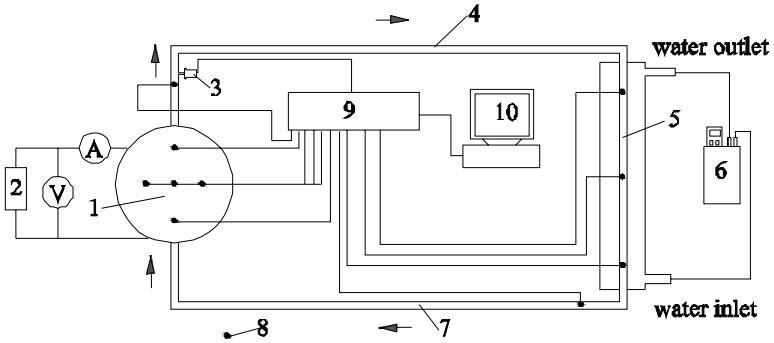

FIGURE 1. Schematic diagram of the experimental apparatus: 1 — evaporator; 2 — DC power supply; 3 — pressure transducer; 4 — vapor line; 5 — condenser; 6 — thermostat reservoir; 7 — liquid line; 8 — thermocouple locations; 9 — digital acquisition system; 10 — computer.

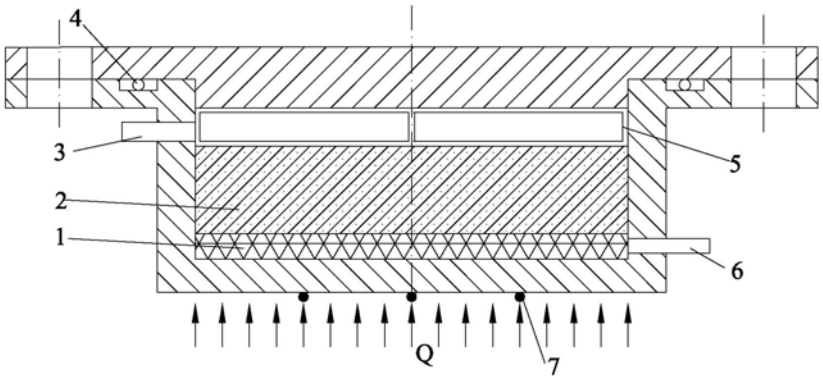

FIGURE 2. Schematic diagram of the evaporator: 1 — 150 meshes; 2 — 300 meshes; 3 — vapor line; 4 — viton o-ring; 5 — support of mesh; 6 — liquid line; 7 — thermocouple locations.

TABLE 1: Structural Parameters of the CPL System

Evaporator		Vapor line	
Outside diameter:	0.036 m	Outside diameter:	0.004 m
Inner diameter:	0.031 m	Inner diameter:	0.003 m
Inner height:	0.014 m	Length:	0.45 m
Thickness of the bottom:	0.003 m		
Condenser		Liquid line	
Outside diameter:	0.004 m	Outside diameter:	0.004 m
Inner diameter:	0.003 m	Inner diameter:	0.003 m
Length:	0.26 m	Length:	0.45 m

of the bottom, and the others uniformly distributed on an axial position 7.5 mm to the center. The wall temperature of the evaporator was the average of the five thermocouples. One thermocouple was installed at the outlet of the evaporator to measure the temperature of the vapor. One thermocouple was installed at the outlet of the condenser to measure the temperature of the liquid. The others were installed equidistantly and the wall temperature of the condenser is the average of the measurement of the three. A pressure transducer was installed at the outlet of the evaporator to measure the pressure of the vapor.

2.2 Working Fluids

In the present experiment, pure water was use as the base fluid and the nanofluid consisted of the base fluid and the nanoparticles. The nanoparticles used in the experiment were Cu and CuO which were commercial products. The average diameters were 20 nm and 50 nm for Cu nanoparticles, and 50 nm for CuO nanoparticles. Before each test, the nanoparticles and the base fluid were poured into an ultrasonic water bath for about 10 hours to prepare the nanofluid. The nanoparticles mass concentrations of nanofluid ranged from 0.1% to 2.0%.

2.3 Experimental Process

At the beginning of each test, the whole system was vacuumed to a pressure of 0.08 Pa before the charging of the working liquid. The experiment was carried out at a steady operational pressure, which was 15.74 kPa and the filling ratio was 55%. During each run, the temperature of the cooling water was carefully adjusted to keep the operating pressure at a stable state at each input. When the wall temperatures of the vapor line could be kept stable for a long time, the signals of

the thermocouples and the pressure were sampled into the data acquisition system. The voltage and the current of the AC power supply were also recorded. After each run, the CPL was stopped from working for a week. Then the CPL was restarted and experiments were repeated. There was no meaningful difference between the results for different experiment runs. Because the nanoparticles were deposited at the bottom of the evaporator after the CPL stopped from work and after the CPL was restarted, the deposited nanoparticles reentered the working fluid under the natural convection of liquid and reformed the uniform nanofluid.

The steady thermal conduction equation is adopted to obtain the inner wall temperature of the evaporator, T_{ew},

$$T_{ew} = T_{eo} - Q\delta/(\lambda A) \tag{1}$$

The heat input was calculated by the measured voltage drop and the current. The average heat transfer coefficient h of the evaporator was calculated by the equation

$$h = Q/[A(T_{ew} - T_s)] \tag{2}$$

The maximum heat loss on the outside area of the heater was less than 3% according to the numerical calculation. The measurement error of the heated area was less than 0.5%. The truncation measurement error caused by the increment in the output of DC power was less than 1%. The measurement errors of electric voltage and the current were 0.1% and 0.1%, respectively. The maximum uncertainty of the pressure was 0.1%. The calibration errors of the thermocouples were 0.10°C. The maximum error of the inner wall temperature of the evaporator was 0.110°C. Therefore; the uncertainties of the heat flux and the heat transfer coefficient of the evaporator were not more than 4.7% and 7.1%, respectively.

3. EXPERIMENTAL RESULTS AND DISCUSSION

3.1 Effect of the Nanoparticles Mass Concentration on the Heat Transfer Coefficient of the Evaporator

Figure 3 shows the effect of the nanoparticles mass concentration on the heat transfer coefficients of the evaporator. It is found from Fig. 3 that the heat transfer coefficient of the evaporator is increased with the increasing of heat input. Then it slightly decreases. The heat transfer coefficient of the evaporator is increased with the addition of nanoparticles. For Cu nanofluid, it is found that the heat transfer coefficient of the evaporator is increased with the increasing nanoparticles mass concentration when the nanoparticles mass concentration is less than 1.0%. When the nanoparticles mass concentration is larger than 1.0%, it begins to decrease to some extent. For CuO nanofluid, it is found that the heat transfer coefficient of the evaporator is increased with the increasing nanoparticles mass concentration when the nanoparticles mass concentration is less than 0.5%. When the nanoparticles mass concentration is larger than 0.5%, it begins to decrease to some extent. Then it is concluded that there exists an optimal concentration for the evaporator which corresponds to the maximum heat transfer enhancement. The optimal concentration is 1.0%, 1.0%, and 0.5% for 20-nm Cu nanofluid, 50-nm Cu nanofluid, and 50-nm CuO nanofluid, respectively.

The properties that affect the heat transfer coefficient are the density of the liquid, the specific heat, the viscosity, and the thermal conductivity. Assuming the nanoparticles are not chemically reacting with water, the density of the nanofluid and the specific heat for the tested nanofluids remain almost constant with the value of pure water since the volume fraction is only on the order of 10^{-3}. Therefore the remaining possible factors for increasing the heat transfer coefficient are the thermal conductivity and the viscosity.

The mechanisms of heat transfer enhancement could be explained as follows. The thermal conductivity of the working liquid is increased when the nanoparticles are added. The stirring effect of nano-particles also enhances the natural convective heat transfer in the evaporator. The viscosity of the working liquid, which is increased with the adding of nanoparticles (Pak and Cho, 1998), leads to an increase of the boundary layer thickness and to a decrease of heat transfer. At the same time, since the nanoparticles cannot be carried by vapor during natural convective evaporating process, with the increase of the nanoparticles mass concentration, a large number of nanoparticles may accumulate at the vapor–liquid interface during the phase change. So the phase-change thermal resistance is strongly increased and the heat transfer is therefore restrained. Hence, there exists an optimal mass concentration for nanofluid working in CPL.

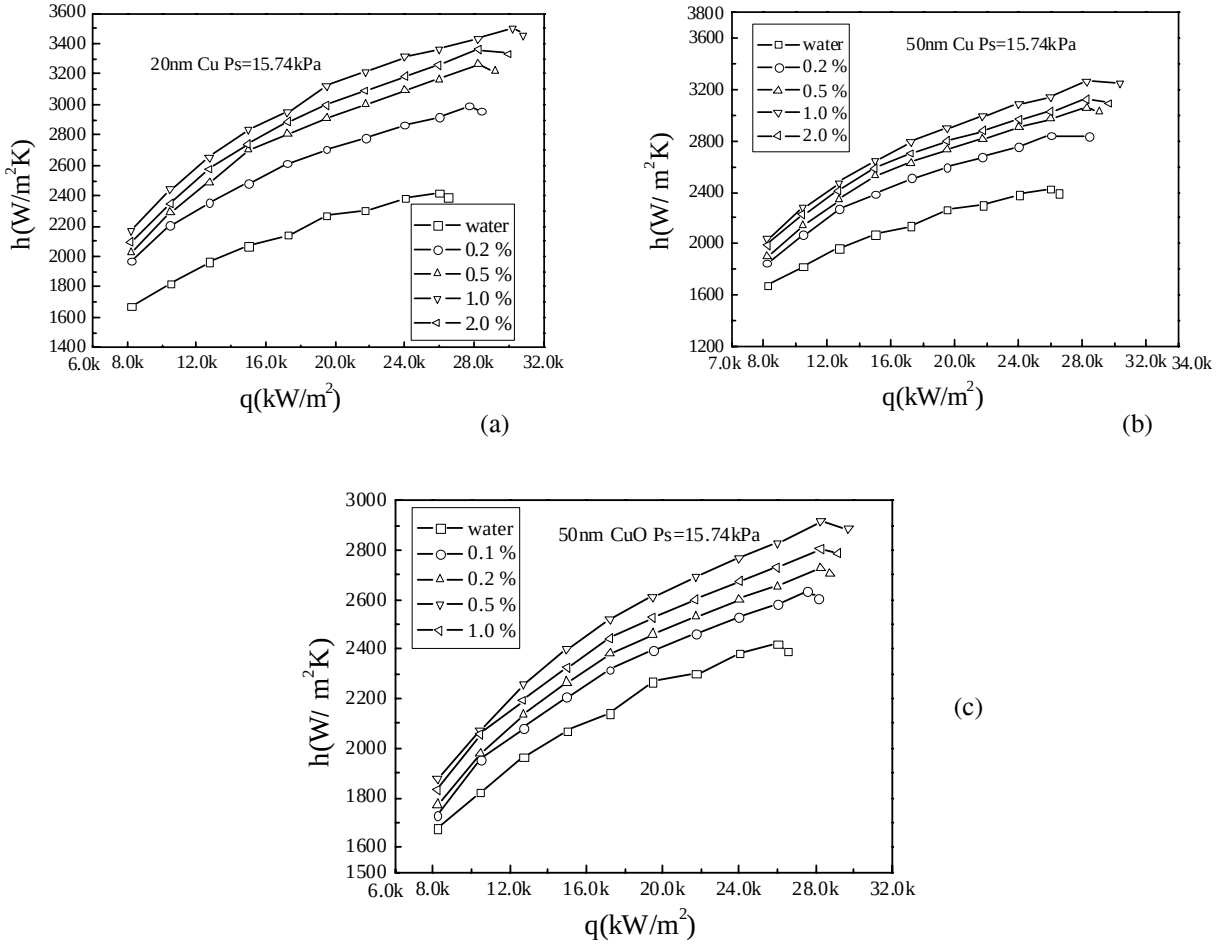

FIGURE 3. Effect of the nanoparticles mass concentration on the heat transfer coefficient of the evaporator: a) 20 nm Cu; b) 50 nm Cu; c) 50 nm CuO.

3.2 Effect of the Nanoparticle Type on the Heat Transfer Coefficient of the Evaporator

Figure 4 shows the effect of the nanoparticle type on the heat transfer coefficient of the evaporator of the CPL. The nanoparticles mass concentration was 1.0% and the nanoparticles were Cu nanoparticle and CuO nanoparticle whose average diameter was 50 nm.

It is found from Fig. 4 that the heat transfer coefficient of the evaporator for 50-nm Cu nanofluid is higher than that for 50-nm CuO nanofluid. The main reason is that one key factor influencing the effective thermal conductivity of nanofluid is the nature of the heat transport in nanoparticle. The thermal conductivities of Cu and CuO are 400 W/m K and 20 W/m·K, respectively. Then the thermal conductivity of Cu nanofluid is much higher than the thermal conductivity of CuO nanofluid, as a result of which the heat transfer coefficient of the evaporator for 50-nm nanofluid is higher than that for 50-nm CuO nanofluid. The maximal heat transfer coefficient of the evaporator for Cu nanofluid is increased 18% than that for CuO nanofluid.

3.3 Effect of the Nanoparticle Size on the Heat Transfer Coefficient of the Evaporator

Figure 5 shows the effect of the nanoparticle size on the heat transfer coefficient of the CPL. The nanoparticles mass concentration was 1.0%. The nanoparticles were 20-nm Cu nanoparticles and 50-nm Cu nanoparticles. It is found from Fig. 5 that the heat transfer co-

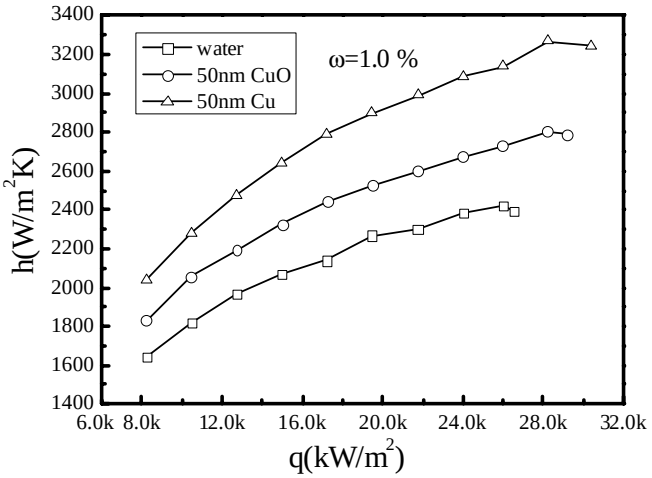

FIGURE 4. Effect of the nanoparticle type on the heat transfer coefficient of the evaporator.

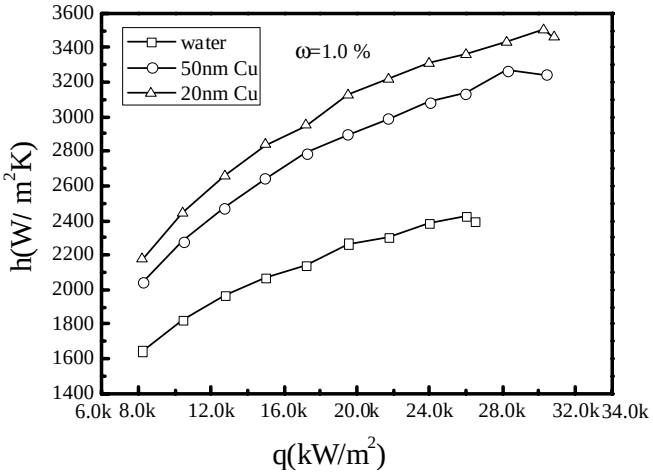

FIGURE 5. Effect of the nanoparticle size on the heat transfer coefficient of the evaporator.

efficient of the evaporator for 20-nm Cu nanofluid is higher than that for 50-nm Cu nanofluid. The main reason is that one key factor influencing the effective thermal properties of nanofluid is the size of the particle. The effective thermal conductivity of nanofluid becomes larger when the nanoparticle diameter decreased (Jang and Choi, 2007). As the particle size decreases, the Brownian motion of nanoparticles is greater and then the nanoconvection becomes dominant. Then the effective thermal conductivity of nanofluids becomes larger. The maximal heat transfer coefficient of the evaporator for 20-nm Cu nanofluid is higher about 10% than that for 50-nm Cu nanofluid.

3.4 Effect of Nanoparticles on the Maximum Heat Flux

Figure 6 shows the effect of nanoparticle type on the maximum heat flux enhancement ratio which is defined as the ratio of the maximum heat flux of nanofluid to that of pure water, at different nanoparticles mass concentraion. The nanoparticles used in the experiment were 20-nm Cu, 50-nm Cu, and 50-nm CuO. It is found from Fig. 6 that the maximum heat flux increased with the addition of the nanoparticles. For the CPL with nanofluid as the working liquid, the enhancement ratio increased with the increase of the

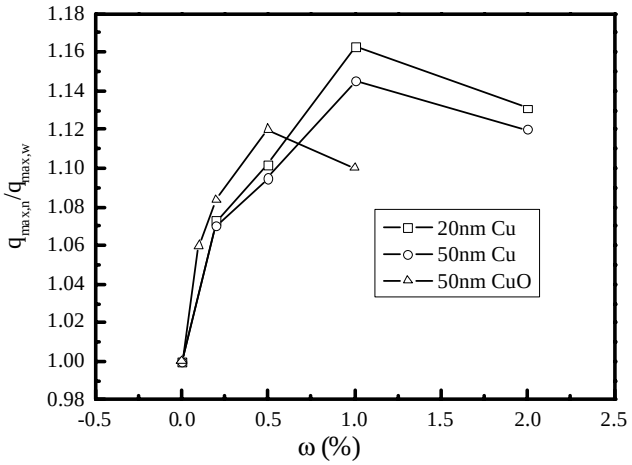

FIGURE 6. Effect of nanoparticles on the maximum heat flux.

nanoparticles mass concentration at the beginning and then decreased when the nanoparticles mass concentration is larger than one value. And the value is 1.0% and 0.5% for the Cu nanofluid and CuO nanofluid, respectively. It is also found from Fig. 6 that the maximum heat flux enhancement ratio, which for the CPL with 20-nm Cu nanofluid as the working fluid, is the largest and it can reach 16%. Then it is 50-nm Cu nanofluid which can reach 14.5%. The minimum is 50-nm CuO nanofluid which can reach 12%. The reason of the increase in the maximum heat flux may be the changes of the solid–liquid contact angle between the liquid and the stainless steel screen (Kim et al., 2007). The solid–liquid contact angle between the liquid and the stainless steel screen is reduced with the addition of nanoparticles which increases the capillary force. Then the maximum heat flux is increased.

The experiment mentioned above indicates that the thermal performance of the CPL with evaporator heated from bottom is improved with the addition of nanoparticles in the working liquid. In order to understand the influence of the different heat location to the thermal performance of the CPL with the nanofluid as the working liquid, a test was carried out to understand the influence of the addition of nanoparticles on the CPL heated from above of the evaporator. It was found that the thermal performance of the CPL with nanofluid as the working fluid is the same as that of the CPL with pure water as the working liquid. The reason was that the heat transport in the evaporator heated from above was only conductive and the nanoparticles deposited on the bottom under the influence of gravity. This makes the thermal performance of the CPL with nanofluid be the same as that of the CPL with pure water. It is concluded that the heat location influences the thermal performance of the CPL with nanofluid as the working liquid. The addition of nanoparticles in the working liquid is effective to the CPL heated from the bottom and it is ineffective to the CPL heated from above.

4. CONCLUSIONS

An experimental research was carried out to understand the effects of nanoparticle parameters on the thermal performance of the CPL with nanofluid as the working liquid. The conclusions are as follows:

1. The thermal performance of the evaporator in the CPL is improved with the addition of nanoparticles. The heat transfer coefficient and the maximum heat flux are increased with the addition of nanoparticles.
2. There exists an optimal nanoparticles mass concentration corresponding to the maximum heat transfer enhancement. The optimal nanoparticles mass concentration is 1.0% and 0.5% for Cu nanofluid and CuO nanofluid, respectively.
3. The nanoparticle type influences the thermal performance of the CPL. The higher the thermal conductivity of nanoparticles, the higher the thermal performance of the CPL.
4. The size of nanoparticles influences the thermal performance of the evaporator. The heat transfer

coefficient of the evaporator increased when the nanoparticle size decreased.

5. The maximum heat flux increased with the addition of nanoparticles. The maximum heat flux enhancement ratios are 16%, 14.5%, and 12% for 20-nm Cu nanofluid, 50-nm nanofluid, and 50-nm CuO nanofluid, respectively.

ACKNOWLEDGMENTS

This study was supported by the key foundation research project of the Science and Technology Bureau of Shanghai under Grant No. 04JC14049. Special thanks are also given to the Instrumental Analysis Center of Shanghai Jiaotong University.

REFERENCES

Chen, P. C. and Lin, W. K., The application of capillary pumped loop for cooling of electronic components, *Appl. Thermal Eng.*, vol. 21, pp. 1739–1754, 2001.

Choi, S. U. S., and Eastman, J., Enhancing thermal conductivity of fluids with nanoparticles, *Proc. 1995 ASME Int. Mechanical Engineering Congress and Exhibition*, ASME FED 231, San Francisco, CA, USA, 1995.

Faghri, A., *Heat Pipe Science and Technology*, Washington, D.C.: Taylor & Francis, 1995.

Figus, C., Ounougha, L., Bonzom, P., Supper, W., and Puillet, C., Capillary fluid loop developments in Astrium, *Appl. Thermal Eng.*, vol. 23, pp. 1085–1098, 2003.

Jang, S. P. and Choi, S. U. S., Effects of various parameters on nanofluid thermal conductivity, *ASME J. Heat Transfer*, vol. 129, pp. 616–623, 2007.

Jentung, K., Overview of capillary pumped loop technology, in: ASME HED, vol. 236, *Heat Pipes and Capillary Pumped Loops*, pp. 1–17, 1993.

Kang, S. W., Wei, W. C., Tsai, S. H., and Yang, S. Y., Experimental investigation of silver nano-fluid on heat pipe thermal performance, *Appl. Thermal Eng.*, vol. 26, pp. 2377–2382, 2006.

Kim, S. J., Bang, I. C., Buongiorno, J., and Hu, L. W., Surface wettability change during pool boiling of nanofluids and its effect on critical heat flux, *Int. J. Heat Mass Transfer*, vol. 50, pp. 4105–4116, 2007.

Liu, Z. H., Xiong, J. G., and Bao, R., Boiling heat transfer characteristics of nanofluids in a flat heat pipe evaporator with micro-grooved heating surface, *Int. J. Multiphase Flow*, vol. 33, pp. 1284–1295, 2007a.

Liu, Z. H., Yang, X. F., and Guo, G. L., Effect of nanoparticles in nanofluid on thermal performance in a miniature thermosyphon, *J. Appl. Phys.*, vol. 102, pp. 013526.1–013526.8, 2007b.

Ma, H. B., Wilson, C., Borgmeyer, B., Park, K., Yu, Q., Choi, S. U. S., and Tirumala, M., Effect of nanofluid on the heat transport capability in an oscillating heat pipe, *Appl. Phys. Lett.*, vol. 128, pp. 143116.1–143116.3, 2006.

Maidanik, Yu. F., State-of-the-art of CPL and LHP technology, *Proc. 11th Int. Heat Pipe Conf.*, Tokyo, pp. 19–30, 1999.

Muraoka, I., Ramos, F. M., and Vlassov, V. V., Experimental and theoretical investigation of a capillary pumped loop with a porous element in the condenser, *Int. Comm. Heat Mass Transfer*, vol. 25, no. 8, pp. 1085–1094, 1998.

Pak, B. C. and Cho, Y. I., Hydrodynamic and heat transfer study of dispersed fluids with submicron metallic oxide particles, *Exp. Heat Transfer*, vol. 11, no. 2, pp. 151–170, 1998.

Stenger, F. J., *Experimental feasibility study of water-filled capillary-pumped heat-transfer loops*, NASA TM-X-1310, NASA Lewis Research Center, Cleveland, Ohio, 1966.

Triem, T. H., Jentung, K., Tamara, A., and O'Connell, Miniature loop heat pipes for electronic cooling, *Proc. Int. Electronic Packaging Technical Conference and Exhibition IPACK2003*, Maui, Hawaii, ASME Paper No.35245, 2003.

Tsai, C. Y., Chien, H. T., Ding, P. P., Chan, B., Luh, T. Y., and Chen, P. H., Effect of structural character of gold nano-particles in nanofluid on heat pipe thermal performance, *Mater. Lett.*, vol. 58, pp. 1461–1465, 2004.

Wei, W. C., Tsai, S. H., Yang, S. Y., and Kang, S. W., Effect of nanofluid concentration on heat pipe thermal performance, *IASME Trans.*, vol. 2, pp. 1432–1439, 2005.

Xue, H. S., Fan, J. R., Hu, Y. C., Hong, R. H., and Cen, K. F., The interface effect of carbon nanotube suspension on the thermal performance of a two-phase closed thermosyphon, *J. Appl. Phys.*, vol. 100, pp. 104909.1–104909.5, 2006.

Journal of Enhanced Heat Transfer, 17(4) 353–368 (2010)
Reprints available directly from the publisher.
Photocopying permitted by license only.

Numerical Behavior of Mixed Convection in a 2D Channel with a Co-Flowing Fluid Injection from a Flat Nozzle

A. MOKNI[1], H. MHIRI[1], G. LE PALEC[2*], & P. BOURNOT[2]

[a]Unité de Thermique et Environnement, Ecole Nationale d'Ingénieurs de Monastir, Route de Ouardanine 5000 Monastir, Tunisia
[b]IUSTI UMR CNRS 6595, Technopole de Chateau-Gombert, 5 rue Enrico Fermi, 13013 Marseille Cedex 20 — France

In this paper, a numerical investigation which concerns a mixed convection flow in a two-dimensional vertical heated channel is performed. This flow results from the mixing of the upgoing fluid along the channel walls with the one issued from a flat nozzle located at its entry section. The system of governing equations is solved with the finite volume method together with an implicit scheme. The obtained results prove the activation of heat transfer by the combined effect of turbulence and jet–wall interactions. This activation is also realized by the drive of ambient air by the jet.

Key words: channel; jet; mixed convection

*Corresponding author: G. Le Palec: georges.lepalec@univmed.fr

NOMENCLATURE

b	width of the nozzle, m
e	half-width of the channel, m
E	dimensionless rate of dissipation of turbulent kinetic energy
g	gravitational acceleration, $m \cdot s^{-2}$
Gr	Grashof number, $= \frac{g\beta\varphi H^4}{\nu^2\lambda}$
h	local heat transfer coefficient, $W \cdot m^{-2} \cdot K^{-1}$
H	length of the channel, m
k	turbulent kinetic energy, $m^2 \cdot s^{-2}$
K	dimensionless turbulent kinetic energy
M	dimensionless outlet mass flow rate: $M = 2Q_1 + Q_2$
Nu_x	local Nusselt number, $= \frac{hx}{\lambda}$
p	pressure, Pa
P	dimensionless pressure
P_g	dimensionless driving pressure
Pr	Prandtl number, $\frac{\mu c_p}{\lambda}$
Q_1	dimensionless mass flow rate at the inlet section of the channel
Q_2	dimensionless mass flow rate at the exit section of the nozzle
Ra	average Rayleigh number, $= \frac{g\beta H^4 \varphi}{\lambda\alpha\upsilon} = Gr \cdot Pr$
Re	Reynolds number, $= \frac{bu_0}{\upsilon}$
T	temperature, K
u, v	velocity components along the x and y axis, respectively, $m \cdot s^{-1}$
u_0	reference velocity
U, V	dimensionless velocity components along X and Y, respectively
x, y	coordinates, m
X, Y	dimensionless coordinates

Greek symbols

α	thermal diffusivity, $m^2 \cdot s^{-1}$
ε	rate of dissipation of turbulent kinetic energy, $m^2 \cdot s^{-3}$
φ	wall heat flux, $W \cdot m^{-2}$
λ	thermal conductivity, $W \cdot m^{-1} \cdot K^{-1}$
μ	dynamic viscosity, $kg \cdot m^{-1} \cdot s^{-1}$
ν	kinematic viscosity, $m^2 \cdot s^{-1}$
ρ	fluid density, $kg \cdot m^{-3}$
θ	dimensionless temperature

Subscripts

m	average
p	wall value
t	turbulent
x	local value
∞	external (ambient conditions value)

1. INTRODUCTION

In mechanical and environmental engineering, mixed turbulent convection is a frequently encountered thermal fluid phenomenon, which exists in atmospheric environment, urban canopy flows, ocean currents, gas turbines, heat exchangers, computer chip cooling systems, etc. When the first convective heat transfer studies were started, forced and natural convections were considered separately and the interaction between these two physical processes was ignored. The latest researches, that combine forced and natural convections, were initiated in the 1960's and were mainly based on experimental approaches (Metais and Eckert, 1964).

The most frequently used configuration in convection air cooling of electronic equipment is the two-dimensional channel formed by parallel plates. The latter is particularly attractive in applications relative to electronic devices due to the passive character of cooling by natural convection. However, researches for methods to improve the heat transfer are crucial in order to increase the cooling efficiencies (Bar-Cohen and Rosenow, 1984; Betts and Dafa'nela, 1986; Cheung and Sohn, 1989; Gebhart et al., 1987).

Heat transfer by natural convection from vertical plates with a uniform wall temperature or heat flux has received considerable attention, and extensive discussions about this subject are available in the literature.

Hugot (1972) undertook an experimental study of the interaction of the boundary layers developing along two large parallel vertical plates. This study allowed measuring the local heat transfer coefficients for various spacings and temperatures corresponding to Grashof numbers ranging from $5{\cdot}10^5$ to $2{\cdot}10^{11}$. The boundary layers interaction was defined by comparison with the single plate results. Moreover, information provided by the velocity, temperature profiles, and their fluctuations have led to a better knowledge of the turbulence of the flow.

Myamoto et al. (1986) studied experimentally turbulent natural convection flow and heat transfer in an asymmetrically heated vertical channel. The local velocity, the temperature values as well as heat transfer measurements were reported in their paper. Recently, Auletta and Manca (2002) carried out an experimental study on a channel-chimney system in order to elucidate the behavior of the fluid flow and the generated heat transfer. The channel is symmetrically heated and the chimney, located above the channel, is adiabatic. The presented results gave local measurements of the air temperature inside the channel and the adiabatic extension. Some correlations were proposed in order to connect the local Nusselt number to the Rayleigh number for several geometrical configurations and height-to-width ratios.

From a theoretical point of view, literature gives us extensive results for both turbulent and laminar flows. Turbulent heat transfer generated in a channel has been reported by Cheung and Sohn (1989), Korbut and Paladenko (1993), Fedorov and Viskanta (1997), and Versteegh and Nieuwstadt (1998, 1999). Fedorov and Viskanta (1997) proposed scaling correlations for induced flow rate and heat characteristics in an asymmetrically heated channel. Later Versteegh and Nieuwstadt (1998, 1999) also studied an asymmetrically heated channel in order to find wall functions from the scaling behavior of the flow. The authors treated this problem for laminar flows as well (Elenbas, 1942). The development of laminar buoyancy-driven convection between two vertical plane plates asymmetrically heated by a constant heat flux was studied by Dalbert et al. (1981) and Penot and Dalbert (1983). Desrayaud and Fichera (2002) undertook a numerical study of the laminar natural convection in an isothermal vertical channel in which rectangular ribs are symmetrically located on both walls. They studied the structure of the flow under different slot positions. Kheireddine et al. (1997) studied the influence of the pressure loss on the induced mass flux for a buoyancy-driven flow. The calculation domain was extended far from the channel, and they showed that the free pressure boundary location may be neglected if placed at a distance 4 times greater than the channel width. However both the theory (Ben Maad, 1979) and the experiments show that laminar and turbulent flows can take place simultaneously if the length of the plate is rather significant. The length of the transition region between the laminar and turbulent flows varies with the wall heat flux value.

For the sake of completeness, few studies focused on the mixed convection regime. Among these, we can cite that of Penot and Dalbert (1983) who proposed useful correlations to determine the flow rate, the fluid temperature, and the Nusselt number according to the heat-flux density, the pressure difference, and the dimensionless numbers Re and Gr. These correlations were proposed for favorable or unfavorable mixed convections. More recently, Najam et al. (2002) studied numerically the mixed convection in a T-shaped cavity heated with a constant heat flux and subjected to an air blast entering from the bottom. They showed the competition between natural and forced convections. The heat transfer was found to be maximal in the zone where the role of natural convection is more significant.

The present theoretical study is first concerned with natural convection in a heated vertical channel whose walls are submitted to a constant heat flux. The aim is to gain improved understanding of the flow evolution and to develop scaling relations for natural convection flow and heat transfer. Then, we combined both forms of convection in the heated channel, as a vertical jet of fresh air is injected from the bottom. The influence of this forced additional jet is analyzed by using the low Reynolds number k–ε turbulence model. Numerical results are reported for dry air as a coolant.

2. ASSUMPTIONS AND GOVERNING EQUATIONS

The geometry of the problem investigated herein is described in Fig. 1. We consider a vertical channel which simulates a chimney. A gas jet is issued from a flat nozzle located at the bottom of the channel. The chimney walls are subject to a constant heat flux which re-

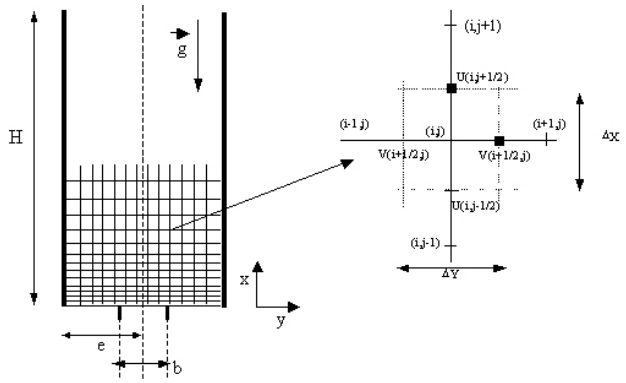

FIGURE 1. Flow configuration, system of coordinates and grid used.

sults in a mixed convection 2D flow when the nozzle operates. The flow is assumed to be steady and incompressible. Both the natural and mixed convection cases are considered by using the Boussinesq approximation in which the density linearly varies with the temperature. Other thermo-physical quantities are assumed to be constant. Let us introduce the dimensionless variables defined by:

$$X=\frac{x}{e};\quad Y=\frac{y}{e};\quad U=\frac{u}{u_0};\quad V=\frac{v}{v_0};$$

$$\frac{P=(p+\rho g x)e^2}{\rho\alpha^2};\quad \theta=\frac{T-T_\infty}{\varphi e}\lambda; \tag{1}$$

$$K=\frac{ke^2}{\alpha^2};\quad E=\frac{\varepsilon e^4}{\alpha^3}$$

The reference velocity is the velocity in the exit section of the nozzle for mixed convection and $u_0=(g\beta\phi e^2/\lambda)^{1/2}$ for free convection. The dimensionless governing equations for two-dimensional buoyancy-driven flows, with no viscous dissipation, can be written as follows:

Continuity equation:

$$\frac{\partial U}{\partial X}+\frac{\partial V}{\partial X}=0 \tag{2}$$

Momentum equation in X direction

$$U\frac{\partial U}{\partial X}+V\frac{\partial U}{\partial Y}=-\frac{\partial P}{\partial X}+(Pr+Pr_t)$$
$$\times\left[\frac{\partial^2 U}{\partial X^2}+\frac{\partial^2 U}{\partial Y^2}\right]-\frac{2}{3}\frac{\partial K}{\partial X}-Ra\,Pr\,\theta \tag{3}$$

Momentum equation in Y direction:

$$U\frac{\partial V}{\partial X}+V\frac{\partial V}{\partial Y}=-\frac{\partial P}{\partial Y}+(Pr+Pr_t)$$
$$\times\left[\frac{\partial^2 V}{\partial X^2}+\frac{\partial^2 V}{\partial Y^2}\right]-\frac{2}{3}\frac{\partial K}{\partial Y} \tag{4}$$

Energy equation:

$$U\frac{\partial\theta}{\partial X}+V\frac{\partial\theta}{\partial Y}=2\left[\frac{\partial^2\theta}{\partial X^2}+\frac{\partial^2\theta}{\partial Y^2}\right] \tag{5}$$

Turbulent kinetic energy equation:

$$U\frac{\partial K}{\partial X}+V\frac{\partial K}{\partial Y}=(Pr+\frac{Pr_t}{\sigma_k})$$
$$\times(\frac{\partial^2 K}{\partial X^2}+\frac{\partial^2 K}{\partial Y^2})-E+G_{DK}+G_{DB} \tag{6}$$

Rate of dissipation of the turbulent kinetic energy equation:

$$U\frac{\partial E}{\partial X}+V\frac{\partial E}{\partial Y}=(Pr+\frac{Pr_t}{\sigma_\varepsilon})$$
$$\times(\frac{\partial^2 E}{\partial X^2}+\frac{\partial^2 E}{\partial Y^2})-C_1\frac{E}{K}G_D+C_2\frac{E^2}{K} \tag{7}$$

where

$$G_{DK} = Pr_t\left(\frac{\partial U_i}{\partial X_j} + \frac{\partial U_j}{\partial X_i}\right)\frac{\partial U_i}{\partial X_j} - \frac{2}{3}K\delta_{ij}\frac{\partial U_i}{\partial X_j}$$

and

$$G_{DB} = \frac{1}{Fr}\frac{\nu_t}{Pr_t}\frac{\partial \theta}{\partial X} \tag{8}$$

E stands for the turbulent kinetic energy production due to shear, while G_{DK} is the turbulent kinetic energy production due to the mean velocity gradients, and G_{DB} is the turbulent kinetic energy production due to the buoyancy.

The standard k–ε model is used, so that constants are those given by Jones and Lauder (1973):

$$C_1 = 1.44;\quad C_2 = 1.92;\quad C_3 = 0.7;$$

$$C_\mu = 0.09;\quad \sigma_\varepsilon = 1.0;\quad \sigma_k = 1.30;\quad Pr_t = 1.0$$

The boundary conditions are the following:

where I_t is the turbulence intensity. The inlet mass flow rates Q_1 and Q_2 are defined by:

$$Q_1 = \int_{b/2e}^{1} U dY = \int_{-1}^{-b/2e} U dY$$

and

$$Q_2 = \int_{-b/2e}^{b/2e} U dY \tag{10}$$

where the reference velocity is now ν/e, in order to compare the results with a fixed reference mass flow rate when the Rayleigh number varies. The governing equations reported above are discretized on a staggered, nonuniform Cartesian grid using a finite volume procedure. In this method, for stability considerations, the scalar quantities P, θ, K, and E are calculated at the center (i, j) of the cells, whereas, the velocity components (U and V) are computed on the faces of the cells $(i, j \pm 1/2)$, $(i \pm 1/2, j)$ as shown in Fig. 1.

$$\left.\begin{aligned}
&\text{At } Y=-1;\quad U=0;\ V=0;\ \left(\frac{\partial\theta}{\partial Y}\right)_p = 1,\ K=0,\\
&\text{At } Y=1;\quad U=0;\ V=0;\ \left(\frac{\partial\theta}{\partial Y}\right)_p = 1,\ K=0,\\
&\text{At } X=0;\quad -1<Y<-\frac{b}{2e};\quad \frac{\partial U}{\partial X}=0,\ V=0,\ P_g=-\frac{Q_1^{\,2}}{2},\ \theta=0,\ K=\frac{3}{2}I_tU^2,\ E=\frac{2eK^{0.5}}{b}\\
&\qquad -\frac{b}{2e}<Y<\frac{b}{2e};\quad \text{For free convection :}\\
&\qquad\qquad \frac{\partial U}{\partial X}=0,\ V=0,\ P_g=-\frac{Q_2^{\,2}}{2},\ \theta=0,\ K=\frac{3}{2}I_tU^2,\quad E=\frac{2eK^{0.5}}{b}\\
&\qquad\qquad \text{For mixed convection (presence of the jet) :}\\
&\qquad\qquad U=1,\ V=0,\ \theta=0,\ K=0.001\,U,\quad E=\frac{2eK^{0.5}}{b}\\
&\qquad \frac{b}{2e}<Y<1;\quad \frac{\partial U}{\partial X}=0,\ V=0,\ P_g=-\frac{Q_1^{\,2}}{2},\ \theta=0,\ K=\frac{3}{2}I_tU^2,\ E=\frac{2eK^{0.5}}{b}\\
&\text{At } X=\frac{H}{e};\quad \frac{\partial U}{\partial X}=\frac{\partial V}{\partial X}=\frac{\partial\theta}{\partial X}=0,\ P_g=0,\ K=\frac{3}{2}I_tU^2,\ E=\frac{2eK^{0.5}}{b}
\end{aligned}\right\} \tag{9}$$

3. RESULTS AND DISCUSSION

For the sake of validation, the computations were performed first for a simple channel, i.e., without gas injection from the nozzle, then the numerical results were compared with the experimental ones published by Auletta ans Manca (2002) (Fig. 2). The resulting free convection problem was simulated with H/e = 5 and φ = 450 W, which corresponds to a Rayleigh number equivalent to $1.16 \cdot 10^7$. The Prandtl number is 0.71 (air). The results show the variation of the dimensionless temperature from the axis to the channel wall, for X = 2.5 and X = 4.75. Differences between measurements and numerical predictions are very low and they mainly concern the middle of the channel (X = 2.5) where experimental wall temperature values are slightly higher than the calculated ones. This may be due to the fact that there were some heat losses caused by insufficient thermal insulation in the experiments, as reported by Cheesewright et al. (1986). Moreover, the imposed wall heat flux was not uniform because of the space between two successive heaters. At least, the use of thermocouples also modifies the flow structure, especially in the vicinity of the plates. All this explains that discrepancies are higher near the wall.

In order to quantify in a better way the total heat exchange between the channel and the flow, let us study the evolution of the average Nusselt number defined as:

$$\mathrm{Nu}_m = \overline{\mathrm{Nu}} = \frac{\overline{h} H}{\lambda}$$

where

$$\overline{h} = \frac{1}{H}\int_0^H h_x dx = \frac{1}{H}\int_0^H \frac{\phi}{T_p - T_\infty} dx \qquad (11)$$

We notice that the average Nusselt number increases with the Rayleigh number (Fig. 3): both of them are well correlated by the two following relationships:

For lowest Rayleigh numbers:

$$Nu_m = 3.38 \cdot 10^{-6}\, Ra^{0.889} \mathrm{Pr}^{0.33} \qquad (12)$$

For higher Rayleigh numbers (turbulent flow):

$$Nu_m = 5.01\, Ra^{0.284} \mathrm{Pr}^{0.33} \qquad (13)$$

Figure 4 presents the mass flow rate evolution in the outlet section, according to the Rayleigh number. Note that the maximum calculated deviation is 0.04% between the inlet and outlet openings of the channel. As the Nusselt number, the mass flow rate increases with the Rayleigh number, except in the range $5 \cdot 10^{10} < \mathrm{Ra} < 2 \cdot 10^{11}$. For low values of the wall heat flux, i.e., low Rayleigh numbers, the thickness of the boundary layers growing up along each plate is large enough so that layers merge on the axis, before reaching the exit section of the channel. For $\mathrm{Ra} \approx 5 \cdot 10^{10}$, the boundary

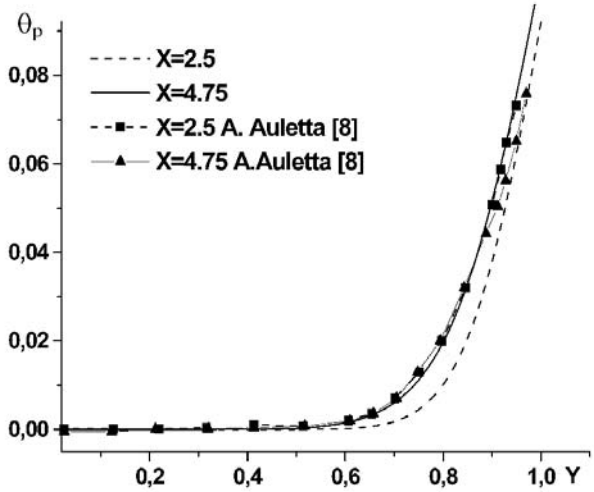

FIGURE 2. Temperature profiles for the configuration with H/e = 2.5 and Φ = 450 W. Comparison with the experiments by Auletta and Manca (2002).

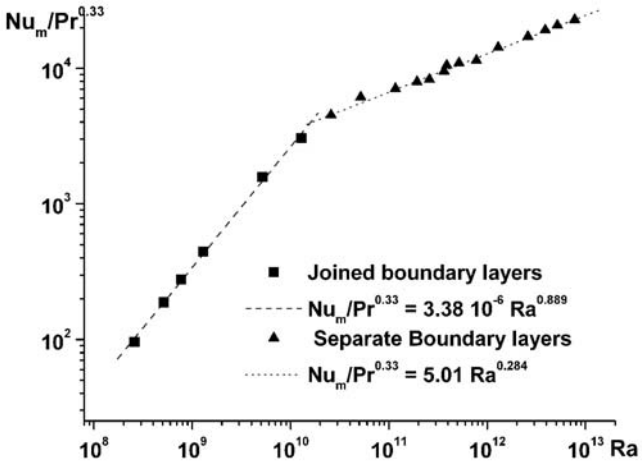

FIGURE 3. Mean Nusselt number variation with Ra.

layers are thinner and they separate before the exit section as the Rayleigh number increases. This fact results in a decrease of the mean flow rate since the x velocity component is progressively decreasing at the center of the channel. The thickness of the boundary layers continues to decrease symmetrically with an increasing x velocity gradient on each plate, whereas the velocity in the central region tends towards zero. The channel then tends to behave like two independent single parallel plates. For Ra > $2{\cdot}10^{11}$, the effect of the velocity increasing in the boundary layers becomes dominating in front of the reduction of the boundary layer thicknesses at the exit section, and the drive of the ambient fluid is so high that it now dominates the trajectory of the flow on the axis of the channel. This explains the observed minimum that is followed by a continual growth in the turbulent region. The above description of the flow behavior also explains the change in the slope of Nusselt correlations shown in Fig. 3.

In order to increase the cooling efficiency, combined forced and free convections are now studied by adding a vertical jet of fresh air entering from the bottom of the channel. The jet is issued from a flat nozzle located on the channel axis, as shown in Fig. 1.

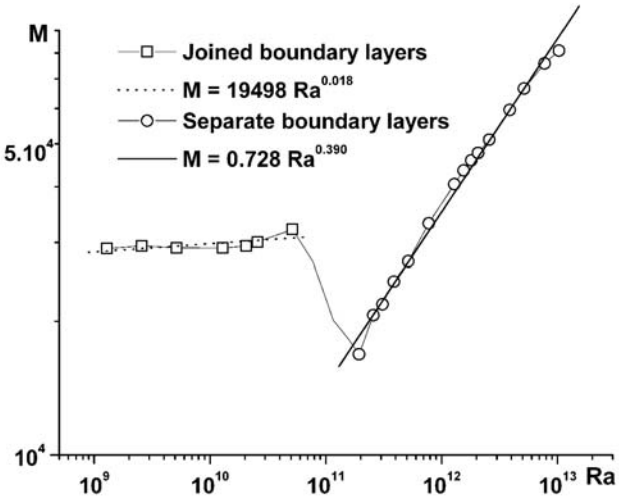

FIGURE 4. Mass flow rate variation with Ra.

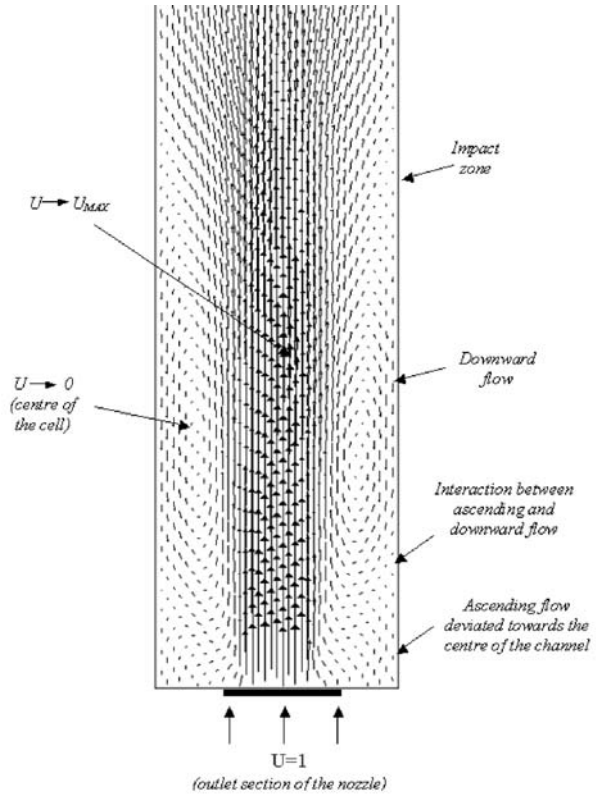

FIGURE 5. Behavior of the flow near the nozzle exit section for the mixed convection case: Re = 1000, Ra = $1.28 \cdot 10^{12}$.

The jet involves all the fluid located in the entry area of the channel in an ascending flow. When it interacts with the walls, the jet separates in an ascending flow and a downward flow, the latter is weak since the angle of impact is small. The downward flow creates a rotating cell between the wall and the jet flow. If the width ($2e$) of the channel and/or if the jet velocity are low, the center of this cell is located close to the entry section, so that an outflow is likely to develop through the entry section along the walls and an upward flow is created in the vicinity of the nozzle, due to the drive of ambient fluid by the jet. When the Reynolds number increases, the point of impact between the jet and the walls moves away from the nozzle and involves the cell whose size increases, all the fluid located in entry section being driven in an ascending flow.

When the heat transfer is generated, natural convection induces along the walls an upward flow which opposes to the downward flow resulting from the impact of the jet. Because of the space occupied by the cell, the ascending flow tends then to being deviated towards the center of the channel, which results in a slight contraction of the jet and, consequently a low acceleration in the axial area. This is shown in Fig. 5 where only the flow in the bottom part of the channel has been represented.

Taking into account this characteristic, we propose to consider in the following the mixed convection phenomenon.

The mass-flow rate at the entry section of the channel ($-1 < Y < -b/2e$; $b/2e < Y < 1$) was evaluated for different Reynolds numbers. When Re > 5000 and for the same imposed heat flux (i.e., constant Rayleigh number), it increases linearly according to the Reynolds number. This can be seen in Fig. 6 and may be expressed in the following correlation:

$$2Q_1 = -15{,}580 + 19.4\mathrm{Re} \tag{14}$$

For low Reynolds numbers (Re < 5000), mixed convection is observed in the entry section. However, as the velocity of the fluid issued from the nozzle increases, the flow is mainly led by the drive caused by the jet, which explains that natural convection does not have an influence anymore.

We examine at present the heat transferred along the walls, the developed flow structures, and temperature fields for $\mathrm{Ra} = 2.57 \cdot 10^{10}$, $H/e = 25$, $b/e = 0.5$, and Reynolds number ranging from 0 (i.e., free convection) to $2 \cdot 10^4$. The flow structure and the thermal field are presented by means of streamlines and isotherms, respectively. For Re = 0, natural convection is developed along the channel because of the temperature gradient between the fluid and the heated walls (Fig. 7a). This thermal drive generates a vertical aspiration of air with a significant mass flow rate at the outlet section of the channel. So, in order to examine the mixed convection cases (Figs. 7b–7d), we considered Re values up to 10^3, the structures induced by the jet being negligible under this value since the natural convection dominates. For $\mathrm{Re} = 10^3$ (Fig. 7b), $\mathrm{Re} = 3 \cdot 10^3$ (Fig. 7c), and $\mathrm{Re} = 2 \cdot 10^4$ (Fig. 7d) we can see that the jet widens and symmetrically impacts the walls, which induces the downward flow along both walls. Opposed to the upward flow (generated by buoyancy forces), the downward flow is deviated towards the axial region, which results in a low accel-

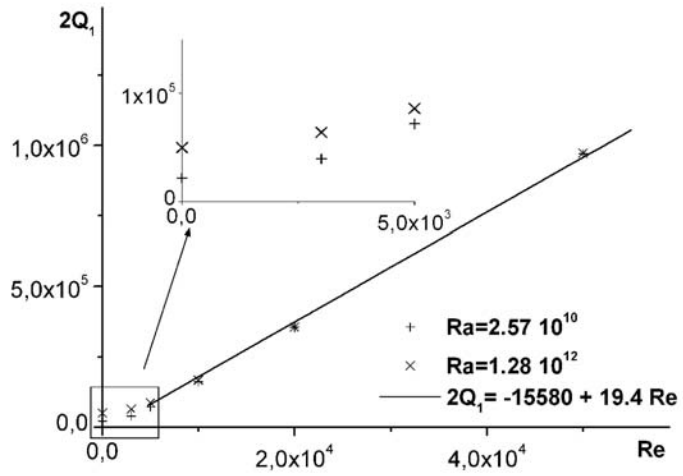

FIGURE 6. Natural convection flow rate according to the Reynolds number.

TABLE 1: Maximal Dimensionless Temperature of the Wall, *H/e* = 25, *b/e* = 0.5

	Re = 0		Re = 1000		Re = 3000		Re = 20,000	
Ra	θ_{MIN}	θ_{MAX}	θ_{MIN}	θ_{MAX}	θ_{MIN}	θ_{MAX}	θ_{MIN}	θ_{MAX}
$2.57 \cdot 10^{9}$	0	1.62697	0	1.57125	0	1.49326	0	1.44897
$2.57 \cdot 10^{10}$	0	0.35475	0	0.272	0	0.2215	0	0.16475
$1.28 \cdot 10^{12}$	0	0.11875	0	0.1095	0	0.0715	0	0.01908
$5.15 \cdot 10^{12}$	0	0.07946	0	0.07794	0	0.06775	0	0.01692

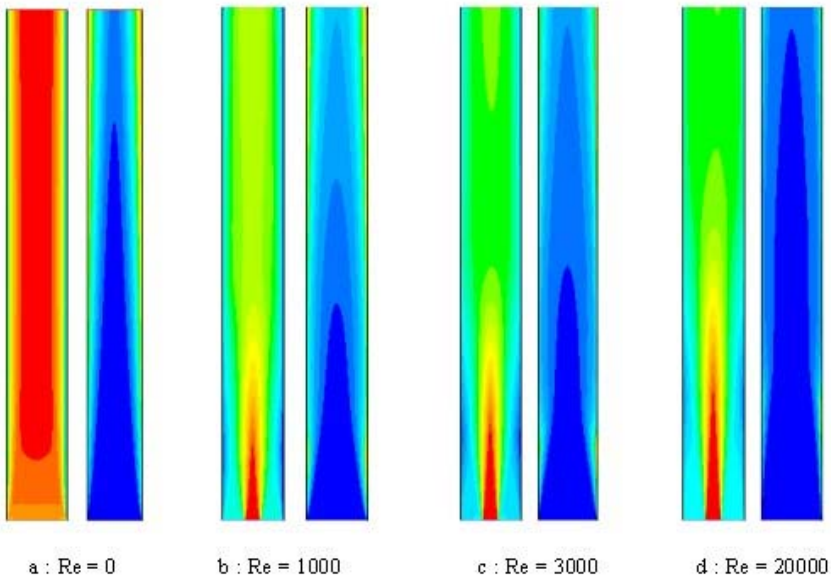

FIGURE 7. Velocity magnitude and isotherms for several Reynolds numbers and Ra = $2.57 \cdot 10^{10}$.

eration at the center of the channel. As the Reynolds number increases, the jet interacts with the walls more significantly far from the nozzle. We notify that the existence of the cells is undesirable because it minimizes the heat exchange through the wall and generates hot zones, as it can be seen from isotherms presented in Figs. 7b, 7c, and 7d. However, the size of this region is small and the overall cooling is higher with an additional jet, the maximal temperature of the wall decreasing with an increasing Reynolds number, as reported in Table 1, for all the Rayleigh number considered.

For ascending Reynolds numbers, the forced convection within the channel results in a thinner thermal boundary layer along both walls, lower dimensionless wall temperatures are consequently observed. This is shown on the profiles reported in Fig. 8. For each profile, we notice that the temperature highly decreases at the vicinity of the impact zone and it re-increases farther. For Re = 1000 and $1 < X < 3.5$, the wall temperature is higher than the one obtained with pure free convection, which means that the heat transfer is worse in this region: this is the consequence of the interaction between the ascending and the downward flows near the walls. This effect no longer appears for higher values of the jet flow velocity because forced convection becomes dominating. This fact confirms that Reynolds numbers with values less than 1000 are practically out of interest.

Figure 9 represents the corresponding local Nusselt numbers, that is the ratio $X/\theta_p(X)$. We note that an increase of the inlet Reynolds number generates a more intense heat exchange. This result was awaited because the higher is the velocity of the fresh air blast, the higher is the heat removed from the channel. Due to a decrease of the boundary layer thickness for increasing jet Reynolds number, the temperature gradient grows and, consequently, the Nusselt number is higher. We also observe that the Nusselt number increases with the X distance for all the inlet conditions tested. However the additional forced flow influence is more noticeable for high Rayleigh numbers. For low Rayleigh numbers ($Ra = 2.57 \cdot 10^9$), a small velocity flow at the nozzle is enough to extract the heat from the walls. So, a significant flow no longer affects the heat transfer between the fluid and the plate, as observed in Fig. 10. For significant Rayleigh numbers ($1.28 \cdot 10^{12}$) the heat transfer is all the more significant since the Reynolds number of the jet flow is high (Fig. 11).

In the following sections, the heat transfer along the walls and temperature fields are examined for the Rayleigh number varying from $2.57 \cdot 10^9$ to $1.28 \cdot 10^{12}$ and fixed Reynolds numbers. Because the natural convection becomes very intense for high values of Ra, it is necessary to apply a very powerful jet to dominate it and to observe the forced convection mode; that is why we adopted the following values: $Re = 10^3$ and $Re = 2 \cdot 10^4$.

For $Re = 3 \cdot 10^3$, the effect of the Rayleigh number on isotherms is shown in Figs. 12a–12c. It can be seen that as Ra increases, the temperature of the fluid inside

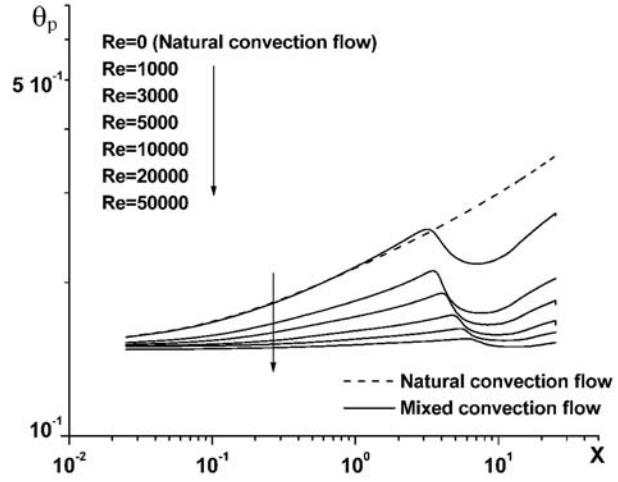

FIGURE 8. Variation of local wall temperatures: $Ra = 2.57 \cdot 10^{10}$, $H/e = 25$, and $b/e = 0.5$.

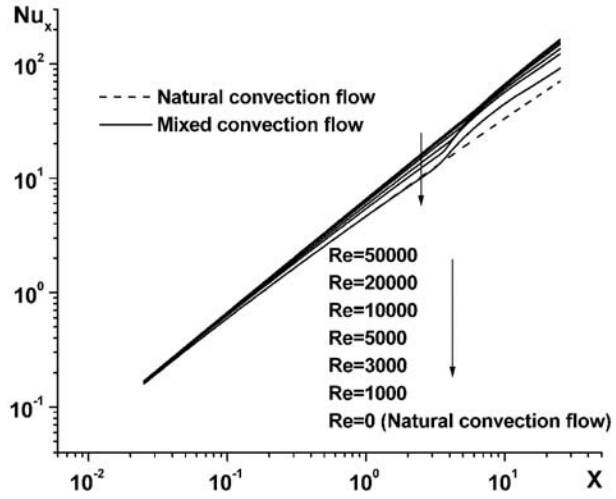

FIGURE 9. Variation of the local Nusselt number: Ra = $2.57 \cdot 10^{10}$, *H*/*e* = 25, and *b*/*e* = 0.5.

the channel increases and as a result the hot fluid rises like a buoyant plume into the outside domain. This action is referred to as the ejection mechanism (Vafai and Ettefagh, 1990) caused by the convection heat transfer interaction within the channel. Due to the additional natural convection flow with a non-negligible mass flow rate, the vertical ascending flow is more important for high Rayleigh numbers and the jet flow interacts with the walls more significantly far from the nozzle. Therefore, the cold air of the surrounding region penetrates more rapidly in the lower part of the channel in order to replace the leaving hot fluid and to ensure the mass flow rate conservation. This mechanism is responsible for an almost parallel flow along the walls of the channel. For a higher Rayleigh number, the thickness of the thermal boundary layer decreases and consequently increases the effectiveness of the heat transfer within the channel as well as with the far field fluid as observed in Fig. 13. This figure also shows that for low Reynolds numbers, the natural con-

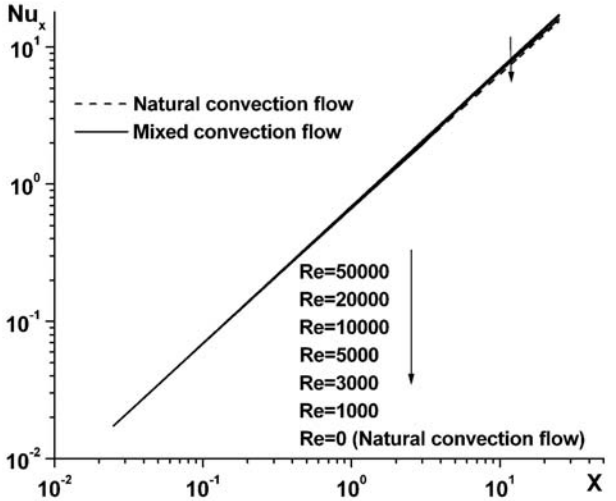

FIGURE 10. Variation of the local Nusselt number: Ra = $2.57 \cdot 10^{9}$, *H*/*e* = 25, and *b*/*e* = 0.5.

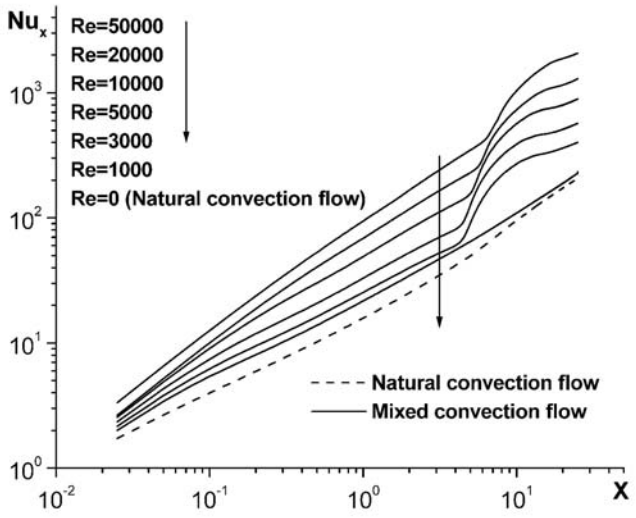

FIGURE 11. Variation of the local Nusselt number: Ra = $1.28 \cdot 10^{12}$, *H*/*e* = 25, and *b*/*e* = 0.5.

vection flow rate is important compared to the forced convection one since the impact zone location raises according to the Rayleigh number.

Figure 14 illustrates the influence of an increase in the Reynolds number of the external flow (Re = $2 \cdot 10^4$). For a higher Reynolds number, the flow field is mainly controlled by the jet. For the three cases, the flow penetration into the channel is almost the same due to the predominant effect of the forced convection flow. As a result, as seen from the figure, isotherms are clustered at the walls due to a high-speed external flow passing over the open cavity. The high speed of the jet flow enhances the heat transfer within the wall.

Figure 15 presents the longitudinal evolution of the local Nusselt number for various Rayleigh numbers and Re = $2 \cdot 10^4$. The influence of the jet on the Nusselt

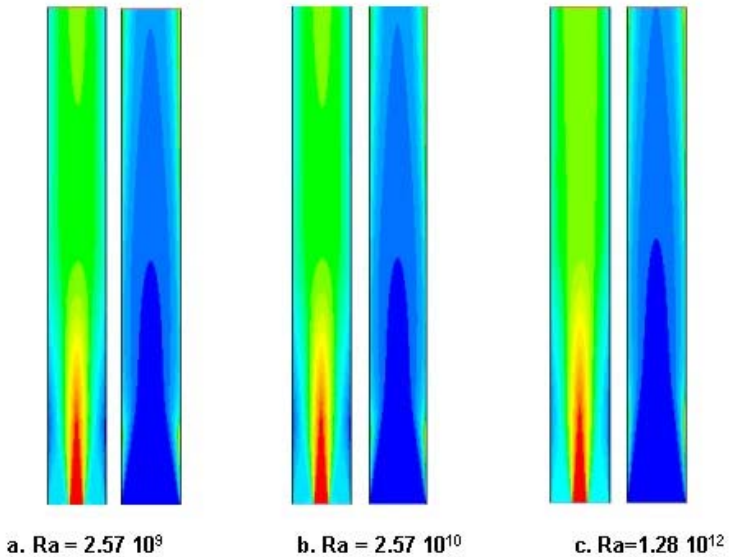

FIGURE 12. Velocity magnitude and isotherms for several Rayleigh numbers: Re = $3 \cdot 10^3$ and Re = $20 \cdot 10^3$.

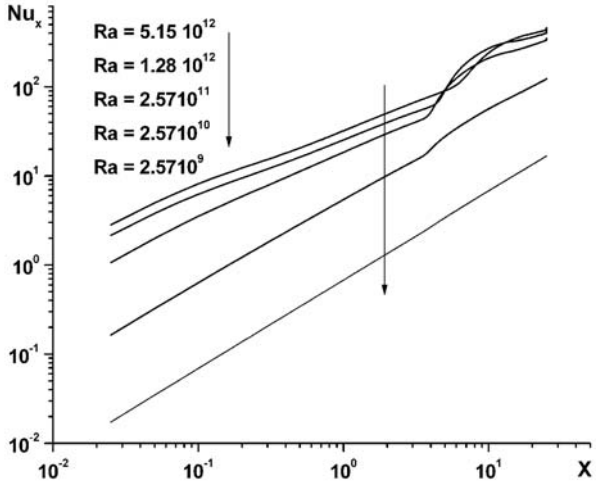

FIGURE 13. Variation of the local Nusselt number: Re = $3{\cdot}10^3$, *H*/*e* = 25, and *b*/e = 0.5.

number profile is particularly noticeable for important Rayleigh numbers, because a higher wall heat flux yields a more significant variation of the wall temperatures, mainly in the region where the jet interacts with the wall. Only in the lower part of this zone, the recirculation flow minimizes the heat exchange. Note that the quasi-linear shape of the Nusselt number profile for the lowest Rayleigh numbers tested (Ra = $2.57{\cdot}10^9$ and Ra = $2.57{\cdot}10^{10}$) is a consequence of the weak wall temperature variation.

Finally, Fig. 16 shows the evolution of the average Nusselt number according to the Reynolds number, for average Rayleigh numbers ranging between Ra = $2.6{\cdot}10^{10}$ and Ra = $1.3{\cdot}10^{13}$. The average Nusselt number increases according to the Reynolds number; which is explained by the fact that the thickness of the boundary layer, which acts as a heat insulator, decreases when the Reynolds number increases. The convective exchange between the flow and the heated plates hence increases. For high Rayleigh numbers (up

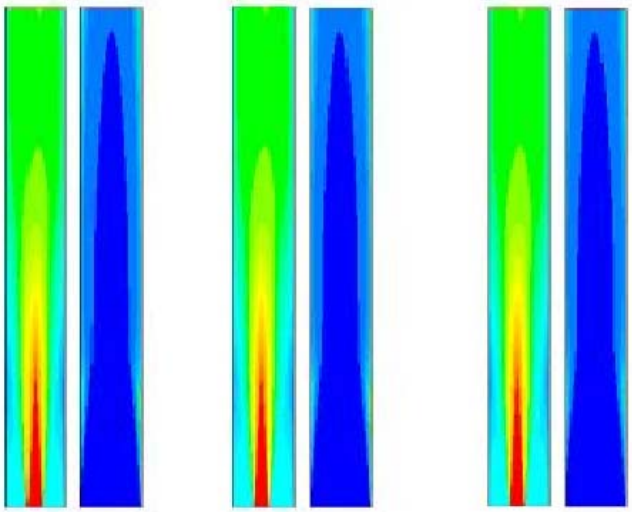

a. Re = 2.57 10^9 b. Ra = 2.57 10^{10} c. Ra = 1.28 10^{11}

FIGURE 14. Velocity magnitude (left) and isotherms (right) for several Rayleigh number and Re = $20{\cdot}10^4$.

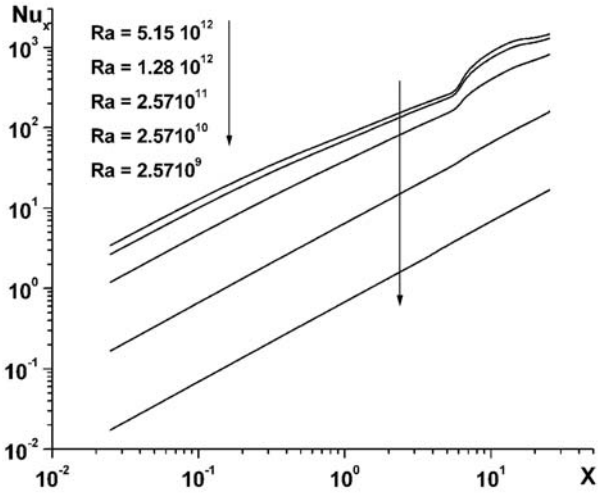

FIGURE 15. Variation of the local Nusselt number: Re = $20{\cdot}10^3$, *H*/*e* = 25, and *b*/*e* = 0.5.

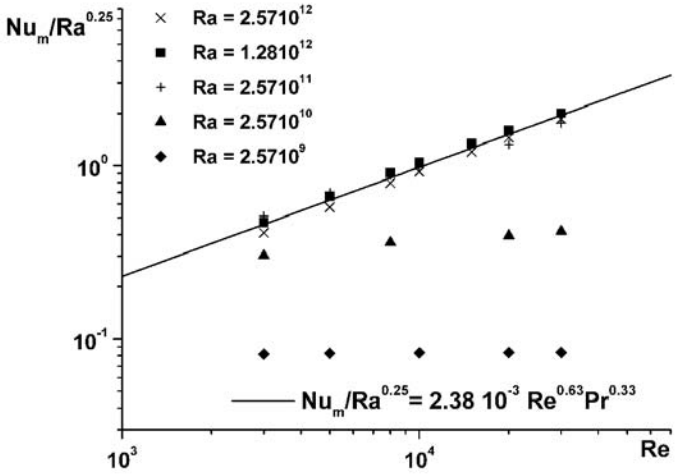

FIGURE 16. Average Nusselt number vs Re.

to $2.6{\cdot}10^{11}$), all these profiles merge and can then be correlated, according to:

$$Nu_m = 2.3810^{-3}\mathrm{Re}^{0.63}\mathrm{Pr}^{0.63}\mathrm{Ra}^{0.25} \qquad (15)$$

4. CONCLUSIONS

A numerical study of both the natural and mixed convection in a 2D channel submitted to a constant wall heat flux was performed. The mixed flow is obtained by using an ascending jet located in the entry section of the channel. The numerical procedure was validated by comparing our results with the experimental data of Auletta and Manca (2002). Special attention was dedicated to the thermal behavior of the flow, especially in the jet–wall interaction zone. The effects of a wide range of pertinent parameters such as the Rayleigh number and the jet flow Reynolds number have been investigated.

The vertical jet permits good ventilation at the entrance of the channel and enhances then the heat exchanges from the channel towards the exterior. It was shown that for high Reynolds numbers, the flow field is mainly controlled by the external flow. An increase in the Rayleigh number leads to the increase of the effectiveness of the heat transfer for all ranges of Reynolds numbers. For Re = $3{\cdot}10^3$, both convection modes coexist. For Re = $2{\cdot}10^4$, the jet flow is very powerful, the natural convection flow is overwhelmed, and the forced convection mode is observed. Some correlations connecting the average Nusselt number with the modified Rayleigh number were also proposed.

REFERENCES

Auletta, A. and Manca, O., Heat and fluid flow resulting from the chimney effect in a symmetrically heated vertical channel with adiabatic extensions, *Int. J. Thermal Sci.*, vol. 41, pp. 1101–1111, 2002.

Bar-Cohen, A. and Rohsenow, W. M., Thermally optimum spacing of vertical natural convection cooled parallel plates, *J. Heat Transfer*, vol. 106, pp. 116–123, 1984.

Ben Maad, R., Convection naturelle en mur plan à des nombres de Prandtl elevés, Ph.D. Thesis, University of Pierre et Marie Curie, Paris VI, 1979.

Betts, P. L. and Dafa'nela, A. A., Turbulent buoyant air flow in a tall rectangular cavity, *ASME HTD 60*, p. 83, New York: ASME, 1986.

Cheeseweright, R., King, K. J., and Ziai, S., Experimental data for the validation of computer codes for the prediction of two dimensional buoyancy cavity flows, *Winter Annual Meeting, ASME HTD 60*, pp. 75–80, 1986.

Cheung, F. B. and Sohn, D. Y., Numerical study of turbulent natural convection in an innovative air cooling system, *Numer. Heat Transfer*, Part A, vol. 16, pp. 467–487, 1989.

Dalbert, A. M., Penot, F., and Peube, J. L., Convection naturelle laminaire dans un canal vertical chauffé á flux constant, *Int. J. Heat Mass Transfer*, vol. 24, no. 9, pp. 1463-1473, 1981.

Desrayaud, G. and Fichera, A., Laminar natural convection in a vertical isothermal channel with symmetric surface-mounted rectangular ribs, *Int. J. Heat Fluid Flow*, vol. 23, pp. 519–529, 2002.

Elenbas, W., Heat dissipation of parallel plates by free convection, *Physica*, vol. 9, pp. 1–28, 1942.

Fedorov, A. G. and Viskanta, R., Turbulent natural convection heat transfer in an asymmetrically heated vertical parallel plate channel, *Int. J. Heat Mass Transfer*, vol. 40, no. 16, pp. 3849–3860, 1997.

Gebhart, B., Jaluria, Y., Mahajana, R. L., and Summakia, B., *Buoyancy-Induced Flows and Transport*, Washington, DC: Hemisphere, 1987.

Hugot, G., Etude de la convection naturelle laminaire entre deux plaques planes verticales parallèles et isothermes, *Entropie*, vol. 46, pp. 55–66, 1972.

Jones, W. P. and Launder, B. E., The calculation of the low Reynolds number phenomena with a two-equation model of turbulence, *Int. J. Heat Mass Transfer*, vol. 16, pp. 1119–1130, 1973.

Kheireddine, A. S., Houla Sanda, M., Chaturvedi, S. K., and Mohieldin, T. O., Numerical prediction of pressure loss coefficient and induced mass flux for laminar natural convective flow in a vertical channel, *Energy*, vol. 22, no. 4, pp. 413–423, 1997.

Korbut, V. P. and Paladenko, Yu. V., Turbulent natural convection flow and heat transfer in a flat vertical slot with asymmetrically heated walls, *Heat Transfer Res.*, vol. 25, pp. 313–320, 1993.

Metais, B. and Eckert, E. R. G., Forced, mixed and free convection regimes, *J. Heat Transfer*, vol. 86, pp. 295–296, 1964.

Miyamoto, M., Katoh, Y., Kurima, J., and Saki, H., Turbulent free convection heat transfer from vertical parallel plates, in C. L. Tien, V. P. Carey, and J. K. Ferrell, Eds., *Heat Transfer*, vol. 4, Washington, DC: Hemisphere, pp. 1593–1598, 1986.

Najam, M., El Almi, M., Hasnaoui, M., and Amahamid, A., Etude numérique de la convection mixte dans une cavité en forme de T soumis à un flux de chaleur constant et ventilé par le bas à l'aide d' un jet d'air vertical, *Compte Rendu de Mécanique*, vol. 330, pp. 461–467, 2002.

Penot, F. and Dalbert, A. M., Convection naturelle mixte et forcée dans un thermosiphon vertical chauffé à flux constant, *Int. J. Heat Mass Transfer*, vol. 26, no. 11, pp. 1639–1647, 1983.

Vafai, K. and Ettefagh, J., The effects of sharp corners on buoyancy-driven flows with particular emphasis on outer boundaries, *Int. J. Heat Mass Transfer*, vol. 33, pp. 2311–2328, 1990.

Versteegh, T. A. M. and Nieuwstadt, F. T. M., A direct numerical simulation of natural convection between two infinite vertical differentially heated walls scaling laws and wall functions, *Int. J. Heat Mass Transfer*, vol. 42, pp. 3673–3693, 1999.

Versteegh, T. A. M. and Nieuwstadt, F. T. M., Turbulent budgets of natural convection in an infinite, differentially heated, vertical channel, *Int. J. Heat Fluid Flow*, vol. 19, pp. 135–149, 1998.

Journal of Enhanced Heat Transfer, 17(4) 369–380 (2010)
Reprints available directly from the publisher.
Photocopying permitted by license only.

Motion and Heat-Transfer Analysis of a Closed-Loop Oscillating Heat Pipe with a Magnetic Field

K. WONGKASEM, S. RITTIDECH,* & B. BUBPHACHOT

Heat Pipe and Thermal Tools Design Research Lab. (HTDR), Faculty of Engineering, Mahasarakham University, 41/20 Khamriang Sub-District, Kantarawichai District, Mahasarakham 44150, Thailand

A mathematical model to predict the oscillating motion and heat transfer in a closed-loop oscillating heat pipe in the presence of a magnetic field is presented. Theoretical analysis is used to study the effect of a magnetic field on the motion of vapor bubbles and a liquid slug. The magnetic field is assumed to produce constant field strength in the transverse direction through the evaporating section. The magnetohydrodynamics (MHD) theory is conducted to investigate the driving force due to the oscillating motion. The proposed model investigates the effect of the magnetic field on forced convection. This study employs the theory of boiling heat transfer to determine the heat-transfer coefficients. This model also investigates several parameters such as a type of fluid (water and salt water), magnetic field strength, operating temperature, and dimension of the oscillating heat pipe. This study concludes that magnetic field increases the oscillating motion and can also raise the heat-transfer rate. The oscillating heat-pipe efficiency is enhanced by 8%.

Key words: oscillating heat pipe, magnetic field, magnetic fluid

*Corresponding author: S. Rittidech rittidej@hotmail.com

NOMENCLATURE

A	cross-sectional area, m^2	ω	frequency, rad/s
B	magnetic field strength $N/A \cdot m^2$, T	ζ	damping ratio [–]
C	specific heat, $J/kg \cdot {}^oC$	μ_r	relative magnetic permeability, N/A^2
D	diameter, m	μ_0	fluid permeability, N/A^2
F	force, N	σ	electrical conductivity, semen/m
G	mass flux, $kg/s \cdot m^2$	σ_t	surface tension, N/m
H	magnetic field intensity, A/m	**Subscripts**	
h	heat-transfer coefficient, $W/cm^2 \cdot {}^oC$	a	ambient
h_{fg}	latent heat of evaporation, kJ/kg	c	condensing, condenser
J	current density [–]	ca	condenser to ambient
k	thermal conductivity, $W/m \cdot {}^oC$	cv	convection
L	length, m	cw	cold water
m	mass flow rate, kg/s	d	driving
P	perimeter, m	e	evaporating, evaporator
P	pressure, N/m^2	ea	evaporator to ambient
Pr	Prandtl number [–]	f	fluid
Q	heat, W	h	hydraulic
R	thermal resistance [–]	hp	heat pipe
R	gas constant, $J/kg \cdot {}^oK$	hw	hot water
Re	Reynolds number [–]	i	in
S	suppression factor [–]	l	liquid
T	temperature, ^oC	mag	magnetic
t	time, s	NB	nucleate boiling
u	velocity, cm/s	o	out
x	coordinate, m	sat	saturated
X_{tt}	Martinelli parameter [–]	tp	two-phase
Greek symbols		tt	total
ν	viscosity, $(N \cdot s/m^2)$	v	vapor
ρ	density, kg/m^3	w	wall

1. INTRODUCTION

An oscillating heat pipe is a new type of two-phase heat-transfer devices. An oscillating heat pipe can be utilized in many ways such as a heat recovery system, a cooling system of electronics parts, an air pre-heater system, and a solar collector. This equipment provides high efficiency in heat transfer. The advantage of using an oscillating heat pipe over the conventional methods is that large quantities of heat can be transported through a small cross-sectional area with no additional power input to the system. Heat transfer relies on an oscillatory flow of a liquid slug and vapor bubbles in a long miniature tube which is bended into many turns. The oscillating heat pipe is filled by working fluid. Heat is added in the evaporating region, liquid is then vaporized causing the vapor volume expansion. Simultaneously, vapor in the condensing region is condensed into the liquid state causing volume contraction. As a result, the oscillating motion of the liquid slugs and vapor bubbles in the heat pipe occurs. Rittidech et al. (2003) stated that an oscillating heat pipe can be designed in at least three ways: (i) open-loop system, (ii) closed-loop system, and (iii) closed-loop system with an additional check valve.

A lot of research studies were carried out both experimentally and analytically due to the complicated behavior of working fluid in an oscillating heat pipe.

The experimental investigation focuses mainly on the visualization of a flow pattern and the measurement of temperature and heat-transfer rate. Ma et al. (2006) proposed a theoretical model to study the motion of liquid slug and vapor bubbles by the temperature difference between hot and cold sections. Different working fluids were compared on both phase and frequency of the oscillating motion. Liang and Ma (2004) created another model using Newton's second law to find a force that influences the motion of liquid and vapor. Zhang and Faghri (2003) analyzed a model of an open-loop oscillating heat pipe by the laws of mass, momentum, and energy conservation, and used an implicit finite-difference method to find velocity and pressure of liquid and vapor. Shafi and Faghri (2002) created a model of a single-loop oscillating heat pipe. There are liquid in a cooling section and vapor in a heating section. The explicit finite-difference method by a unit step function was used to find heat transfer from the evaporating section to the condensing section.

A magnetic field was used in an active technique to enhance the heat-transfer rate of a conventional heat pipe. Magnetic field and magnetic fluid were applied in conventional heat pipes; however, it is rarely found in oscillating heat pipes. Typically, magnetohydrodynamics is present when the working fluid flows through a magnetic field. The induced current is formed. It produces force and energy on the working fluid. This force and energy can increase the motion and the heat-transfer rate. Therefore, this is a good way to enhance the heat transfer of an oscillating heat pipe. In the conventional heat pipe proposed by Jeyadevan and Natkasuka (2004), permanent magnets are installed on both sides of a vertical heat pipe in the evaporating section. Both the distance and angle of permanent magnets are adjusted to measure the heat-transfer rate. These permanent magnets can be maximized to 13% of their efficiency. Elizbieta et al. (2005) studied the effect of the magnetic field in a perpendicular direction on a vertical heat pipe by flow visualization. It was found that a strong magnetic field can induce convection flow and enhance the heat-transfer rate. Ji and Gardner (1997) studied the effect of the magnetic field in the transverse direction of a flow pattern on the other side of a horizontal heat pipe. When the magnetic field strength is increased, the turbulence changes to laminar. Feng et al. (2005) investigated the effect of the magnetic field on a liquid–gas annular flow. The experiment showed that a magnetic field in transverse direction could produce vapor bubbles along the core direction. The application of a magnetic field to enhance the heat-transfer and air-flow rate in a heat pipe was studied by Shu et al. (2003). The finite-volume technique was applied to computation methods. It was found that the strength of a magnetic field and the temperature difference between a pipe wall and inlet can induce strong radial velocity. They can also increase both volume flow rate and Nusselt number to be more than twice.

A magnetic field affects the motion and heat transfer of an oscillating heat pipe, when electrical conductivity and magnetic permeability of working fluid are high. Water, ethanol, and R22 are usually used to fill in an oscillating heat pipe but they have low values of electrical conductivity and magnetic permeability. There are some research studies on different working fluids such as critic-stabilized ion by Jeyadevan and Natkasuka (2004), micro sized magnetic particles with 29.9 wt.% in carried fluid by Hongo and Tagahashi (2004), NaCl and KCl by Ghaddar and Sawara (2004), and silver nano-fluid by Park and Ma (2007). Ghaddar and Sawara (2004) proposed that if working fluid is nonconducting, it will move through a magnetic field without any interaction.

The goal of this study is to use the advantages of an oscillating heat pipe, magnetic field, and magnetic fluid to develop a mathematical model. This model will investigate the effect of a magnetic field on the oscillating motion and heat transfer. To reach the full potential of a closed-loop oscillating heat pipe, developing a mathematical model is necessary to understand the characteristics of a closed-loop oscillating heat pipe. Since there are just a few works on this subject, it will be helpful to know the performance and efficiency of an oscillating heat pipe by applying a magnetic field and magnetic fluid. A magnetic field will improve the performance of a closed-loop oscillating heat pipe. This knowledge is useful to apply a magnetic field to other types of heat pipes or heat exchangers.

2. MODEL OF OSCILLATING MOTION

The physical model of a closed-loop oscillating heat pipe is shown in Fig. 1. The bend of the tube is not considered. This study focuses only on the vertical direction of flow. There is an evaporating section at the

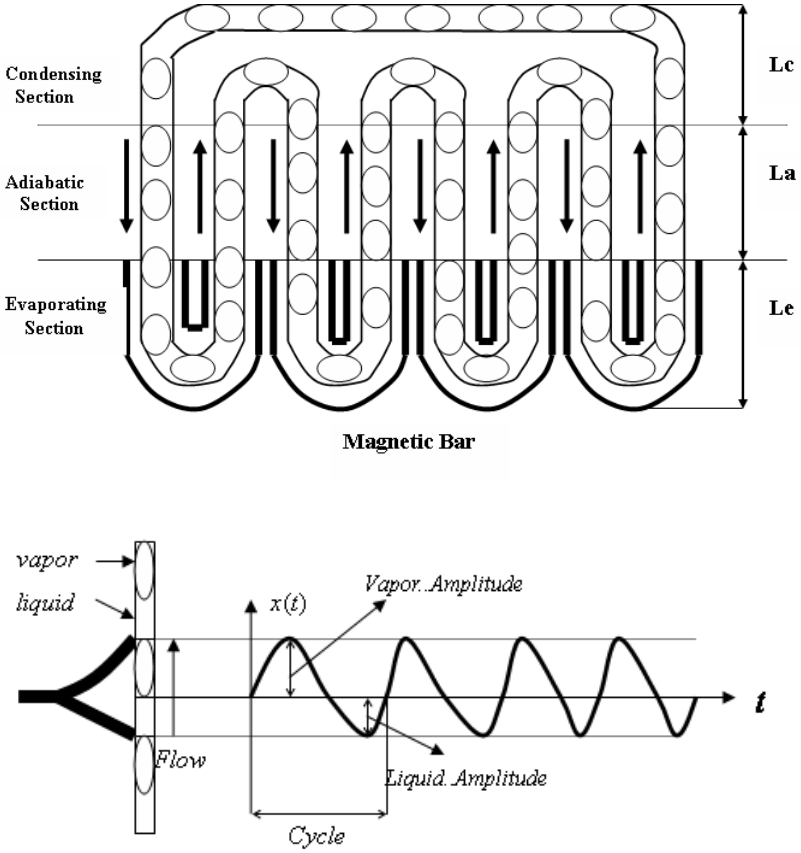

FIG. 1: Model of oscillating motion

bottom, an adiabatic section at the center, and a condensing section at the top side. A magnetic field occurs only in the evaporating section.

The model is built upon the following assumptions:

1. In the steady state, liquid slug and vapor bubbles have equal sizes.
2. Liquid slug and vapor bubbles flow in the same direction.
3. The lengths of evaporating, adiabatic, and condensing sections are equal.
4. Liquid slug is incompressible and a vapor bubble is assumed to be an ideal gas.
5. Shear stress at the liquid–vapor interface is negligible.

2.1 Magnetohydrodynamics Force

In the evaporating section, a magnetohydrodynamics phenomenon appears. When the working fluid flows across the magnetic field with the velocity (u), the current density (J) occurs, inducing the force (F_{mag}) that interacts with the working fluid. The current density that affects the working fluid can be calculated by

$$J = \sigma(u \times B) \ . \tag{1}$$

The magnetic force which acts on the working fluid can be defined as

$$F_{mag} = J \times B = \sigma u B^2 \ . \tag{2}$$

Energy from the magnetic field generated at the working fluid is

$$W_{mag} = \frac{J \times J}{\sigma} = \sigma u^2 B^2 \ . \tag{3}$$

The pressure difference from the magnetic field acting on the fluid at the evaporating section is

$$\Delta P_{mag} = \frac{\sigma u B^2}{A} \ , \tag{4}$$

where

$$B = \mu_r \mu_o H \ .$$

Therefore, Eq. (4) can be expressed as

$$\Delta P_{mag} = (\sigma u \mu_r^2 \mu_o H^2)/A \ . \tag{5}$$

2.2 Conventional Forces

Conventional forces that act on a liquid slug and vapor bubble are a driving force (F_d), a frictional force (F_f), and a vapor force (F_v). An MHD force (F_{mag}) is added in both the liquid slug and vapor bubble as shown in Fig. 2. Driving force can be determined by the Clapeyon equation. Heat is added to the evaporating section through the wall and reaches the working fluid. Saturated liquid will be vaporized to the saturated vapor. The pressure in the evaporating section is

$$P_e = P_o \exp\left(\frac{h_{fg}(T_e - T_o)}{RT_eT_o}\right) \tag{6}$$

Combined with the forced oscillation, the heat added on the evaporating area can be immediately distributed throughout the entire oscillating heat pipe. The pressure difference between the evaporation and the condensation section defined by Ma et al. (2006) is shown in Eq. (7)

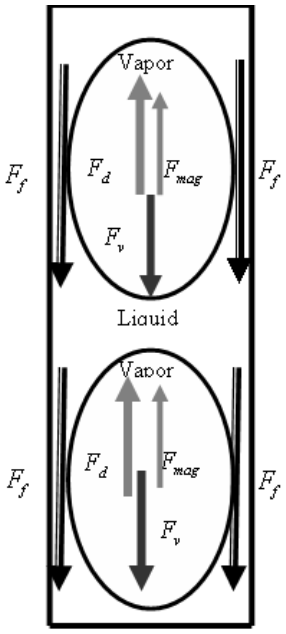

FIG. 2: Directional of force

$$\Delta P = P_e - P_c = P_c\left(\frac{\exp(h_{fg}(T_e - T_c) - 1}{RT_eT_c}\right). \tag{7}$$

Utilizing the Taylor series and neglecting the high order terms, Eq. (7) becomes

$$\Delta P = \Delta T_d \frac{h_{fg}\rho_{vc}}{T_e} \ , \tag{8}$$

where $\Delta T_d = T_e - T_c$. This can be explained by vapor trapped between the liquid slugs. It is compressible. Hence, the volume extraction and contraction in the vapor space cause an oscillation. The system frequency is ω. A model predicting the temperature difference between the evaporating and condensing sections may be approximately expressed as

$$\Delta T_d = \left(\frac{T_e - T_c}{2}\right)(1 + \cos \omega t) \ . \tag{9}$$

Substituting Eq. (9) in Eq. (8), the driving pressure causing the oscillating motion can be found as presented in Eq. (10)

$$\Delta P_d = \left(\frac{h_{fg}\rho_{vc}}{T_e}\right)\left(\frac{T_e - T_c}{2}\right)(1 + \cos \omega t) \ . \tag{10}$$

The frictional force that arises from the interaction between liquid and vapor of the pipe wall can be evaluated by

$$\frac{dP_f}{dx} = -\frac{4\tau_s}{D_h} \ . \tag{11}$$

A solid interface can be expressed in terms of the frictional factor

$$\tau_s = \frac{1}{8} f \rho \left(\frac{dx}{dt}\right)^2. \tag{12}$$

Integrating Eq. (12), the total pressure drops due to the frictional force. The pressure difference can be determined by

$$\Delta P_f = \left[\left(f_l \mathrm{Re}_l\right)\left(\frac{\mu_l L_l}{2D_h^2}\right) + \left(f_v \mathrm{Re}_v\right)\left(\frac{\mu_v L_v}{2D_h^2}\right)\right]\frac{dx}{dt}. \tag{13}$$

Due to the symmetry, only one path is considered. The total characteristic length of an oscillating pipe equals the summation of the pipe lengths in three sections as shown below

$$L_t = L_e + L_a + L_c$$

based on the low Reynold number flow rate. The fictional pressure in Eq. (13) can be written as

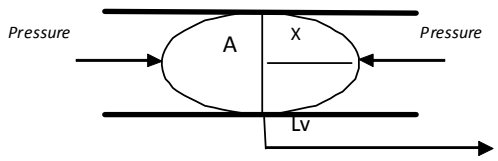

FIG. 3: Vapor in space at pressure increase

$$\Delta P_f = \frac{8P}{D_h}(\mu_l L_l + \mu_v L_v)\frac{dx}{dt} . \quad (14)$$

Vapor is assumed to be the ideal gas; therefore, the vapor pressure at time t is

$$P_{vt} = \frac{m_v RT}{L_v A} . \quad (15)$$

At the time $t + \Delta t$, heat added to the evaporating section causes the increase in pressure and decrease in the vapor volume by $-xA$, as shown in Fig. 3. The vapor in the space at time $t + \Delta t$ is

$$P_{v,t+\Delta t} = \frac{m_v RT}{(L_v - x)A} , \quad (16)$$

because x is very small relative to L_v. The pressure difference in the evaporating section can be defined as

$$\Delta P_v = \frac{\rho_v RTx}{L_v} \quad (17)$$

2.3 Governing Equations

Substituting all terms of forces using Newton's second law, the total force can be obtained as shown in Eq. (18)

$$\Sigma F = m\left(\frac{d^2x}{dt^2}\right),$$

$$m\left(\frac{d^2x}{dt^2}\right) + F_f = D_d + F_{mag} - F_v . \quad (18)$$

Substituting the force term with ΔPA

$$m\left(\frac{d^2x}{dt^2}\right) + A\Delta P_f = A\Delta P_d + A\Delta P_{mag} - A\Delta P_v . \quad (19)$$

Substituting all parameters with

$$(L_l\rho_l + L_v\rho_v)A\frac{d^2x}{dt^2} + \left[\frac{8P}{D_h}(\mu_l L_l + \mu_v L_v)\right]A\frac{dx}{dt} + \frac{A\rho_v RTx}{L_v}$$

$$= \left(\frac{Ah_{fg}\rho_{vc}}{T_e}\right)\left(\frac{T_e - T_c}{2}\right)(1 + \cos\omega t) + \sigma\mu_r^2\mu_o^2 H^2 u. \quad (20)$$

Equation (20) is equivalent with an ordinary differential equation of the force damp vibration shown in Eqs. (21) and (22)

$$\frac{d^2x}{dt^2} + \frac{c}{m}\frac{dx}{dt} + \frac{k}{m}x = \frac{B}{m} + \frac{B}{m}\cos\omega t + \frac{F_{mag}}{m}, \quad (21)$$

$$\frac{d^2x}{dt^2} + 2\omega\xi\frac{dx}{dt} + \omega^2 x = \frac{B}{m} + \frac{B}{m}\cos\omega t + \frac{F_{mag}}{m}, \quad (22)$$

where

$$m = (L_l\rho_l + L_v\rho_v)A ,$$

$$c = A\frac{8P}{D_h}(\mu_l L_l + \mu_v L_v) ,$$

$$k = \frac{A\rho_v RT}{L_v} ,$$

$$B = \left(\frac{Ah_{fg}\rho_{vc}}{T_e}\right)\left(\frac{T_e - T_c}{2}\right) ,$$

$$F_{mag} = \sigma\mu_r^2\mu_o^2 H^2 u ,$$

$$\omega = \sqrt{\frac{k}{m}} ,$$

$$\xi = \frac{c}{2m\omega} .$$

Equation (22) is nonhomogenous and is the second order of an ordinary differential equation. The initial conditions of the Laplace transform are

$$x = 0 , \quad \frac{dx}{dt} = 0 , \quad \text{at} \quad t = 0.$$

Therefore, the oscillating motion of closed-loop heat pipes with magnetic field can be obtained by Eq. (23)

$$x(t) = \frac{B + F_{mag}}{m} \quad (23)$$

$$\times\left[\frac{\dfrac{\sqrt{\zeta^2-1}\sin(\omega t) - e^{-\zeta\omega t}\sinh\left[\omega(\sqrt{\zeta^2-1})t\right]}{2\zeta\omega^2\sqrt{\zeta^2-1}} + \dfrac{1 - e^{-\zeta\omega t}\left[\cosh((\sqrt{\zeta^2-1})\omega t) + \dfrac{\zeta\sinh((\sqrt{\zeta^2-1})\omega t}{\sqrt{\zeta^2-1}}\right]t}{\omega^2}\right].$$

3. MODEL OF HEAT TRANSFER

In the evaporating section, the working fluid inside the tube receives heat from hot water (Q_{hw}). Heat is transferred to the oscillating heat pipe (Q_{hp}) throughout as well as to the condensing section by the cooling water (Q_{cw}). Heat is lost to the ambient by convection (Q_{ea}, Q_{ca}) and is transferred to the tube wall by conduction (Q_w). Heat transfer of the oscillating heat pipe can be modeled as a system of the thermal resistance, as shown in Fig. 4.

The total heat-transfer coefficient is defined in Eq. (24)

$$h_{tt} = \frac{Q_{hp}}{(T_e - T_c)} \left(\frac{1}{A_e} + \frac{1}{A_c}\right) . \tag{24}$$

The thermal resistance and energy are balanced to simplify the model. Heat balance in the evaporating section is shown in Eq. (25)

$$Q_{hp} = Q_{hw} - Q_w - Q_{ea} . \tag{25}$$

Equation (26) presents the heat balance in the condensing section

$$Q_{hp} = Q_{cw} - Q_w + Q_{ca} . \tag{26}$$

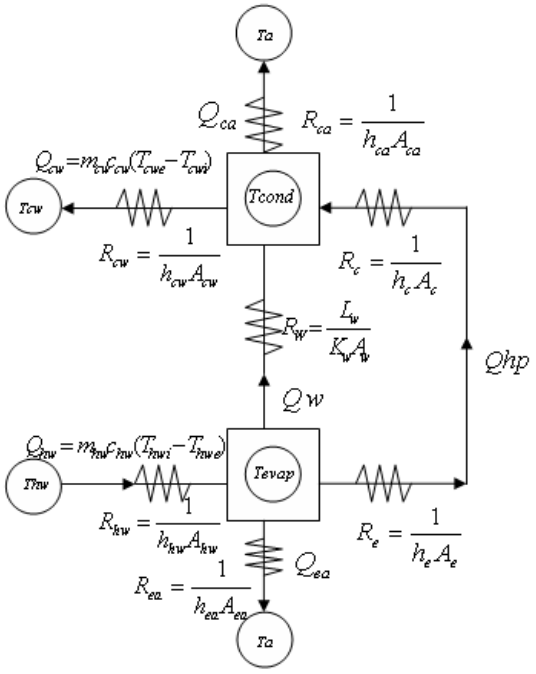

FIG. 4: Model of heat transfer

Dobson and Graf (2003) studied and approximated convection and conduction to the wall from heat loss and heat transfer, using the following terms:

$$Q_{ea} = 0.349(T_e - T_c) , \tag{27}$$

$$Q_{ca} = 0.691(T_e - T_c) , \tag{28}$$

$$Q_w = 0.415(T_e - T_c) . \tag{29}$$

Nucleate boiling, force convection, and MHD will appear inside the oscillating heat pipe. The total heat-transfer coefficient in the evaporating section is defined as

$$h_{tt} = h_{NB} + h_C + h_{MHD} \tag{30}$$

Ozisik (1990) developed the model to describe the nucleate boiling heat-transfer coefficient presented in Eq. (31)

$$h_{NB} = 0.00122 \left[\frac{k_l^{0.79} c_{pl}^{0.45} \rho_l^{0.49}}{\sigma^{0.5} \mu^{0.29} h_{fg}^{0.24} \rho^{0.24}} \right]$$

$$\times \Delta T_{sat}^{0.24} \Delta P_{sat}^{0.75} S , \tag{31}$$

where S is the suppression factor of the two-phase Reynolds number shown in Eq. (29)

$$S = (1 + 2.56 \times 10^{-6} \, \mathrm{Re}_{tp}^{1.17})^{-1} . \tag{32}$$

The two-phase Reynolds number is

$$\mathrm{Re}_{tp} = \mathrm{Re}_t \left[F(X_{tt}) \right]^{1.25} , \tag{33}$$

where the liquid Reynolds number is

$$\mathrm{Re}_t = \frac{G(1-x)D_i}{\mu_i} \tag{34}$$

and the Martinelli parameter is

$$X_{tt} = \left(\frac{1-x}{x}\right)^{0.9} \left(\frac{\rho_v}{\rho_l}\right)^{0.5} \left(\frac{\mu_l}{\mu_v}\right)^{0.1} , \tag{35}$$

$$F(X_{tt}) = 1 \quad \text{where} \quad X_{tt}^{-1} \le 0.1 ,$$

$$F(X_{tt}) = 2.35(0.213 + \frac{1}{X_{tt}})^{0.736} \quad \text{where} \quad X_{tt}^{-1} \ge 0.1 .$$

Utilizing the Martinelli parameter for the two-phase flow, the heat-transfer coefficient due to forced convection by oscillating motion can be readily determined by

$$h_c = F(X_{tt})h_l \ , \tag{36}$$

where h_l is the liquid-phase heat-transfer coefficient which is defined as

$$h_l = 0.023\left(\frac{k_l}{D_i}\right)\mathrm{Re}_l^{0.8}\,\mathrm{Pr}_l^{0.8} . \tag{37}$$

In the evaporating section, the magnetohydrodynamics phenomenon appears when the working fluid flows across the magnetic field (B) with the velocity (u). The current density (J) then occurs. It will induce the magnetic energy (W_{mag}) which later interacts with the working fluid. The current density that affects the working fluid can be calculated by $J = \sigma(u \times B)$. The energy of magnetic field is generated inside the working fluid. It can be defined in terms of the heat-transfer coefficient as presented in Eq. (38) in the same unit (W/cm^2.^{o}C)

$$h_{MHD} = W_{mag} = J\,J = \sigma u^2 B^2 \ , \tag{38}$$

where $B = \mu_r\mu_0 H$. Therefore, the heat-transfer coefficient from the magnetic field is defined as

$$h_{MHD} = (\sigma^2\mu_r^2\mu_o^2 H\,u^2) \ . \tag{39}$$

The heat-transfer coefficients of nucleate boiling, forced convection, and MHD are then substituted in Eq. (30). The overall heat-transfer coefficient of the oscillating heat pipe is obtained in Eq. (40)

$$h_{tt} = 0.00122\left[\frac{k_l^{0.79}c_{pl}^{0.45}\rho_l^{0.49}}{\sigma_t^{0.5}\mu^{0.29}h_{fg}^{0.24}\rho_v^{0.24}}\right]\Delta T_{sat}^{0.24}\Delta p_{sat}^{0.75}S + \ F(X_{tt})$$

$$\times 0.23\left[\frac{k_l}{D_l}\right]\mathrm{Re}_l^{0.8}\,\mathrm{Pr}_l^{0.8} + \ \sigma^2\mu_r^2\mu_0^2 B^2 u^2 . \tag{40}$$

4. RESULTS AND DISCUSSIONS

4.1 Results of Oscillating Motion

The model of the oscillating motions was simulated using various parameters as follows:

- Working fluids [water, salt water]
- Operating temperature [40^{o}C, 60^{o}C, 80^{o}C]
- Total length [1 m, 2 m, 3 m]
- Temperature difference [40^{o}C, 60^{o}C, 80^{o}C]
- Magnetic field strength [0, 0.5, 1 T]

The comparison of this study and that of Ma et al. (2006) is shown in Fig. 5. The oscillating motion of Ma et al. (2006) and this study are similar. Water is used as working fluid, operating temperature is 60^{o}C. The amplitudes of both studies are slightly increasing. After 1 s, the amplitudes are constant as they reach their steady-state level. The phase and frequency of this study are the same as those in [Ma et al., 2006]; however, the amplitude is greater comparing with the results of Ma et al. (2006). Under the influence of a magnetic field, the amplitude of oscillation is a little bit higher than that without a magnetic field. In Fig. 6, magnetic permeability and electrical conductivity of salt water are higher than those of water; hence, the magnetic field has more effects when compared with Fig. 5. There are five oscillating pulses within 2 s. The amplitude of the oscillation is increased when the magnetic field strength is increased. The frequency of the oscillation is constant when the magnetic field strength is varied. The working fluid can receive a larger amount of heat to amplify the amplitude due to the appearance of the magnetic field. The relation between the total length and the oscillating motion is shown in

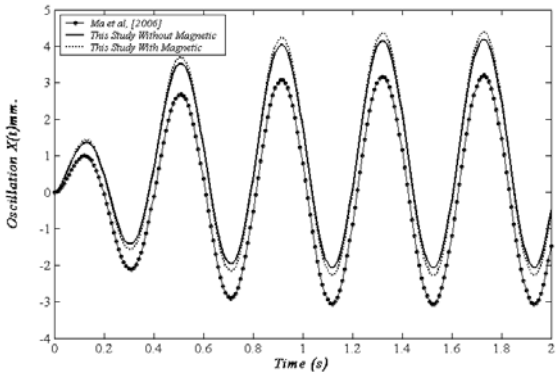

FIG. 5: Comparison of oscillating motion between (Ma et al., 2006) and this study

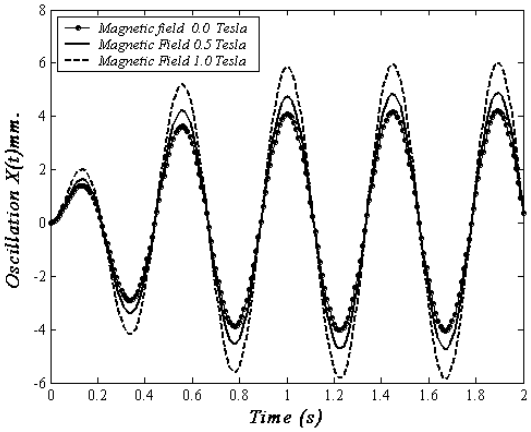

FIG. 6: Oscillating motion of magnetic fluid (salt water) with various magnetic field strengths

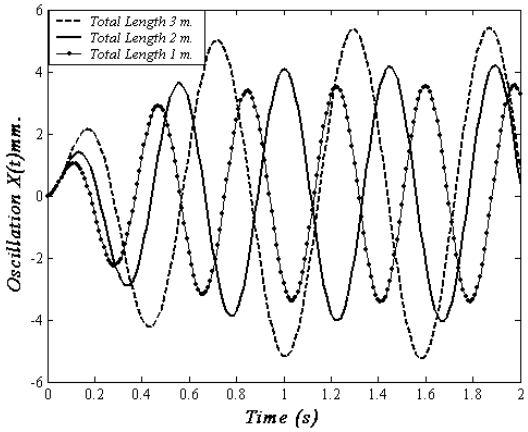

FIG. 7: Oscillating motion of salt water with various total lengths

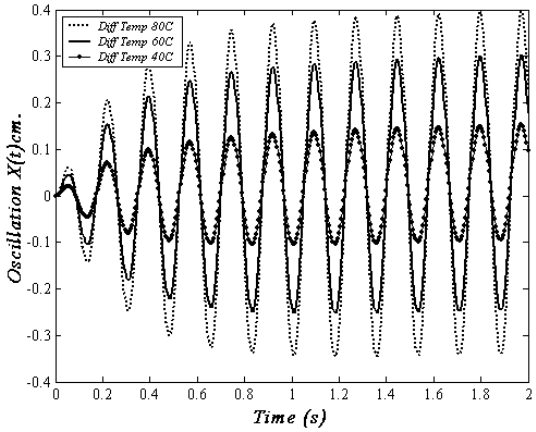

FIG. 8: Oscillating motion of salt water with various temperatures

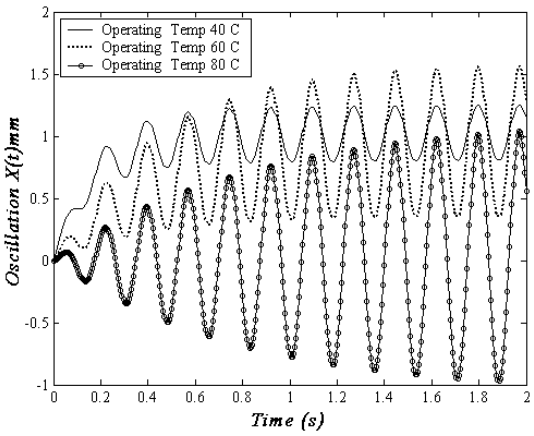

FIG. 9: Oscillating motion of salt water with various operating temperatures

Fig. 7. The total length of a pipe is changed from 1 to 3 meters. Amplitudes are increased but phase and frequency are decreased. Amplitude and frequency of the oscillation is higher and lower, respectively, as the pipe is longer. The relation between the temperature difference of the evaporating and condensing sections is also studied. When the temperature difference is increased from 40°C to 60°C to 80°C, the amplitude of the oscillating motion is also increased, while both phase and frequency of the oscillating motion are constant. The simulation results support the assumption that the temperature difference influences the oscillation, as shown in Fig. 8. The relation between the operating temperature and the oscillating motion is shown in Fig. 9. Liquid slug and a vapor bubble oscillate at a higher level with larger amplitude when the operating temperature is increased. It means that the higher oscillation is generated when the operating temperature higher.

4.2 Results of Heat Transfer

Heat transfer, heat-transfer coefficient, heat input in the evaporating section, heat output in the condensing sec-

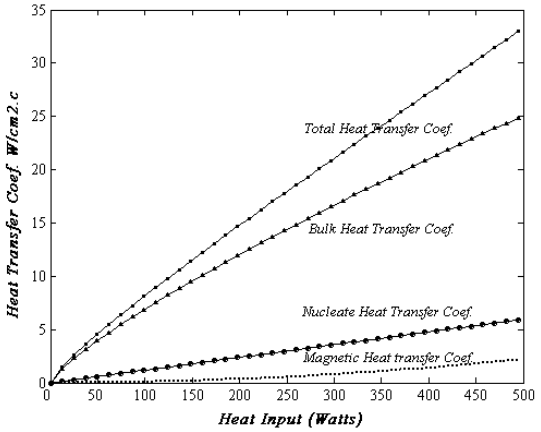

FIG. 10: Comparison of the heat-transfer coefficients when working fluid is salt water

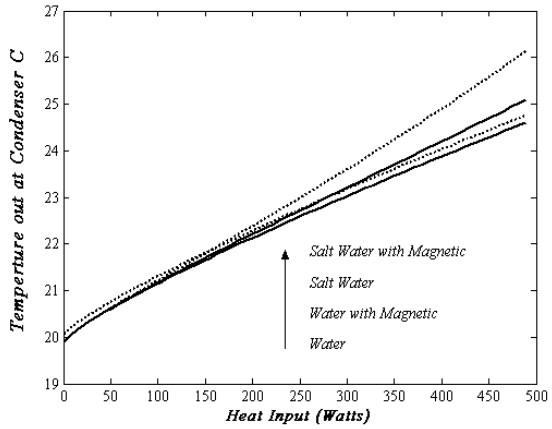

FIG. 11: Output temperature in condensing with and without magnetic field

tion, and efficiency of the heat pipe with various magnetic field strengths were observed. The studied parameters are:

- Working fluid [water, salt water]
- Temperature at condensing section [20^{o}C]
- Temperature at evaporating section [80^{o}C]
- Total length of pipe [1 m]
- Inner diameter [1.65 mm]
- Magnetic field strength [0, 0.3, 0.6, 0.9, 1.2 T]

Figure 10 shows the relation between the heat-transfer coefficient and the heat input. Working fluid is water. When the heat input is increased, the heat-transfer coefficient is also increased. The total heat-transfer coefficients are bulk, nucleate, and magnetic heat-transfer coefficients. Although, a magnetic heat-transfer coefficient shows the least impact on heat transfer a magnetic field can still enhance heat-transfer rate of an oscillating heat pipe. If the working fluid is changed from water to salt water, the magnetic heat-transfer coefficient is increased, because of magnetic properties of the working fluid. Temperature of cooling water in the condensing section is increased from 20^{o}C to the maximum at 26.4^{o}C when the working fluid is salt water with a magnetic field. A minimum value of cooling water temperature is 24.6^{o}C when the working fluid is water without a magnetic field, as shown in Fig. 11. Hence, we can conclude that magnetic field can improve the ability of heat receiving by salt water

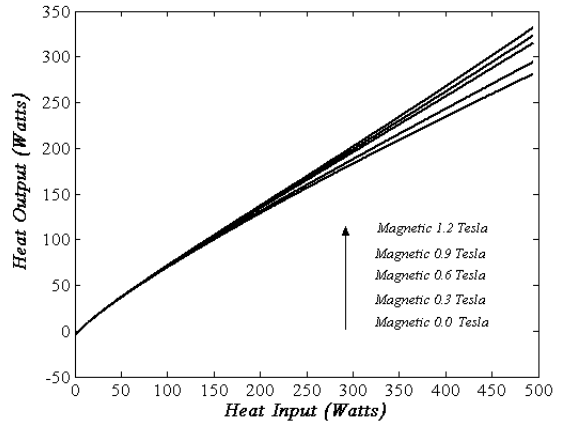

FIG. 12: Heat output and heat input with various magnetic field strengths

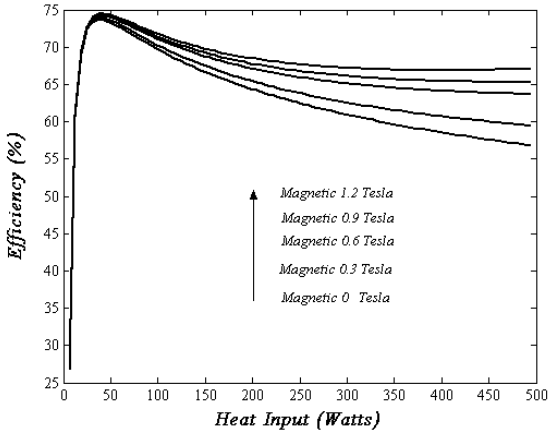

FIG. 13: Comparison of the efficiency with various magnetic field strengths

as well as can increase temperature at the condenser more than water. The relation between heat input and output is shown in Fig. 12. Heat input is increased from 0 to 500 W. At heat input of 500 W, the magnetic field strength is increased from 0 to 1.2 T and the heat output is increased from 275 W to 325 W. It means that magnetic field can increase as maximum as 50 W of heat output. At low heat input (0–150 W), magnetic field does not affect heat output. Efficiency is slightly increased when the magnetic field strength is increased as illustrated in Fig. 13. A maximum value of the efficiency is 75% at the magnetic field strength of 1.2 T. The oscillating heat pipe can increase its efficiency up to 8%, comparing to the case of a nonmagnetic field.

5. CONCLUSIONS

The mathematical model of a closed-loop oscillating heat pipe is developed to study and describe the influence of magnetic field on oscillating motion and heat transfer. The accuracy of the model is validated with other studies. The results show good agreement. The effect of the magnetic field increases oscillating motion by increasing the amplitude of motion at the same frequency. A higher value of the magnetic field strength produces a higher amplitude of oscillation. Magnetic field raises the temperature in the condenser. Heat output and heat pipe efficiency are slightly increased when the magnetic field strength is increased. Magnetic field increases heat output up to 50 W and raises heat-pipe efficiency to 8%. Magnetic fluid (salt water) can receive more force and energy from the magnetic field than water. High operating temperature can increase the oscillation. High temperature difference also provides more oscillation. The total elongate length of the tube can change the phase oscillation. This study will significantly help to interpret the activation of the oscillating motion by magnetic field and offer a solution on how to enhance the heat-transfer rate in an oscillating heat pipe.

ACKNOWLEDGMENT

The research has been supported generously by the Faculty of Engineering, Mahasarakham University.

REFERENCES

Dobson, R. T. and Graf, G. Thermal characteristic of an ammonia charge pulsating heat pipe, *Proc. 7th Int. Heat Pipe Symp.*, Korea, p. k1, 2003.

Elizbieta, F., Ghaddar N., and Chaban, F. Experimental study on the magnetic convection in a vertical cylinder, *Exp. Thermal Fluid Sci.*, vol. 29, pp. 971–980, 2005.

Feng, C. L., Kunugi, T., and Serizawa, A. MHD effect on flow structures and heat-transfer characteristics of liquid metal gas annular flow in a vertical pipe, *Int. J. Heat Mass Transfer*, vol. 48, pp. 2571–2581, 2005.

Ghaddar, N. and Sawaya, E. Testing and modeling thermo-syphonic closed loop magnetohydrodynamic electrolyte flow, *J. Thermophys. Heat Ttransfer*, vol. 17, no. 2, pp. 129-137, 2004.

Hongo, T. and Takahashi, M. Forced convective boiling heat transfer of magnetic fluid in a thin tube under a magnetic field, *J. Jpn. Soc. Mech. Eng. B*, vol. 65, no. 634, pp. 1992–1999, 1999.

Jeyadevan, B. and Natkasuka, K. Performance evaluation of critic ion-stabilized magnetic fluid heat pipe, *J. Magnetism Magnetic Mater.*, vol. 289, pp. 253–256, 2004.

Ji, H. C. and Gardner, R. A. Numerical analysis of turbulent pipe flow in a transverse magnetic field, *Int. J. Heat Mass Transfer*, vol. 40, no. 8, pp. 1839–1851, 1997.

Liang, S. B. and Ma, H. B. Oscillating motions of slug flow in capillary tubes, *Int. Comm. Heat Mass Transfer*, vol. 31, no. 3, pp. 365–375, 2004.

Ma, H. B., Hanlon, M. A., and Chen, C. L. An investigation of oscillating motions in a miniature pulsating heat pipe, *Microfluidics Nanofluidics*, vol. 2, no. 2, pp. 171–179, 2006.

Ozisik, M. N. *Heat Transfer. A Basic Approach*, Int. ed., McGraw Hill, pp. 510–513, 1985.

Park, K. and Ma, H. B. Nano-fluid effect on heat transport capability in a well balanced oscillating heat pipe, *J. Thermophys. Heat Ttransfer*, vol. 21, no. 2, pp. 443–445, 2007.

Rittidech, S., Terdtoon, P., Murakami, M., Kamonpet, P., and Jompakdee, W. Correlation to predict

heat transfer characteristic of closed-end oscillating heat pipe at normal operation, *Appl. Thermal Eng.*, vol. 23, pp. 497–510, 2003.

Shafii, M. B. and Faghri, A. Analysis of heat transfer in unlooped and looped pulsating heat pipe, *Int. J. Numer. Meth. Heat Fluid Flow*, vol. 12, no. 5, pp. 585–609, 2002.

Shu, S. L, Lee, H., Tagawa, T., Ozoe, H., and Hua, B. Enhancement of heat-transfer and air flow rates in a pipe with application of a magnetic field, *J. Enhanced Heat Ttransfer*, vol. 10, no. 1, pp. 45–60, 2003.

Zhang, Y. and Faghri, A. Oscillatory flow in pulsating heat pipe with arbitrary numbers of turns, *J. Thermophys. Heat Transfer*, vol. 17, no. 3, pp. 340–347, 2003.

Journal of Enhanced Heat Transfer

CONTENTS VOLUME 17, 2010

Page Range of Issues
Issue 1: 1–109; Issue 2: 111–204; Issue 3: 205–291; Issue 4: 293–380

Number 1

Number 2

Number 3

Number 4

Journal of Enhanced Heat Transfer

AUTHOR INDEX VOLUME 17, 2010

Page Range of Issues
Issue 1: 1–109; Issue 2: 111–204; Issue 3: 205–291; Issue 4: 293–380

Journal of Enhanced Heat Transfer

SUBJECT INDEX VOLUME 17, 2010

Page Range of Issues
Issue 1: 1–109; Issue 2: 111–204; Issue 3: 205–291; Issue 4: 293–380
